ABSTRACT

BRADY, RENEÉ JHENEALL. Mathematical Modeling of the Acute Inflammatory Response & Cardiovascular Dynamics in Young Men. (Under the direction of Mette S. Olufsen.)

The magnitude of the initial reaction of the body to a pathogenic microbial infection or severe tissue trauma is of critical importance; an uncontrolled acute inflammatory response can cause further tissue damage, sepsis, and ultimately death, while an insufficient response can result in inadequate clearance of the pathogens, leading to chronic inflammation. A normal inflammatory response helps to combat threats posed by pathogens and restore the body to a healthy state. Inflammation caused by surgery or endotoxin increases the vagal activity due to the neuroinflammatory reflex. The increased vagal tone increases the risk of vasovagal syncope, as seen in 40% of patients during the early post-surgical phase. To gain insight into the factors associated with this and to identify those who may be susceptible to problems, a mathematical model of the acute inflammatory response (AIR) to an endotoxin challenge has been developed and analyzed in this thesis. The model incorporates the main components of the AIR: the resting and activated monocytes, the pro-inflammatory cytokines tumor necrosis factor-α (TNF-α) and interleukins-6 and -8 (IL-6 and IL-8), and the anti-inflammatory cytokine interleukin-10 (IL-10). Our model was calibrated to experimental data obtained from experiments measuring the circulating cytokines over 8 hours in 20 healthy subjects administered a low dose of lipopolysaccharide. Subject-specific parameters were estimated and related to changes in heart rate variability (HRV), a measure that can be obtained non-invasively in real-time.

Conditions such as autonomic dysfunction (nausea, fainting, and dizziness) and chronic fatigue, which result in response to changes in the autonomic nervous system, can be detrimental for a patient recovering post-surgery. We hypothesize that blood pressure and heart rate are affected by changes in the pro-inflammatory mediators via changes in temperature, the production of the vasodilator nitric oxide (NO), and changes in the pain perception tolerance (PPT). To test this hypothesis, we have coupled the inflammatory model with a non-pulsatile cardiovascular model. The non-pulsatile model was derived by integrating a pulsatile cardiovascular model, using the same parameter values in both formulations. This is the first model of its kind developed in such a way. While previous studies have formed an understanding of the effect of the cardiovascular system on the inflammatory response, via a cholinergic anti-inflammatory pathway, limited research has been done to understand the effect of the inflammatory system on the cardiovascular dynamics.

The coupled model was calibrated to experiment measurements of heart rate and blood pressure. Model simulations compared well with data and were able to predict both normal and abnormal responses. Results were cross-validated against second day data. HRV analysis showed that an enhanced inflammatory response is correlated with attenuated vagal firing. The identified and

modeled associations between inflammatory responses and changes in HRV suggest that HRV data may be further modeled and used as a non-invasive, real-time monitoring marker of autonomic dysfunction in response to inflammation.

Mathematical Modeling of the Acute Inflammatory Response & Cardiovascular Dynamics in Young
Men

by
Reneé Jheneall Brady

A dissertation submitted to the Graduate Faculty of
North Carolina State University
in partial fulfillment of the
requirements for the Degree of
Doctor of Philosophy

Applied Mathematics

Raleigh, North Carolina

2017

APPROVED BY:

_____   _____
Hien T. Tran   Belinda S. Akpa

_____   _____
Ralph C. Smith   Mette S. Olufsen
                                                    Chair of Advisory Committee

DEDICATION

To my mother, Angela, for all of the sacrifices that you have made for me to be where I am today, for your continuous love and support, and for always encouraging me to strive for the best.
To my son, Chance, for being such a wise, understanding, loving, and caring little boy. I hope that witnessing my journey will inspire you one day, like my mother has inspired me.

BIOGRAPHY

Renee was born in Ontario, Canada and moved to South Florida at the age of seven. Even at a young age, she always had an interest in mathematics, often attending college level-mathematics courses with her mother. After graduating from high school in 2007, Renee attended Florida Agricultural & Mechanical University, where she majored in Mathematics, with a focus on Actuarial Science. While considering career options during her senior year, Renee decided that continuing her education in Applied Mathematics was attractive and began applying to graduate programs.

After taking a tour of NC State's campus and speaking with several graduate students and professor in the Applied Mathematics program, Renee felt that NC State was the perfect place for her to progress in her academic career. She began the Applied Mathematics Ph.D. program in August of 2011. While excelling in her classes, Renee also had the opportunity to teach several undergraduate courses and help incoming students find their love for mathematics. It was a very rewarding experience.

Renee gave birth to a baby boy Chance, in August of 2013, taking a brief break from the university. After returning in the Spring of 2014, she received her Master's degree and began working with Dr. Mette S. Olufsen to study the inflammatory process in the Cardiovascular Dynamics Group. In May of 2015, Renee was given the opportunity to travel to Copenhagen, Denmark where she was able to collaborate with clinicians and be exposed to new ways that mathematics was being integrated into the field of physiology. After completing her degree, Renee and her family will be relocating back to the Sunshine State, as she has accepted a Postdoctoral Fellow position in the Integrated Mathematical Oncology Department with Moffitt Cancer Center in Tampa, Florida.

ACKNOWLEDGEMENTS

TABLE OF CONTENTS

LIST OF TABLES

CHAPTER

1

INTRODUCTION

Invasion by pathogens or injury triggers an acute inflammatory response (AIR) that is vital in the repulsion of pathogens and the induction of a repair mechanism in damaged tissues. Inflammation is characterized by heat, redness, swelling, pain, and can lead to loss of function if not properly controlled. An insufficient response can cause persistent tissue injury, resulting in conditions such as autoimmune diseases, cancer, and lifestyle-related disorders [Janeway et al., 2001]. An uncontrolled, excessive production of pro-inflammatory mediators from immune cells and traumatized tissues can cause systemic inflammatory response syndromes (SIRS) such as sepsis and, in life-threatening events, septic shock [Schulte et al., 2013]. The Agency for Healthcare Research and Quality lists sepsis as the most expensive condition treated in U.S. hospitals, costing more than $23 billion in 2013 [Torio & Moore, 2013]. It has been found that many chronic inflammatory diseases can increase a person's risk of cancer. In particular, Crohn's disease and multiple sclerosis, which have been linked to colorectal and breast cancer, respectively, the second and third most deadly cancers.

In recent years, it has been suggested that inflammation may be connected to autonomic dysfunction (nausea, fainting, and dizziness) [Tracey, 2002] and chronic fatigue syndrome (CFS) [Buchwald et al., 1997], two symptoms that have been found in girls exhibiting side effects to vaccinations against human papillomavirus (HPV) [Brinth et al., 2015]. Recent studies by Dr. Jesper Mehlsen's group (not yet published) suggest that G-protein coupled antibodies with agonistic effects

on receptors in the autonomic nervous system may be partially responsible for postural orthostatic tachycardia syndrome (POTS), an autonomic disorder in which a change from the supine position to an upright position causes an abnormally large increase in heart rate [Grubb, 2008]. It is known that inflammation is associated with a large number G-protein coupled receptors (GPCRs), which are crucial to the migration of monocytes and their accumulation at sites of inflammation [Sun & Ye, 2012]. Increased levels of pro-inflammatory mediators have also been reported in cases of CFS.

There exists a host of diseases and disorders which can be linked to inflammation, many of which can be fatal if not properly treated. The development of treatment options can be challenging due to the inability to elicit a large range of endotoxin doses, in some cases much higher than safe, in humans. Thus, many treatment options are developed from clinical studies in mice. However, physiological differences between humans and mice, allow for limited confidence in these treatment options. The development of mathematical models of the inflammatory response that are validated against human data can aid in the development of treatment options more suitable for humans. We hypothesize that changes in the inflammatory response affect blood pressure and heart rate, in particular changes in heart rate variability (HRV). Using HRV as a preoperative marker might enable physicians to identify patients requiring a different treatment regimen post-surgery. This may provide a non-invasive, real-time monitoring marker of early sepsis, which can shorten a patient's hospital stay, reducing health care costs and improving a patient's quality of life.

1.1 Overview of Dissertation

There are five aims of this study: (1) develop a mathematical model of the acute inflammatory response to an endotoxin challenge, (2) render the model patient-specific by conducting sensitivity analysis, and identifiability analysis. The latter is essential to determine a subset of parameters that can be estimated, given the model and available data. Estimated parameters will be analyzed and used to categorize differences between normal and abnormal responders. (3) Develop a non-pulsatile cardiovascular model that can be used in lieu of the more complex, pulsatile cardiovascular model, to predict blood pressure using heart rate as an input, (4) couple the inflammatory model with the the non-pulsatile cardiovascular model, incorporating temperature, nitric oxide and pain, (5) use sensitivity analysis, identifiability analysis and optimization techniques, to render the coupled model patient-specific.

The proceeding chapters are organized as follows:

Chapter 2 introduces the immune and cardiovascular systems.

Chapter 3 describes the experimental data used to calibrate and validate the model.

Chapter 4 introduces sensitivity analysis, identifiability analysis, and the optimization techniques used to render the models patient-specific. Uncertainty quantification, using both frequentist and Bayesian methods, is also introduced. The implementation of each method is demonstrated using a modification of the SIRS model.

Chapter 5 describes the inflammatory model.

Chapter 6 presents model predictions for the inflammatory model, as well as parameter variations between subjects, and uncertainty quantification results.

Chapter 7 develops the non-pulsatile cardiovascular model from the pulsatile model and develops the coupled cardiovascular inflammatory model.

Chapter 8 presents predictions of the coupled cardiovascular-inflammatory model and comparisons of parameter values.

Chapter 9 summarizes the results of the dissertation and discusses future work.

CHAPTER

2

PHYSIOLOGICAL BACKGROUND

This chapter presents the components of the immune and cardiovascular systems needed to develop the mathematical model. The inflammatory response to endotoxin is also explained in detail. The general information presented here are from the physiology book by [Guyton & Hall, 2011]. The immune system and the inflammatory response are discussed in Section 2.1. The cardiovascular system is described in Section 2.2. As a motivation for coupling the two systems together, the inflammatory reflex is discussed in Section 2.3.

2.1   Immune System

The immune system protects the body from pathogens such as bacteria, viruses, parasites, and antigens. It consists of the white blood cells (WBCs), tissue cells derived from WBCs, the thymus, lymph nodes, and lymph vessels. The body relies on the immune system to aid in distinguishing between its own cells and foreign cells/substances and to create a defense mechanism to destroy the invaders. The body's ability to resists foreign organisms is called immunity and is either innate or acquired. Innate immunity is activated immediately or within hours of a pathogen's appearance in the body, while adaptive immunity is an antigen-specific immune response that does not develop until after the body is first attacked by the antigen. Once an antigen has been recognized, the

adaptive immune system produces immune cells specifically designed to attack that antigen. The body's response to an endotoxin results in a short-term response that is innate and for that reason, for the remainder of the thesis we focus on such a response.

Monocytes & Neutrophils

The immune response is controlled by WBCs. There are six types of WBCs normally present in the blood: polymorphonuclear neutrophils, polymorphonuclear eosinophils, polymorphonuclear basophils, monocytes, lymphocytes, and plasma cells. Additionally, there are a large number of fragments of the megakaryocyte, a cell found in the bone marrow that is similar to WBCs. These disk-shaped fragments are called platelets.

Polymorphonuclear cells (neutrophils, eosinophils, and basophils) have a granular appearance and for this reason are sometimes called granulocytes. Mast cells are specific granulocytes containing granules that are rich in histamine and heparin, which act as vasodilators and anticoagulants, respectively. Neutrophils are mature phagocytic WBCs; that is, they can attack and destroy bacteria immediately. Along with monocytes, they are primarily responsible for mediating the inflammatory response. Both neutrophils and monocytes are stored in the bone marrow until they are needed in the circulatory system. Monocytes make up about 5.3% of the 7000 WBCs per microliter of blood. They circulate in the blood for 10 to 20 hours and can migrate outside of the capillary membranes in response to the detection of a pathogen or other foreign substance. After entering the tissue, the monocytes swell to become activated monocytes (macrophages), which can either become attached to the tissue or remain mobile. Lymphocytes include B and T cells, which are responsible for producing antibodies and scanning for cellular abnormalities, respectively. Plasma cells are formed in the lymph tissues and are transported to different parts of the body where they are needed. Platelets are active in the blood clotting mechanism.

As shown in Figure 2.1, in response to the pathogen entering the body, platelets release blood-clotting proteins at the wound site and mast cells release histamine which cause the blood vessels to dilate. This enables monocytes and neutrophils to move out of the blood vessel via a process called diapedesis, in which they squeeze through the pores of the capillary membranes. Once they are outside of the blood vessel, these immune cells control the inflammatory process via chemotaxis and phagocytosis. During chemotaxis, in response to the release of chemical substances in the tissues, neutrophils and activated monocytes move toward the source of the chemical. These chemicals can be produced by the bacteria themselves or by degenerative products of the inflamed tissues. Chemotaxis is effective up to 100 micrometers away from an inflamed tissue and since no tissue is more than 50 micrometers away from a capillary, the chemotaxis system can easily move the
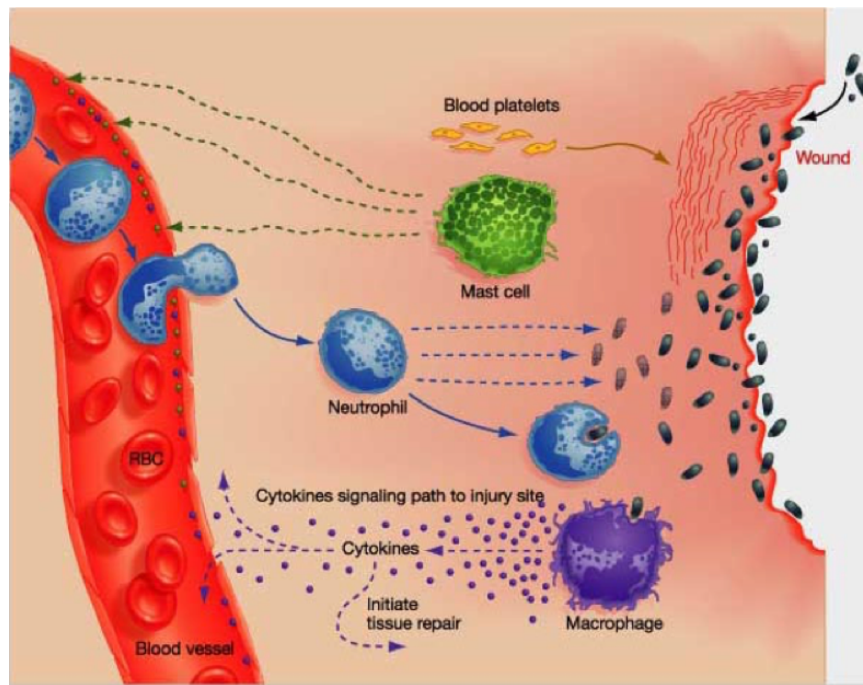
Figure 2.1 *The inflammatory response.* In response to bacteria, platelets from the blood release blood-clotting proteins at the wound site. Mast cells secrete factors that mediate vasodilation and vasoconstriction, as blood continues to flow to the injured area. Neutrophils and activated monocytes (macrophages) release factors that phagocytize pathogens. Activated monocytes release cytokines that attract immune cells to the site and activate cells involved in tissue repair. The inflammatory response subsides once the pathogen is removed. Used with permission from [Resource, 2015].

monocytes and neutrophils into the inflamed area. Once the cells reach the chemical source, they ingest the offending agent via phagocytosis (or cellular ingestion). Natural structures in the body have smooth surfaces that can resist phagocytosis, but foreign particles do not. This ensures that the cells are not destroying each other in the process of eliminating the initial threat.

In the event that the inflammation cannot be controlled by the inflammatory mediators, the inflammation can spread to the remaining parts of the body. This will force the mediators and immune cells in other parts of the body to attempt to reduce the levels of inflammation. An unsuccessful attempt at this can lead to whole-body inflammation (i.e. sepsis) and eventually, septic shock.
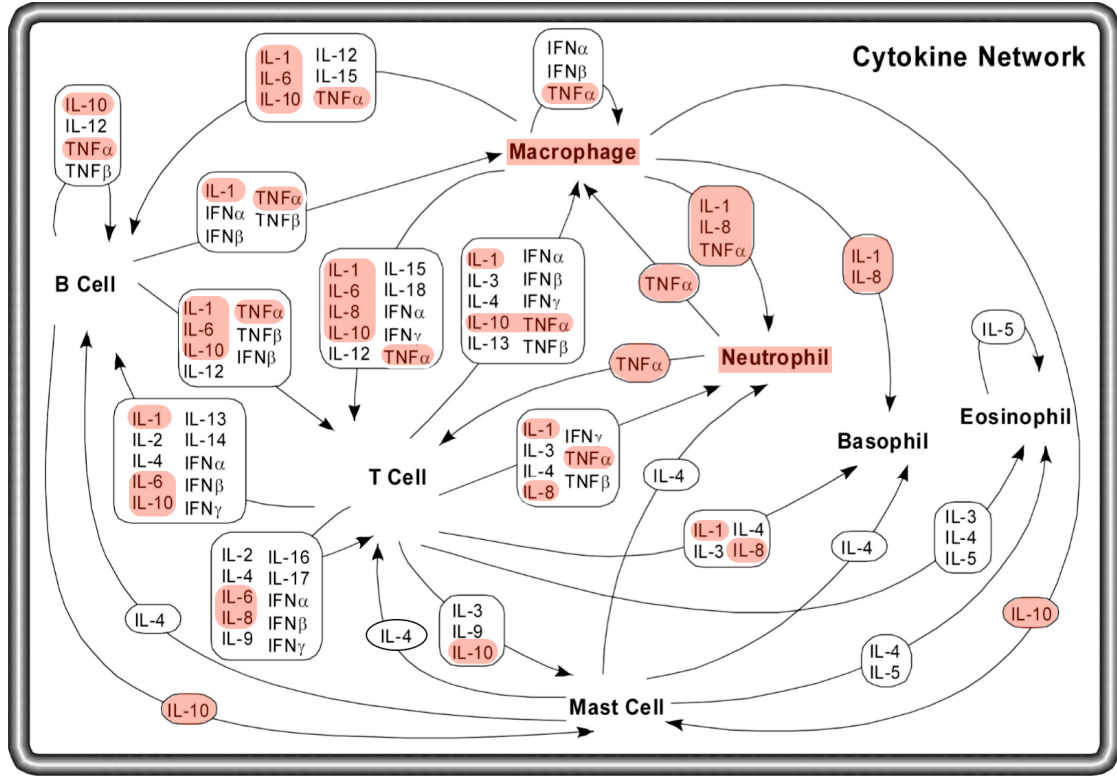
Figure 2.2 *Cytokine network.* The immune system is regulated by several cell types including B cells, T cells, activated monocytes (macrophages), mast cells, neutrophils, basophils, and eosinophils. Each cell type has a specific role and communicates with each other using cytokines. The components highlighted in red will be included in the mathematical model. Used with permission from [Zhang & An, 2007].

Cytokines

The monocytes and neutrophils release cytokines, small secreted proteins that mediate the interactions and communications between cells [Zhang & An, 2007]. They affect the activation and differentiation of the immune response by migrating through the tissues and to the blood vessels where they encourage the activation of the monocytes and chemotaxis through the release of chemicals into the tissue. Cytokines are released sequentially through the cytokine cascade, as one cytokine stimulates the immune cells to produce another cytokine. They work synergistically or antagonistically to mediate the inflammatory response as shown in Figure 2.2.

The pro-inflammatory cytokines included in the mathematical model are tumor necrosis factor α (TNF-α) and interleukins 1β, 6, and 8 (IL-1β, IL-6, and IL-8, respectively) that are involved in the up-regulation of the inflammatory reactions. TNF-α is one of the most extensively studied cytokines. Accumulation is seen within 90 minutes of a pathogen entering the body. Consequently, TNF-α is characterized as an early regulator of the immune response [Schulte et al., 2013]. It is primarily responsible for differentiation and activation of immune cells and has been implicated in the induction of fever. The production of TNF-α up-regulates the release of other pro-inflammatory mediators. When released systemically, TNF-α has been shown to cause septic shock and is said to be responsible for several chronic inflammatory diseases such as rheumatoid arthritis, Crohn's disease, and psoriasis [Rossol et al., 2011].

IL-1β is also characterized as an early mediator, with accumulation detected two hours after pathogen introduction. It is said to be one of the main pyrogens and is involved in coagulation [Schulte et al., 2013]. IL-6 is involved in the activation of B and T cells, as well as the induction of fever. It is primarily released in response to TNF-α and though considered pro-inflammatory, it exhibits anti-inflammatory behavior inhibiting the release of TNF-α and IL-1β [Schulte et al., 2013]. IL-8 is a chemotactic activating cytokine, also known as chemokine ligand 8 (CXCL8). It isj responsible for the activation of neutrophils [Harada et al., 1994]. Its accumulation is seen two hours after the pathogen is introduced.

The anti-inflammatory cytokine interleukin-10 (IL-10) suppresses the production of the pro-inflammatory cytokines. It also stimulates the production of IL-1 receptor antagonist (IL-1Ra) and soluble TNF-α receptors (sTNFRs), which are soluble inhibitors of the pro-inflammatory cytokines IL-1β and TNF-α, respectively. IL-10 is classified as an endogenous antipyretic, reducing the effects of TNF-α, IL-1β, and IL-6 on temperature. IL-10 is a late mediator of the response, as its production is does not peak until three hours after the pathogen is introduced.

Though it might be useful to model the behavior of additional cytokines, in this study we focus on the interactions between the pro-inflammatory cytokines TNF-α, IL-6, and IL-8 and the anti-inflammatory cytokine IL-10. These four mediators are regarded as the main drivers of the early pro-inflammatory response (TNF-α), the intermediate step between pro- and anti-inflammation (IL-6), neutrophil activation (IL-8), and the late anti-inflammatory response (IL-10). We will primarily focus on monocytes, as opposed to neutrophils, in the proceeding chapters.

2.2   Cardiovascular System

The cardiovascular system is responsible for maintaining metabolism and cell function by transporting nutrients, oxygen, carbon dioxide, hormones, and blood cells. Nutrients and oxygen are
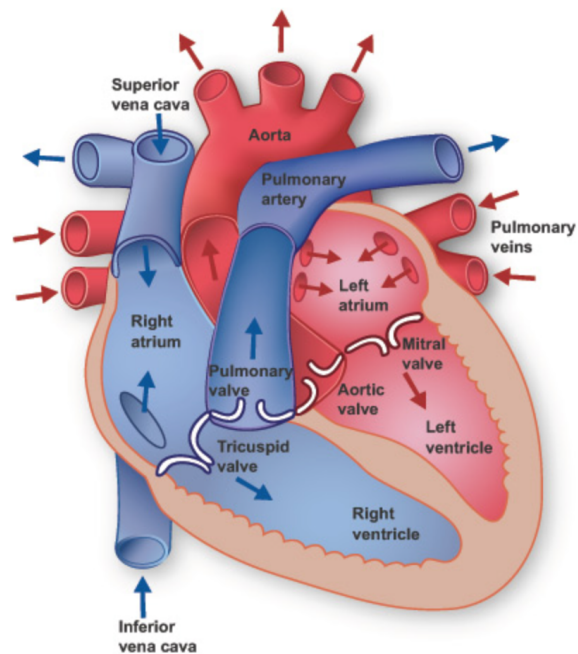
Figure 2.3 *Heart anatomy.* The heart is divided into four chamber: the left and right atria and the left and right venticles. Blow flow through the heart is regulated via four valves. The tricuspid valve controls blood flow between the atrium and ventricle in the right heart. The pulmonary valve regulates blood flow between the right ventricle and the pulmonary artery. Blood flows from the left atrium to the left ventricle via the mitral valve. Finally, the aortic valve controls blood flow from the left ventricle to the aorta. Used with permission from [Institute, 2016].

transported to the tissues, while metabolic waste products such as carbon dioxide are removed. The system is comprised of the heart, blood, and blood vessels and with each heartbeat, blood is pumped throughout the body via a network of arteries, arterioles, capillaries, venules, and veins.

Blood is transported to the lungs via the pulmonary circuit and to the vascular tissues via the systemic circuit. The pulmonary circuit operates under a lower pressure than the systemic circulation (15 versus 100 mmHg). This is due to the systemic circuits need to facilitate blood flow to the furthest extremities of the body, while the pulmonary circuit is only responsible for blood flow through the lungs.
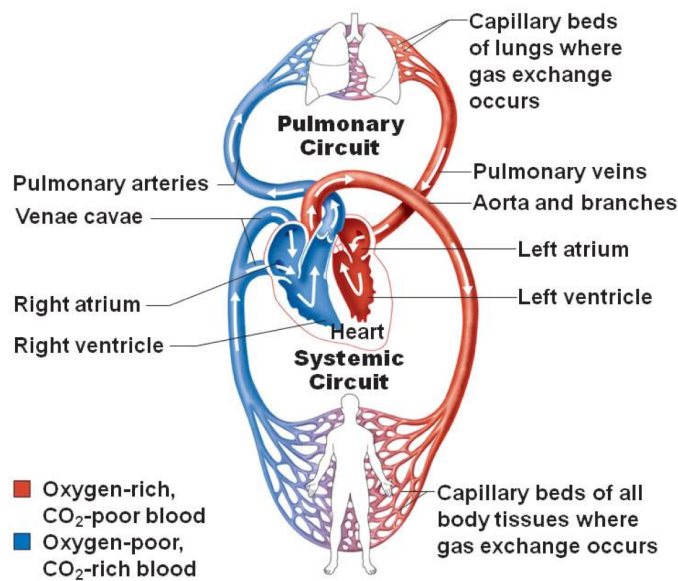
Figure 2.4 *The Cardiovascular System* The left heart receives oxygen-rich blood from the pulmonary veins and pumps it into the systemic arteries. In the capillaries, oxygen is removed from the blood and carbon dioxide is collected. The oxygen-depleted blood enters the systemic venous system. Blood is pumped from the right ventricle into the pulmonary artery and the pulmonary arterial tree. Blood is transported to the pulmonary capillaries of the lungs where carbon dioxide is removed from and oxygen enters the blood. This oxygen-rich blood flows through the pulmonary veins to the left atrium and finally, back to the left ventricle. Used with permission from Pearson.

2.2.1 The Heart

The heart consists of four chambers. The upper chambers are the left and right atria and the lower chambers are the left and right ventricles. On each side of the heart (the left heart and the right heart), the atria fill their respective ventricles. Blood flow through the heart is regulated by four valves, which under normal conditions, prevents the backflow of blood. The tricuspid valve controls blood flow between the atrium and ventricle in the right heart. The pulmonary valve regulates blood flow between the right ventricle and the pulmonary artery, which carries blood to the lungs to collect oxygen. Blood flows from the left atrium to the left ventricle via the mitral valve. Finally, the aortic valve controls blood flow from the left ventricle to the aorta. The anatomy of the heart is illustrated in Figure 2.3.
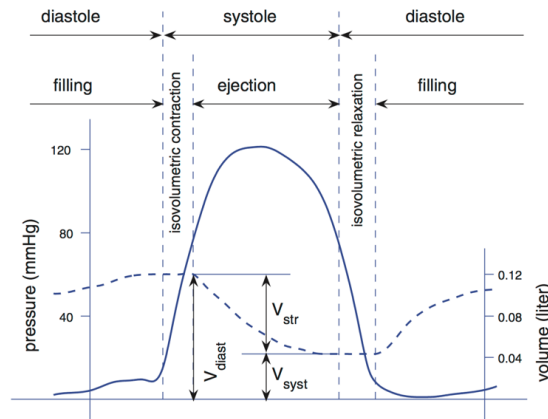
Figure 2.5 *The cardiac cycle.* As diastole begins, the heart relaxes and blood flows into the ventricle from the atrium, causing the ventricular volume (shown by dashed line) to rise. Systole begins when the heart begins to contract, increasing the ventricular pressure (solid line). When the ventricular pressure exceeds the atrial pressure, the atrioventricular valve closes. At this point, all valves are closed and the ventricle enters its isovolumic contraction phase. Once the ventricular pressure exceeds the arterial pressure, the outflow valves open. As ejection begins, the ventricular pressure continues to rise, while the volume decreases. Systole ends as the heart muscles begin to relax and the ventricular pressure decreases. When the ventricular pressure is less than the arterial pressure, the outflow valves close and diastole begins. The period of time at which both the outflow valve and atrioventricular valves are closed is called the isovolumic relaxation. The stroke volume V_{str} is defined by the difference between the end-diastole V_{diast} and end-systolic V_{syst} volumes. Used with permission from [Batzel et al., 2007].

2.2.2   The Circulation

The left heart receives oxygen-rich blood from the lungs and pumps it into the aorta. This vessel is the largest artery and is responsible for distributing blood to all regions of the body. The vasculature bifurcates into the systemic arteries, systemic arterioles, down to the systemic capillaries. The vessels progressively get smaller as the divisions continue. In the capillaries, oxygen and other substrates needed for metabolism are removed from the blood and carbon dioxide is collected. The oxygen-depleted blood enters the systemic venous system going through progressively larger vessels, from the systemic venules, to the systemic veins, and finally to the superior and inferior vena cava. Once the blood reaches the right ventricle, it is pumped into the pulmonary artery and the pulmonary arterial tree. Blood is distributed from the alveolar region of the lungs to the pulmonary capillaries where carbon dioxide is removed from the blood and oxygen enters the blood. This oxygen-rich blood flows through the pulmonary veins to the left atrium and finally, back to the left ventricle. The circulation of blood is shown in Figure 2.4.

11

2.2.3 The Cardiac Cycle

Each cardiac cycle consists of a period of relaxation called diastole followed by a period of contraction called systole. Systole begins with the contraction of the heart which causes the ventricular pressure to rise. When the ventricular pressure exceeds the arterial pressure, the atrioventricular valves (the tricuspid valve of the left heart and the mitral valve of the right heart) close. The outflow valves (the aortic and pulmonary valves) open and ejection begins once the pressure in the pressure in the left (right) ventricle exceeds the pressure in aortic (pulmonary) artery. This occurs at around 80 mmHg in the left ventricle and at around 10 mmHg in the right ventricle). The period of time when the both valves on either side of the ventricle are closed is called the isovolumic contraction reflecting that the volume is not changing. As ejection begins, the ventricular pressure continues to rise to about 120 mmHg in the left ventricle and to about 25 mmHg in the right ventricle. As systole ends, the heart muscles begin to relax and the ventricular pressure decreases. When the ventricular pressure is less than the arterial pressure, the outflow valves close and diastole begins.

The ventricular pressure continues to decrease until it reaches the pressure in the atria (around 5 mmHg in the left ventricle and 8 mmHg in the right ventricle), at which point the atrioventricular valve opens. The time in which both the outflow valves and the atrioventricular valves are closed is called the isovolumic relaxation. As diastole continues, the heart continues to relax, the ventricular pressure continues to decrease, and blood flows into the ventricle from the atrium. Diastole ends when the heart muscles begin to contract again, increasing the ventricular pressure above the pressure in the atria so that the atrioventricular valves close. The phases of the cardiac cycle are illustrated in Figure 2.5.

2.2.4 Cardiovascular Control

The cardiovascular system is controlled by local and global mechanisms. Local mechanisms respond to changes in pressure and chemicals by altering the flow, thereby affecting the vascular tone. Global mechanisms control the function of the cardiovascular system via neural, hormonal, and renal control, as well as influences from respiration. Global control mechanisms maintain blood pressures and flows by regulating heart rate, cardiac contractility, arterial resistance, venous capacitance, and blood volume. These actions are necessary to maintain an adequate supply of oxygen and removal of waste products in metabolism.

The autonomic nervous system consists of involuntary neural activities generated in response to various stimuli and regulate the smooth muscle cells, glands, and other organs. Afferent pathways carry information from sensory sites to the central control centers in the brain, while efferent pathways carry information from the brain to target organs and tissues.
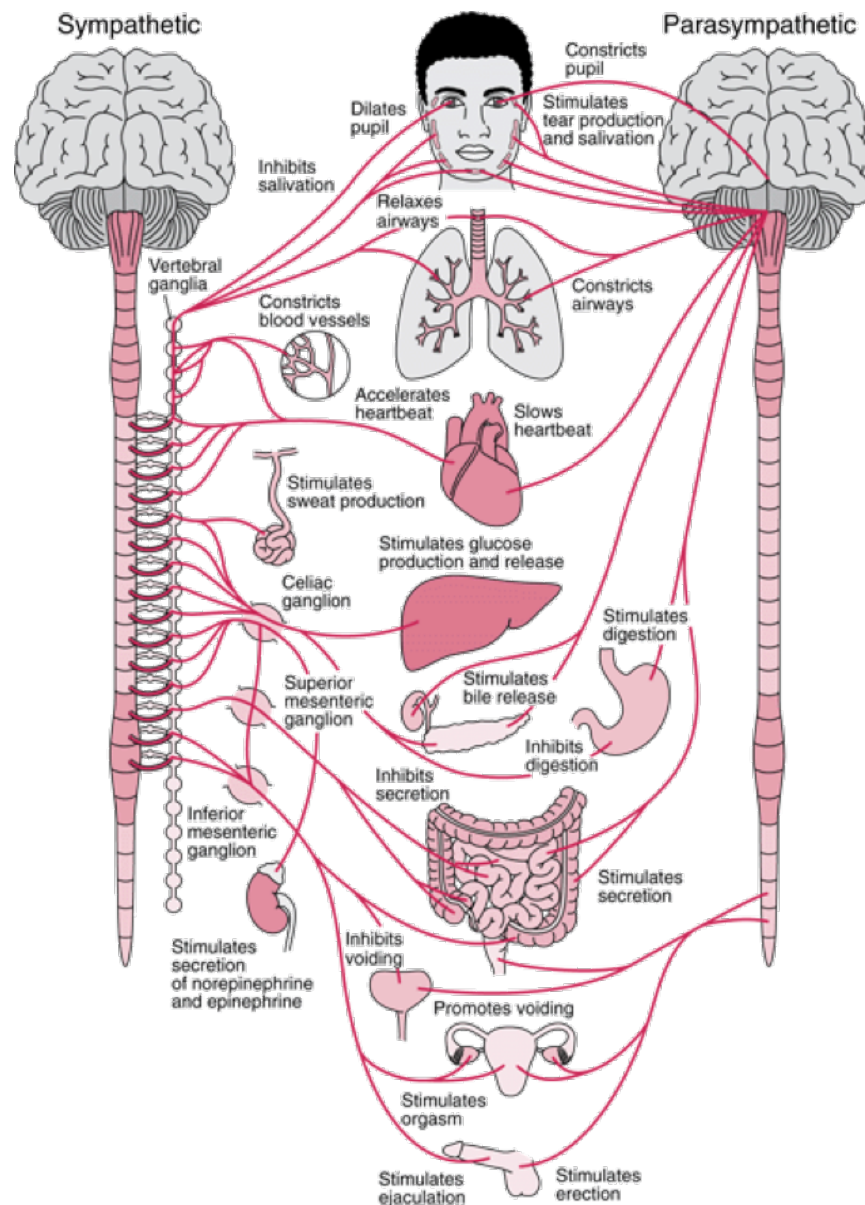
Figure 2.6 *Autonomic nervous system functions.* Sympathetic signals are carried through the sympathetic efferent nerves to the body tissues, while parasympathetic signals are carried through the vagus nerve, targeting specific organs. The main neurotransmitter of the sympathetic nervous system are adrenaline and noradrenaline, while acetylcholine is the main neurotransmitter of the parasympathetic nervous system. Used with permission from [Merck, 2017].
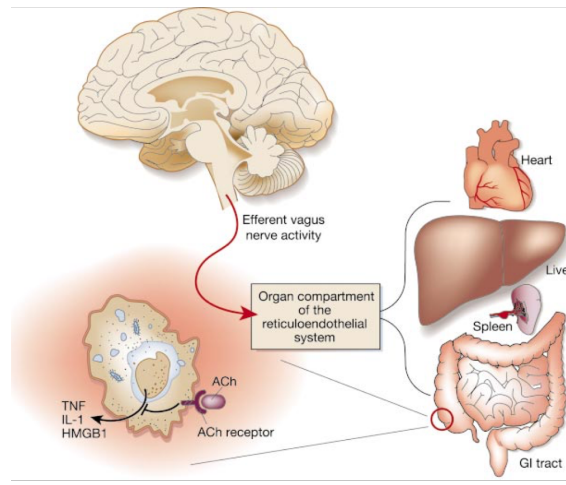
Figure 2.7 *The cholinergic anti-inflammatory pathway.* Efferent activity in the vagus nerve causes the release of acetylcholine (ACh) into the organs of the reticuloendothelial system (liver, heart, spleen, and gastrointestinal tract). ACh interacts with α-bungarotoxin-sensitive nicotinic receptors (Ach receptors) on tissue monocytes, which inhibit the release of TNF-α, IL-1β, high mobility group B1 (HMGB1), and other cytokines. Used with permission from [Tracey, 2002].

In response to a stimuli, such as a change in blood pressure, afferent signals are sent from the sensory site to the central nervous system and the brain. Efferent signaling from the brain is carried via sympathetic and parasympathetic pathways that work either in opposition or in synergy to control involuntary body functions. The main neurotransmitters of the sympathetic system are adrenaline and noradrenaline, while acetylcholine is the main neurotransmitter of the parasympathetic system. Sympathetic signals are carried through the sympathetic efferent nerves to the body tissues, while parasympathetic signals are carried through the vagus nerve, targeting specific organs. In general, an increase in sympathetic nerve activity increases heart rate, contractility, arterial resistance, and venous tone, while an increase in vagal activity tends to have an opposite effect. Due to its more specified function, parasympathetic activity tends to be quicker than sympathetic activity. The general pathways of the sympathetic and parasympathetic nervous systems are shown in Figure 2.6. In response to a decrease in blood pressure, the sympathetic activity increases, while the parasympathetic activity decreases. This causes heart rate to increase, as well as vasoconstriction of the blood vessels, allowing blood pressure to increase.

2.3 Inflammatory & Cardiovascular Interaction

Borovikova et al. [2000] discovered a parasympathetic anti-inflammatory pathway by which the brain modulates the systemic inflammatory response to endotoxin via acetycholine (ACh) (Figure 2.7). In particular, ACh interacts with α-bungarotoxin-sensitive nicotinic receptors on tissue monocytes. They found that an increase in vagal activity decreased the pro-inflammatory mediators TNF-α, IL-6, and IL-1β, but not the anti-inflammatory mediator IL-10. This pathway, called the cholinergic anti-inflammatory pathway, is responsible for the effective deactivation of endotoxin-stimulated human monocytes in the presence of ACh. In contrast to the diffusible anti-inflammatory network, which consists of cytokines, glucocorticoids, and other humoral mediators, the cholinergic anti-inflammatory pathway is discrete and localized in tissues where invasion and injury typically originate.

Tracey [2002] found that the production of cytokines in response to inflammation activates afferent firing to the brain, in particular the nucleus tractus solitarius. Subsequent vagus efferent activation inhibits cytokine synthesis through the cholinergic anti-inflammatory pathway. Efferent activity also increases heart rate variability. He named this inflammation-sensing and inflammation-suppressing network the inflammatory reflex, shown in Figure 2.8. This reflex is a localized, rapid and discrete regulator of the inflammatory response and shows that the pathway between changes in vagal activity and the inflammatory response is well-defined. However, as this was validated in mice, it leaves the question as to how the response is regulated in humans. Particularly, how blood pressure is controlled during an inflammatory response.

In response to inflammation, *we hypothesize that temperature has an effect on changes in heart rate, while blood pressure is primarily regulated by changes in pain perception and the vasodilator nitric oxide (NO). An increased presence of inflammatory mediators causes increased afferent firing to the brain, resulting in a fever [Hansen et al., 2001; Netea et al., 2000]. Subsequently, we hypothesize that this causes a decrease in efferent vagal activity, which increases heart rate.* In addition, Janum et al. [2016] found that pain perception threshold decreases during an endotoxin challenge, increasing sympathetic activity, leading to an increase in blood pressure. In response to the inflammatory mediator production, NO is released 2-4 hours after the endotoxin administration [Chowdhary et al., 2000]. As a vasodilator, NO causes blood pressure to decrease. These findings are summarized in Figure 2.9. Further details can be found in Chapter 7.

15
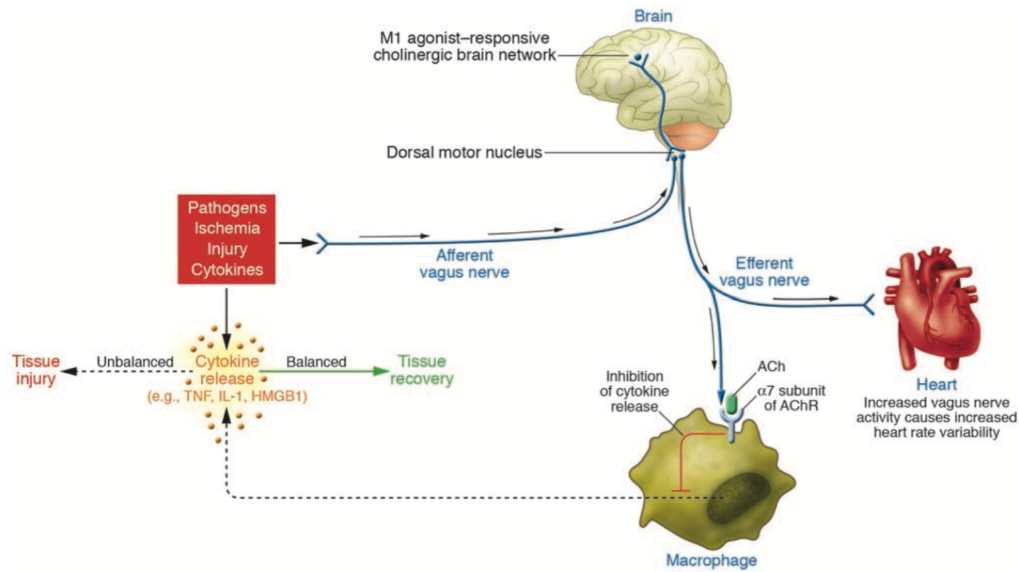
Figure 2.8 *The inflammatory reflex.* In response to a pathogen, ischemia (inadequate blood supply), or injury, cytokine production is activated. Afferent signals carried to the brain activate efferent signals that inhibit cytokine production via the cholinergic anti-inflammatory pathway. Efferent activity also increases instantaneous heart rate variability. Used with permission from [Tracey, 2007].

2.4   Mice versus Humans

To quantify the differences in the inflammatory responses between mice and humans, Copeland et al. [2005] conducted an experiment in which mice and humans were given equivalent doses of endotoxin and the levels of circulating inflammatory mediators, including TNF-α and IL-6 were measured and compared. This study found that humans experienced a rapid physiological response, consisting of fever, tachycardia, and slight hypotension, which was not evident in mice, as shown in Figure 2.10. Thus, it was concluded that the autonomic control system is affected by the inflammatory response in humans, but likely not in mice. This strengthens our hypothesize that it is indeed temperature controlling heart rate in response to an inflammatory event.
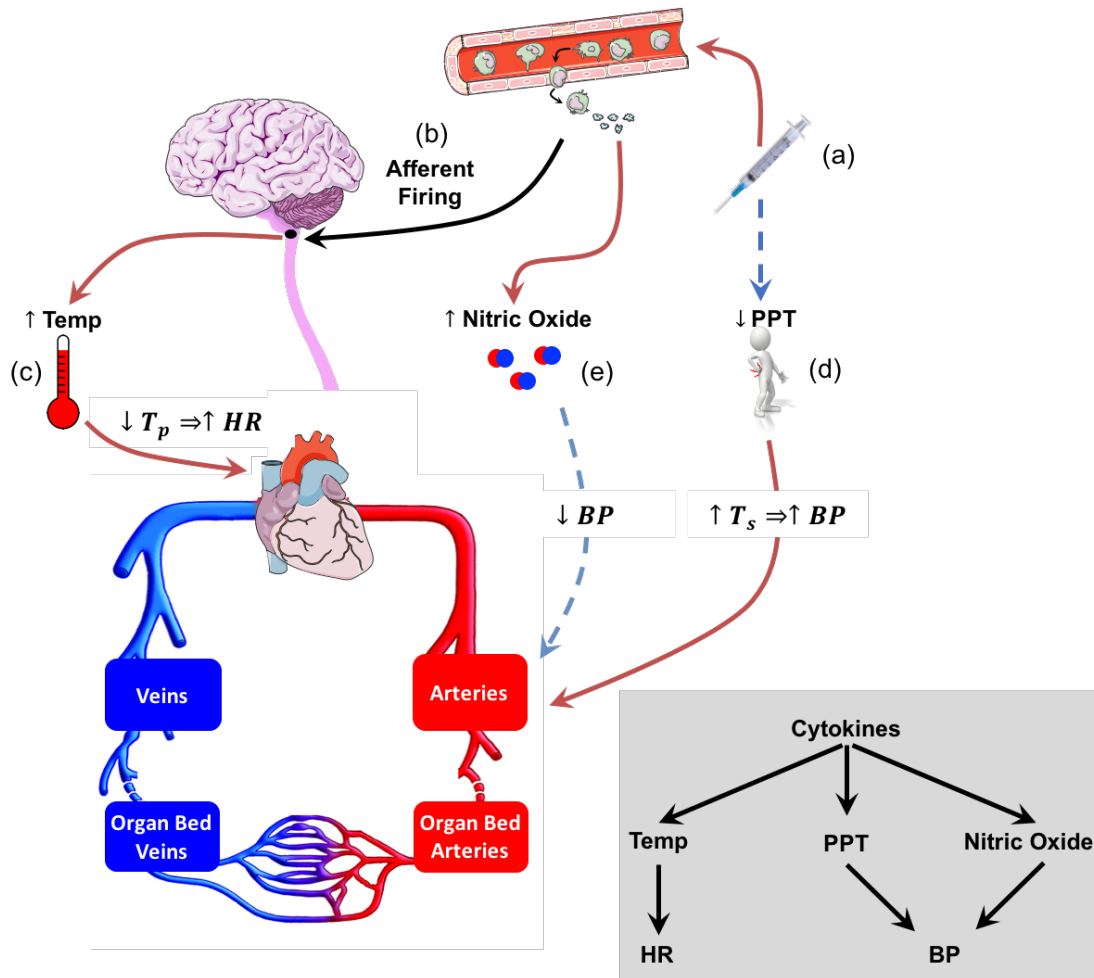
Figure 2.9 *Effect of inflammation on cardiovascular dynamics.* (a) Endotoxin causes release of inflammatory mediators and reduction of pain perception threshold (PPT). (b) Afferent firing in the brain, as a result of IL-1β, TNF-α, and IL-6 increases temperature. (c) In response to the fever, a decrease in parasympathetic activity (T_p) causes an increase in HR. (d) PPT reduction increases sympathetic activity (T_s), which increases blood pressure. (e) Between 2 and 4 hours after the administration of endotoxin, nitric oxide is released, decreasing BP.
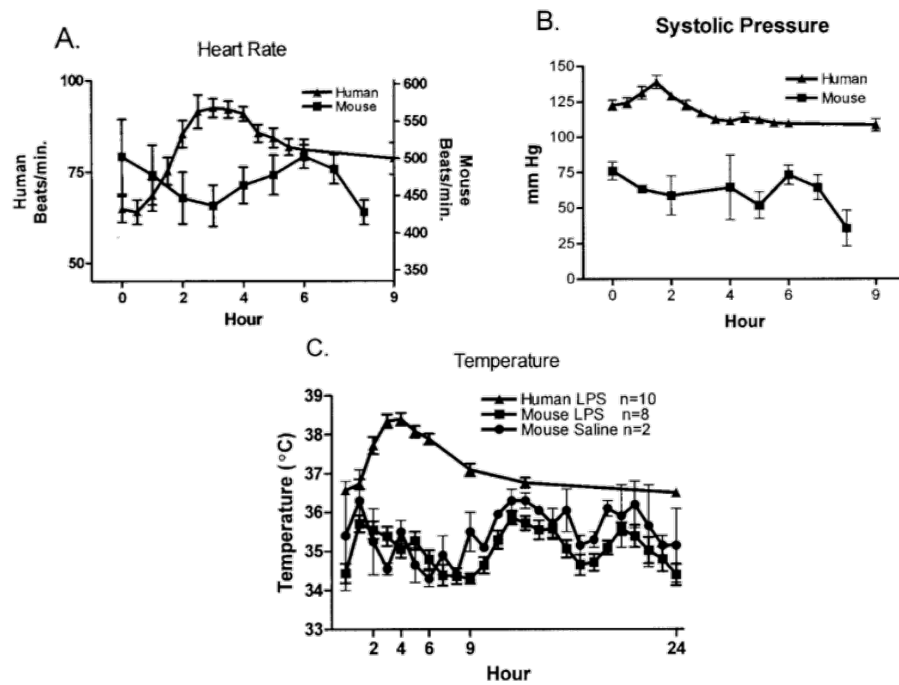
Figure 2.10 *Physiological changes in response to an endotoxin challenge in mice and humans.* Physiological changes in (A) heart rate, (B) systolic blood pressure, and (C) temperature in mice (■) and humans (▲) in response to equivalent doses of endotoxin. Mice and humans experience opposite affects on heart rate in response to an endotoxin. Blood pressure is initially increased in humans and eventually returns to baseline, while mice experience a slight increase later in the response. In (C), circles (●) show data from mice injected with saline demonstrating that the changes in body temperature are not due to the endotoxin but to normal diurnal variations. However, humans experience a large increase in temperature as a result of the endotoxin. Used with permission from [Copeland et al., 2005].

CHAPTER

3

DATA

The experimental data used throughout this thesis were made available by Dr. Jesper Mehlsen at the Coordinating Research Center at Frederiksberg Hospital in Copenhagen, Denmark. This chapter describes the experiment, the data acquired, and how the data were prepared for use in the mathematical models.

3.1 Experiment

3.1.1 Experimental Protocol

The study was an open-label, randomized cross-over study with two separate study days (trial A and B, respectively), in which an identical dose of lipopolysaccharide (LPS – also referred to as endotoxin) was injected. On each day, participants received a bolus of LPS at a dose of 2 ng/kg of body weight two hours after the start of the experiment. Blood samples for the analysis of the inflammatory mediator levels in plasma were collected before endotoxin infusion (at $t = -2$) and then at $t = 0, 1, 1.5, 2$h followed by one hour increments for the next 4 hours.

Trial B was preceded by the application of a nicotine patch, applied 10h before and removed 6h after the LPS challenge. Pain perception was recorded using a pressure algometry and heat stimulation at $t = -2, 2$ and $t = 6$h. A sequence of four tonic heat stimulations were delivered
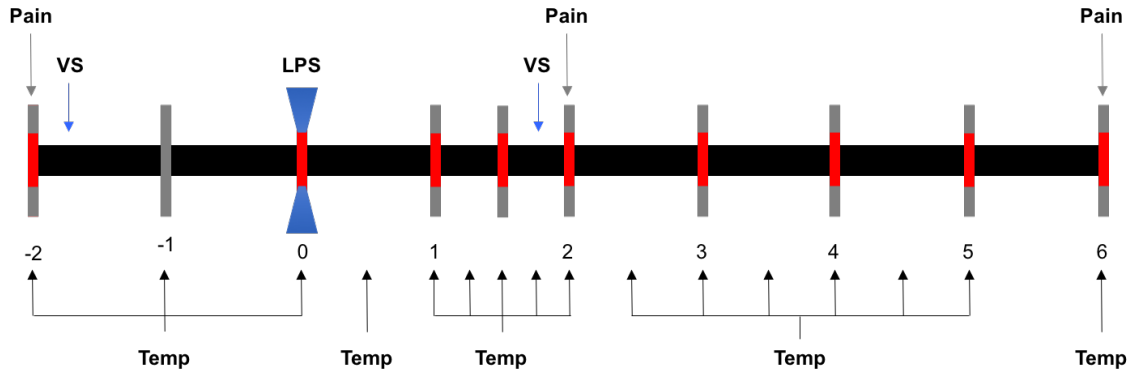
Figure 3.1 *Experimental Protocol*. Participants received a low-dose of LPS at $t = 0$. Red lines denote blood samples, collected at $t = -2, 0, 1, 1.5, 2$h followed by one hour increments for the next 4 hours. Participants performed the Valsalva maneuver at $t = 0.25$ and $t = 3.75$h (blue arrows). Pain perception was recorded at $t = -2, 2$, and 6h (gray arrows). Temperature was recorded periodically (black arrows).

with a duration of 5s each, separated by 30s, with temperatures ranging from $45°$ to $48°C$. Body temperature was also recorded periodically throughout the experiment. Changes in autonomic nervous system activity were observed by having the participants perform the Valsalva maneuver at $t = 0.25$ and $t = 3.75$h. The experimental protocol is summarized in Figure 3.1.

Trials A and B were randomized. To minimize the risk of tolerance, a minimum interval of 4 weeks was required between study days. To avoid any effects of recent infection, experiments were cancelled if the patient had experienced fever or malaise within the last 2 weeks before the trial days. The patients were instructed to remain physically inactive for 24h prior to each trial day.

Twenty healthy, young male volunteers, between the age of 20 and 33 years (median 24.3 years) participated in the study. They were divided into two groups: well trained ($VO_2 \max \geq 60$ ml O_2/kg/min) and untrained ($VO_2 \max \leq 47$ ml O_2/kg/min). Three participants left the study during the interval between study days — one due to a joint infection not related to the study and the other two chose not to return for the second day. Further experimental procedure details can be found in [Janum et al., 2016].

3.1.2 Instrumentation

Blood samples were collected in EDTA tubes (Greiner bio-one, Germany). The samples were kept on ice until centrifuged at 4°C and 1233g for 10min, and the supernatant was stored at 80°C until analysis. Concentrations of the pro-inflammatory mediators TNF-α, IL-6, and IL-8, and the anti-inflammatory mediator IL-10 were analyzed using ELISA (Meso Scale Discovery, Rockville, Maryland,

USA). These particular mediators were analyzed as they are regarded as main drivers of the early pro-inflammatory response (TNF-α), the intermediate step between pro- and anti-inflammation (IL-6), neutrophil activation (IL-8), and the late anti-inflammatory response (IL-10).

Pressure algometry was performed by a hand-held device with a tip area of 1cm^2 applied perpendicularly on the non-dominant lateral vastus muscle of the thigh with a gradual increase in pressure until the participant indicated pain. Participants rated the pain sensation from zero to ten with zero meaning no pain and ten meaning unbearable pain. Electrocardiogram (ECG) was recorded continuously using a five-electrode system. Blood pressure (BP) was measured continuously using a photoplethysmography (Finapres Medical Systems B.V.) attached to the index finger on the non-dominant hand, which was placed at the level of the heart, secured with a sling around the neck.

3.2   Inflammatory Mediators

Day A experimental data from all 20 subjects are shown in Figure 3.2. Literature shows that in humans, the inflammatory mediators take between 6 and 8 hours to return to baseline levels after the introduction of a pathogenic agent [Copeland et al., 2005]. Thus, pseudodata was added at $t = 7$ and 8h (shown in blue), to ensure that the cytokines decayed appropriately. As explained in [Janum et al., 2016], neither nicotine administration nor training status affected the inflammatory response. Therefore, all subjects were placed in to one study population.

The population median and the data set that most closely resembles the average response are shown by the black and red lines in Figure 3.2. Box-and-whisker plots [Chambers, 1983], shown in Figure 3.3, were used to identify subjects displaying an abnormal response. Box-and-whisker plots use the median and lower and upper quartiles to identify outliers, observations that lie an abnormal distance from the other values. The interquartile range is defined as

$$\text{IQR} = Q3 - Q1,$$

where $Q3$ and $Q1$ are the 25$^{\text{th}}$ and 75$^{\text{th}}$ percentiles, respectively. The upper and lower quartiles are represented by the black error bars of Figure 3.2. In Figure 3.3, each box is comprised of the median, denoted by the red line, and the lower and upper quartiles, denoted by the bottom and top of the box. The upper and lower inner fences are used to identify the outliers and are defined as

$$\text{Upper Inner Fence: } Q3 + 1.5\text{IQR} \quad \text{and} \quad \text{Lower Inner Fence: } Q1 - 1.5\text{IQR}.$$
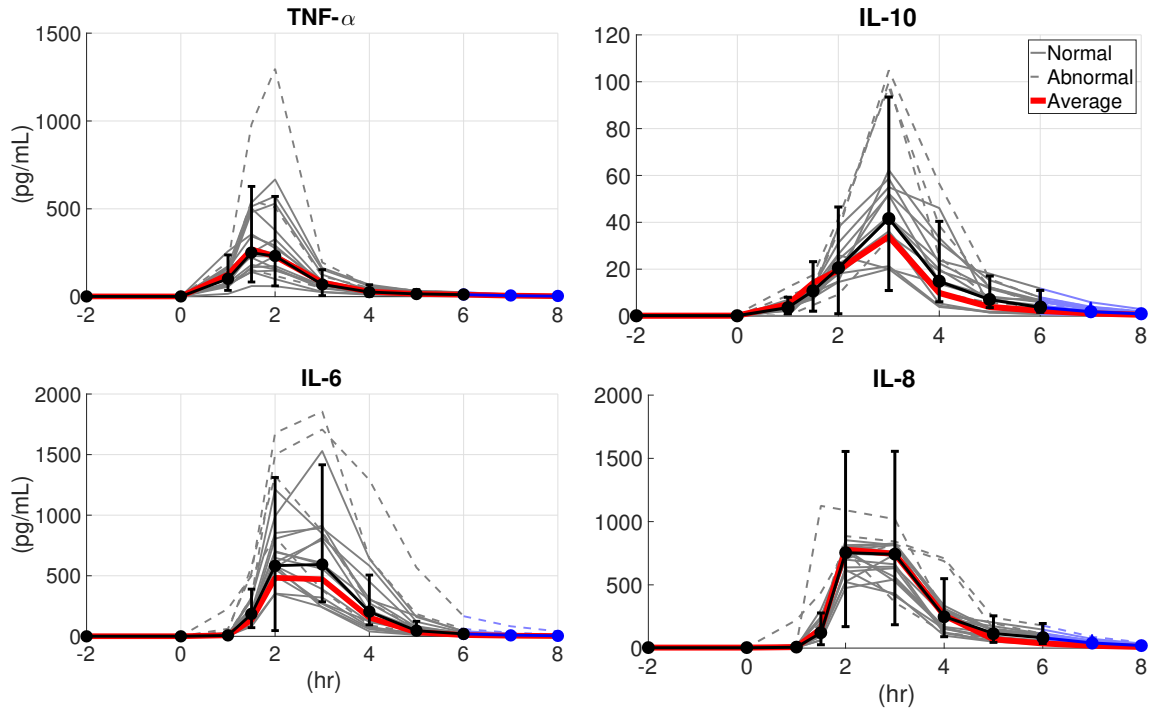
Figure 3.2 *Day A inflammatory mediator data.* Plasma cytokine responses to intravenous (i.v.) endotoxin administration in 20 healthy young men. Median (black circle), interquartile range (error bars), and the subject most in line with data mean (red) are shown. Abnormal response (identified via Box-and-Whisker plots shown in Figure 3.3) are denoted by dashed lines. Pro-inflammatory mediators, TNF-α, IL-6, and IL-8, and the anti-inflammatory mediator IL-10 levels were measured at $t = -2, 0, 1, 1.5, 2$h followed by one hour increments for the next 4 hours. Pseudodata was added at $t = 7$ and 8h to ensure that mediators decayed to baseline levels (blue). Endotoxin was administered at $t = 0$h.

Any point above the upper inner fence or below the lower inner fence is considered a mild outlier. Upper and lower outer fences are defined by

$$\text{Upper Outer Fence: } Q3 + 3\text{IQR} \quad \text{and} \quad \text{Lower Outer Fence: } Q1 - 3\text{IQR},$$

and any value outside of these fences is considered an extreme value. The whiskers represent the highest and lowest values that are not outliers.

For the inflammatory data, all outliers were considered, whether mild or extreme. The outliers are represented by the red crosses in Figure 3.3. Box-and-whisker plots identified six abnormal responses, which are indicated by the dashed lines in Figure 3.2. Outliers were first identified on an
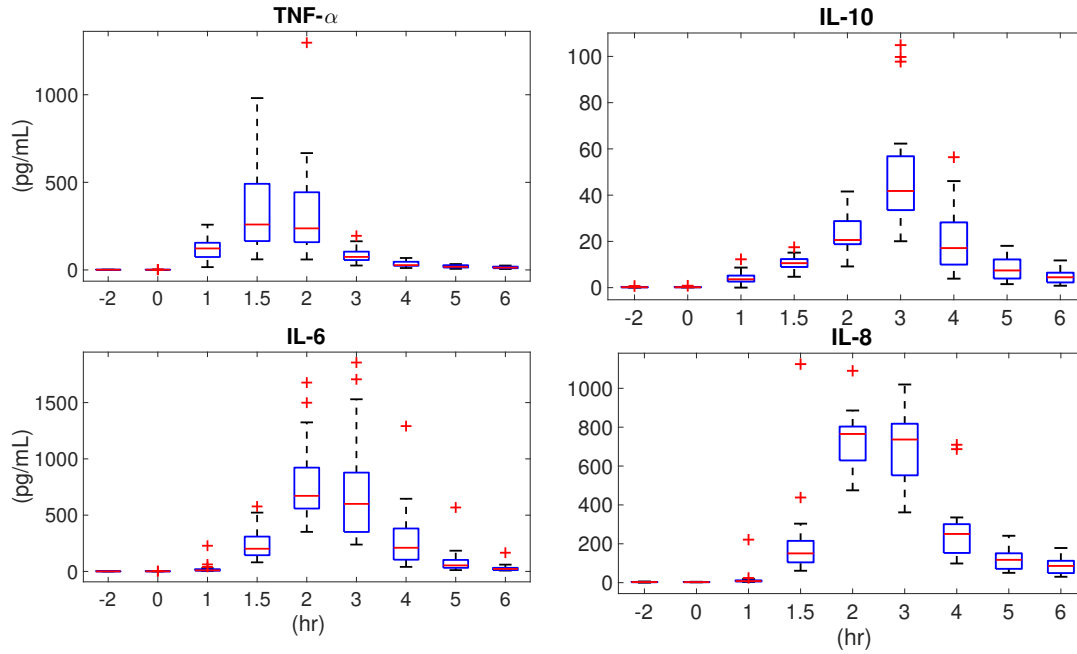
Figure 3.3 *Box-and-whisker plots of experimental data.* Twenty healthy young men were administered intravenous (i.v.) endotoxin. Data for pro-inflammatory mediators TNF-α, IL-6, and IL-8, and the anti-inflammatory mediator IL-10, collected at $t = -2, 0, 1, 1.5, 2$h and in one hour increments for the next 4 hours, were analyzed to identify outliers. For each time step, median inflammatory mediator levels are shown by red horizontal lines and the outliers are shown by the red cross.

individual basis for each inflammatory mediator. Those subjects with outliers for more than one mediator were denoted as abnormal.

3.3 Blood Pressure & Heart Rate

LabChart®[ADInstruments Inc. Colorado Springs, USA] was used to record the ECG data, which is comprised of deflections in the QRS waveforms. Heart rate (HR) is computed by dividing 60 by the duration between two consecutive QRS waveforms. Since the R wave is normally the easiest waveform to detect on the ECG, heart rate is computed from the distance between successive R waves (the RR interval). The LabChart software has built-in algorithms that detects the R waves and then computes HR. Figure 3.4 shows a zoom of the ECG recording, shown in red, and LabChart's detection of the peaks of the QRS-complex. Heart rate data for two individuals are shown in Figure 3.5. The discontinuity in the response is due to the sensitivity of the ECG to movements of the chest,
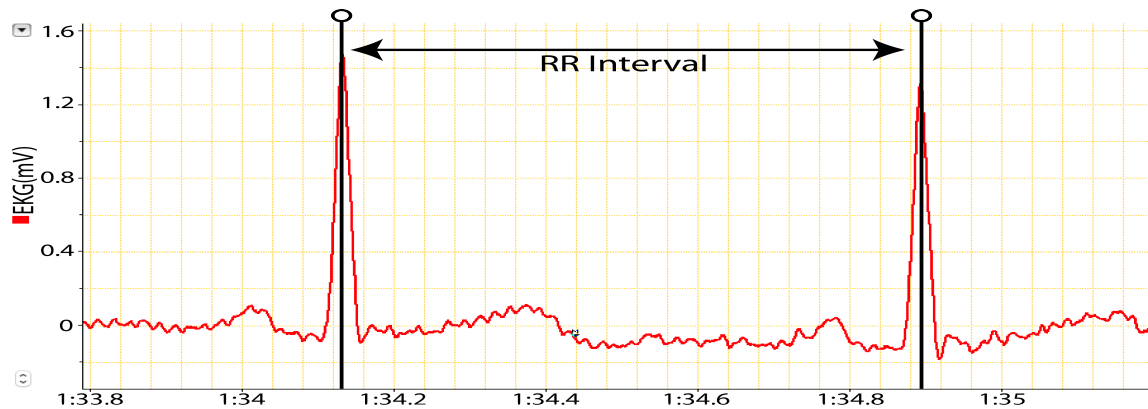
Figure 3.4 *Zoom of electrocardiogram recording.* Heart rate is computed by dividing 60 by the length be-tween two consecutive QRS waveforms. `LabChart` has built-in algorithms that can identify the peak of each waveform and then compute HR.

causing measurement noise. Movements can also be caused by motion artifacts, as shown in the top zoomed portion of Figure 3.5. Additionally premature heart beats, called ectopic beats, can also cause great fluctuations in HR. This is shown in the bottom zoomed portion of Figure 3.5.

Heart rate variability (HRV) was studied by analyzing the distance between successive RR-intervals. Five-minute intervals of ECG data were extracted to form a tachogram, where the distance between each RR-interval is plotted against time. HRV parameters including 1) the standard de-viation of the average beat-to-beat intervals (SDANN), 2) the percentage of interval differences of successive interbeat intervals greater than 50 ms (pNN50), 3) the high frequency variability (HF), and 4) the low frequency/high frequency ratio (LF/HF), were analyzed. These values were obtained using `LabChart`'s built-in HRV Toolbox and are shown in Figure 3.6 for a representative subject. Each of these parameters give a measure of the total heart rate variability and the amount of parasympathetic and sympathetic activity present.

The finapres used to record BP is very sensitive to movement. Thus, the experimentalists were unable to obtain continuous measurements of BP throughout the entirety of the experiment. Figure 3.7 on page 27 shows the mean arterial blood pressure data for two individuals.

3.4 Data Preprocessing

The objective of this thesis is to understand the interaction between the inflammatory response and the cardiovascular dynamics. As will be shown in Chapter 7, temperature is used as an input to predict heart rate. From Figure 3.8, it is clear that the temperature data is sparse compared to the
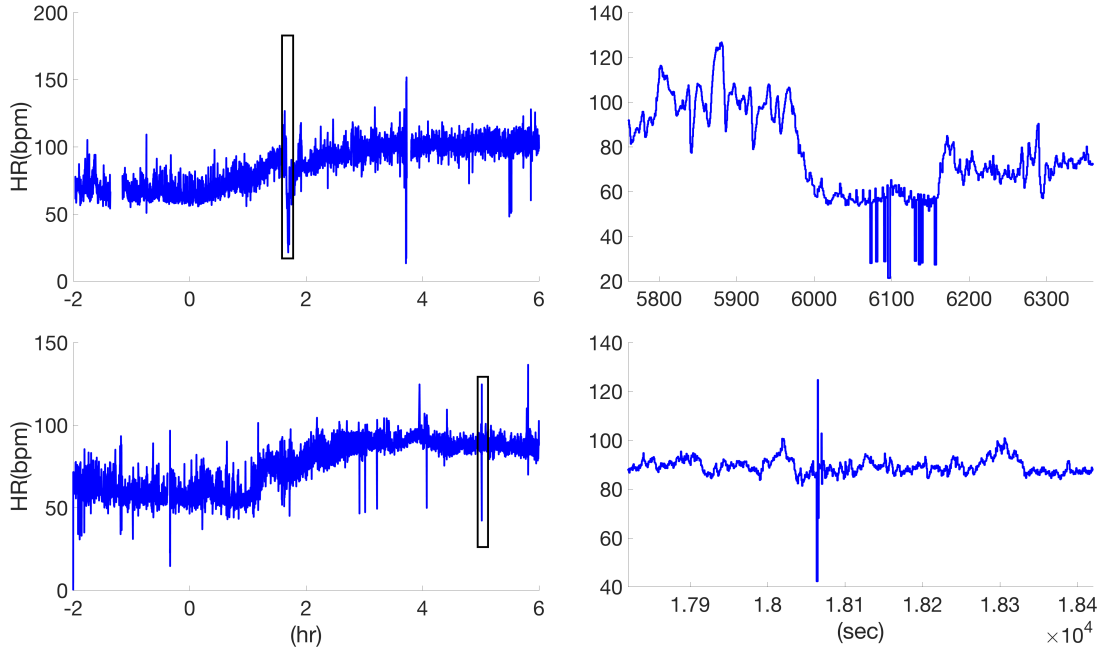
Figure 3.5 *Heart rate data for two individuals.* (Top) Heart rate computed from the ECG data, collected continuously throughout the experiment. Zoom on right shows ectopic beats and motion artifacts in the data.

heart rate data shown in Figure 3.5. Thus, the mean heart rate will be predicted.

To obtain the mean heart rate from the HR data, we used the Savitzky-Golay smoothing filter. This method is based on a local least-squares polynomial approximation to each window of data by a polynomial of fixed degree n. Savitzky-Golay filters are typically used to smooth data that even without noise, span a large range of frequencies. In comparison to standard averaging filters such as the moving average filter, which smooths data by replacing each data point with an average of its neighbors, Savitzky-Golay filters perform much better. One caveat to that is its inability to reject large levels of noise [Orfanidis, 1995]. Due to the change observed in the HR over the course of the experiment and minimal amount of noise, Savitzky-Golay was the most appropriate smoothing filter to use.

The Savitzky-Golay filter acts on a vector of input samples $x_1, \ldots, x_j$ to produce a smoothed vector $y_1, \ldots, y_j$. For a particular point x_ℓ, a window of $N = 2M + 1$ samples is created with $x_\ell = x(0)$ at the center. Given the samples $x(-M), \ldots, x(0), \ldots, x(M)$, the best least-squares fit is determined by an n-degree polynomial p. The smoothed output $y(0) = y_\ell$ is given by the center of the polynomial
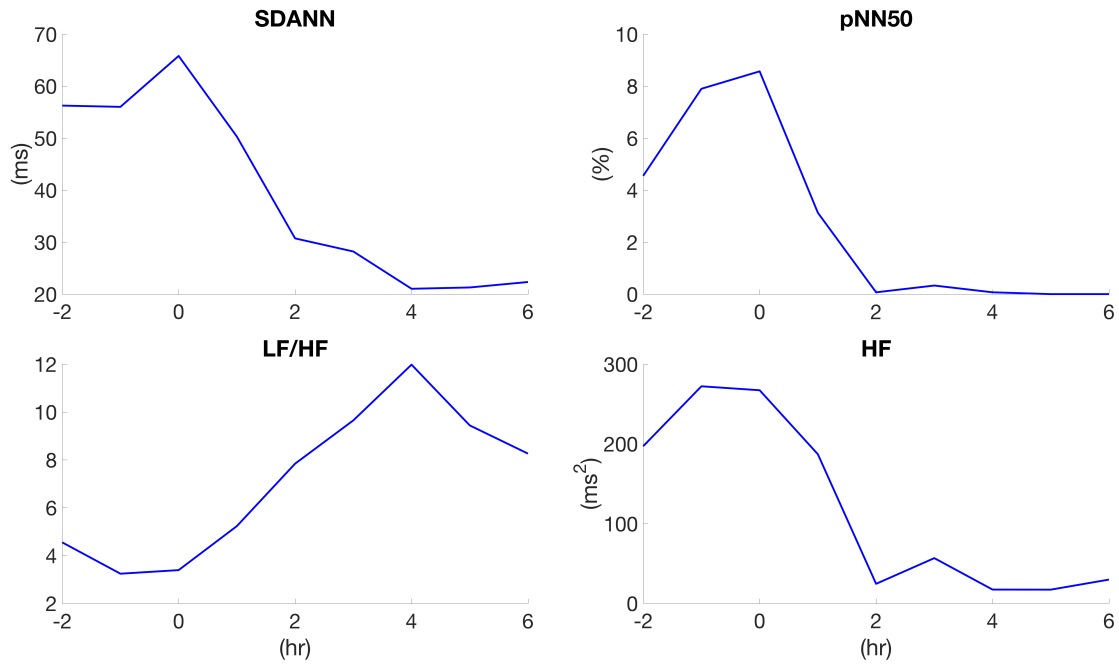
Figure 3.6 *Heart rate variability measures obtained from ECG data for one representative subject.* HRV measures were collected from 5-minute intervals of ECG data extracted from the tachogram. 1) The standard deviation of the average beat-to-beat intervals (SDANN), 2) the percentage of interval differences of successive interbeat intervals greater than 50 ms (pNN50), 3) the high frequency variability (HF), and 4) the low frequency/high frequency ratio (LF/HF). Each value was recorded using `LabChart`'s ®built-in HRV Toolbox.

$p(0)$. Shifting the window by k time steps creates another set of samples $x(k-M), \ldots, x(k+M)$. An n-degree polynomial is fitted to the samples and the smoothed output $y(k)$ is given by the center of the polynomial $p(k)$. Near the endpoints, where the window extends beyond the beginning or end of the input samples, a symmetric extension of the signal can be used [Persson & Strang, 2003].

The built-in `smooth` function in `MATLAB` was used to smooth the HR data. Figure 3.9 shows the smoothed data. Each segment of data was smoothed using a 2-degree polynomial and a 5-degree polynomial. Linear splines were used to connect the data between segments. While the 5-degree polynomial is able to capture the transient behavior of the segment from $t = -2$ to $t = -1.3$, it is more sensitive to the apparent noise around $t = 2$, when compared to the 2-degree polynomial fit. Thus, choosing an appropriate degree polynomial to approximate the data is greatly dependent upon the behavior of the data. Each segment can be estimated by polynomials of varying degrees. Note that too much smoothing the data removes the heart rate variability as shown in the zoomed
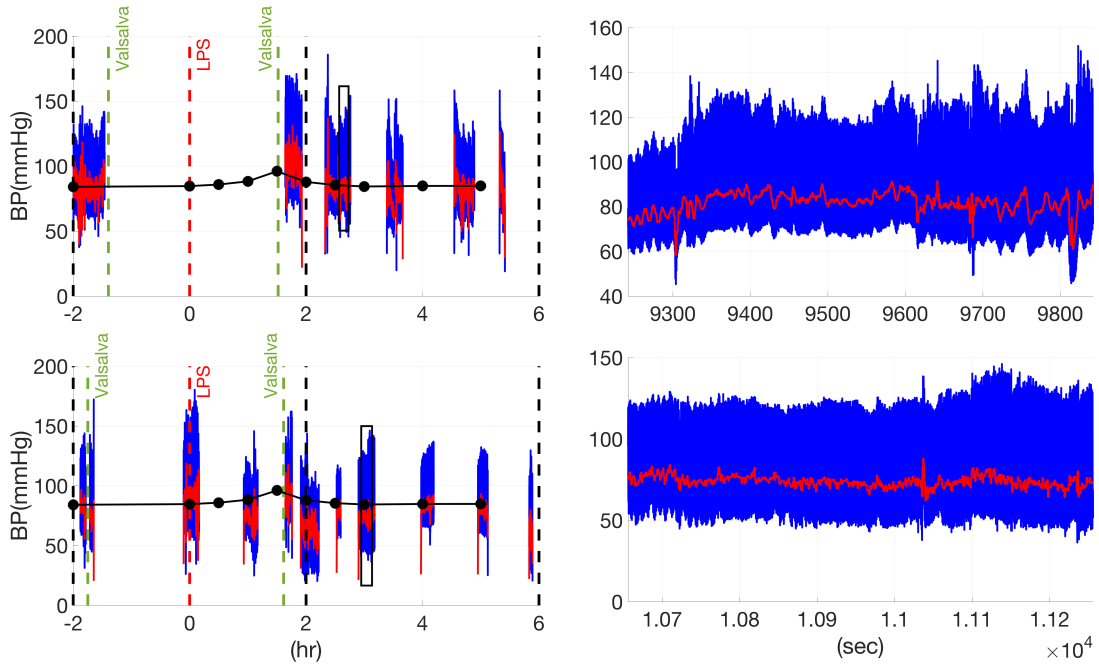
Figure 3.7 *Arterial and mean arterial blood pressure for two individuals.* Arterial blood pressure (blue) recorded using a finapres for two individuals (zoom on right). Mean arterial blood pressure is shown in red. Due to the sensitivity of the finapres to the participants' movements due to the events of the experiment, BP data could not be continuously recorded. Events are denoted by dashed lines (black–pain, green–Valsalva, red-LPS). Temperature was also recorded at discrete time points throughout. See Figure 3.1 for protocol. Black circles represent the mean blood pressure over all normal data sets.

portions in Figure 3.9.

Mean arterial blood pressure was also measured using a blood pressure cuff at $t = 0, 1, 2, 2.5, 3, 3.25, 3.5, 3, 75$, and 4hr and then every 30 minutes for the remainder of the experiment. This cuff pressure was used to calibrate the arterial blood pressure obtained by the finapres. Pressure measurements during experimental events were removed since these events will not be modeled here.
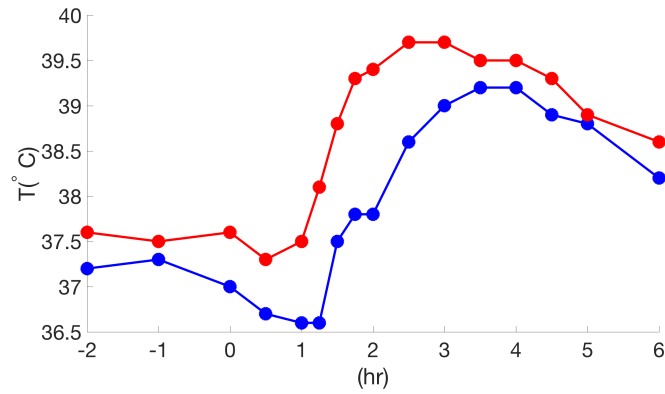
Figure 3.8 *Temperature data for two individuals.* Temperature was collected periodically throughout the experiment, using an oral thermometer.
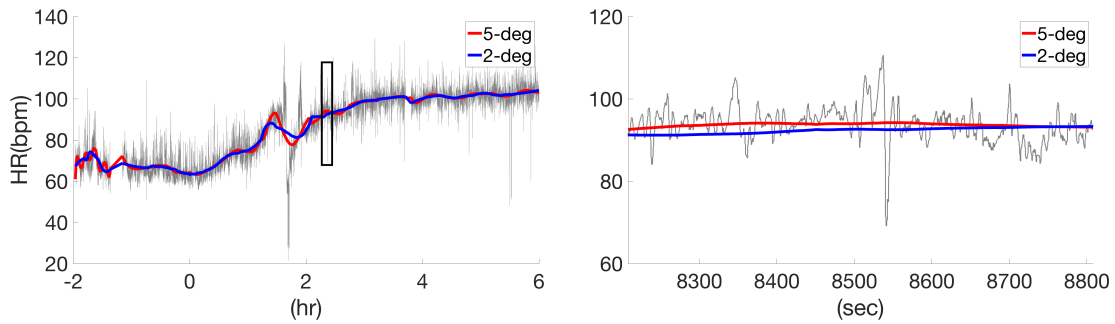
Figure 3.9 *Smoothed HR data, using a Savitzky-Golay smoothing filter.* Smoothing with 5-degree and a 2-degree polynomial are shown by the red and blue lines, respectively (zoom on right). Each segment of data was connected by linear splines. Data was smoothed using the `smooth` function in MATLAB.

CHAPTER

4

SENSITIVITY ANALYSIS, IDENTIFIABILITY, & PARAMETER ESTIMATION

To develop a mathematical model that can accurately fit experimental data, it is typical to utilize optimization methods to find a parameter set that minimizes the least squares error between the model output and the data. The first step in finding an optimal parameter set is analyzing the model and data to determine a subset of the parameters to be optimized. To do so, we use sensitivity and identifiability analysis. Subsequently, parameters can be estimated to solve the inverse problem.

This chapter introduces these concepts, using a mathematical model of the spread of disease by contact with an infected person. The model is discussed in Section 4.1. *Sensitivity analysis* and *identifiability analysis* are introduced in Sections 4.3 and 4.4. In Section 4.5, parameter estimation techniques, including simplex methods and gradient-based methods, are described. Finally, Sections 4.6 discusses the *frequentist* and *Bayesian* methods used to quantify the amount of uncertainty in the model. All methods described in this chapter can be implemented using the `MATLAB` code, discussed in detail in Appendix A. The chapter will conclude with a discussion of the methods used and the results obtained.
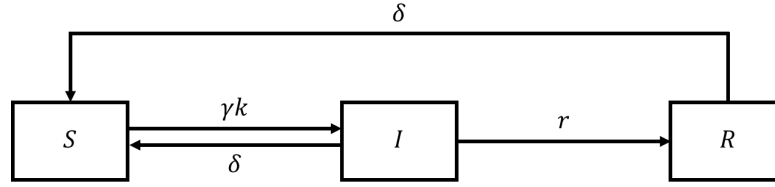
Figure 4.1 *Modified SIRS model (mSIRS).* The total population N is subdivided into susceptible (S), infectious (I), and recovered (R). γ describes how the infection is transmitted between S and I, k denotes the degree of the interaction between S and I, r is the recovery rate, and δ is the rate at which an individual rejoins the susceptible population; note δ is independent of the infection.

4.1   Introduction

Infections caused by viruses and bacteria reproduce within their host and are transmitted directly from one host to another. To model the interactions between the infected and uninfected populations, its members can be subdivided into distinct classes, depending on the health of the individuals. Most commonly, the population is divided into the susceptible population S, infectious population I, and recovered population R. Depending on whether the recovered population have full or temporary immunity to the virus or bacteria, the model is either an SIR or SIRS model, respectively [Edelstein-Keshet, 2005].

The most common SIR model contains two transition rates: γ denotes how the infection is transmitted between S and I, and r denotes the recovery of the infectious population. As an extension of the SIR model, the SIRS model includes a constant δ, denoting the rate at which an individual rejoins the susceptible population after recovery. The example presented in this chapter is a modification of the SIRS model, in that it takes into account the movement of the infectious population back to the susceptible population, at the same rate δ. The diagram shown in Figure 4.1 summarizes the transition between the three populations. The model is motivated by the SIR model by [Smith, 2016].

Mathematically, these interactions can be modeled by the ordinary differential equations (ODEs) of the form

$$
\begin{aligned}
\frac{dS}{dt} &= \delta I + \delta R - \gamma k S I \\
\frac{dI}{dt} &= \gamma k S I - r I - \delta I, \\
\frac{dR}{dt} &= r I - \delta R,
\end{aligned}
\tag{4.1}
$$
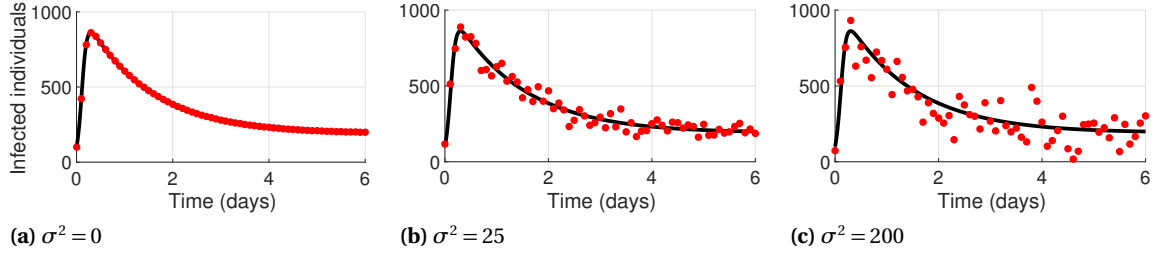
Figure 4.2 *mSIRS model output $y = I$ (black line) with simulated data (red dots) using varying levels of σ^2.*

where k denotes the degree of the interaction between S and I. The rate of transmission of the virus or bacteria is proportional to the rate of encounter of susceptible and infectious individuals, modeled by $\gamma k S I$. The sum of the three ODEs is zero, thus the total population $N = S + I + R$ must be a constant and one variable, say R, can be eliminated, reducing (4.1) to two ODEs given by

$$\frac{dS}{dt} = \delta(N - S) - \gamma k S I$$
$$\frac{dI}{dt} = \gamma k S I - r I - \delta I. \tag{4.2}$$

Synthetic Data

For the modified SIRS model, hereafter referred to as the mSIRS model, we assume that the true parameters $(\delta, \gamma, k, r, N)$ and the initial conditions $[S_0, I_0]$ are known to be $(0.15, 0.2, 0.1, 0.6, 1000)$ and $[900, 100]$, respectively. To illustrate the concepts of sensitivity analysis, identifiability, and parameter estimation, synthetic data is generated for the population of infected individuals by simulating the model forward and then adding independent and identically distributed (i.i.d.) noise from a normal distribution with variance σ^2. The synthetic data, as well as the model output, for the infected individuals are shown in Figure 4.2, for (a) $\sigma^2 = 0$, (b) $\sigma^2 = 25$, and (c) $\sigma^2 = 200$.

Generalized Model Formulation

In general, an ordinary differential equation (ODE) model of the form (4.2) can be written as a system of nonlinear differential equations of the form

$$\frac{dx}{dt} = f(t, x, \theta), \qquad x(t_0) = x_0, \tag{4.3}$$
$$y = g(t, x, \theta), \tag{4.4}$$

31

where $x \in \mathbb{R}^n$ denotes the state vector, $t \in \mathbb{R}^T$ denotes time, $\theta \in \mathbb{R}^q$ denotes the parameter vector, $x_0 \in \mathbb{R}^n$ is the associated initial conditions, and $y \in \mathbb{R}^m$ is the model output. For the mSIRS model shown in equation (4.2), $x = [S, I]$, $\theta = (\delta, \gamma, k, r, N) \in \mathbb{R}^5$, and the model output is $y = I$.

For the analysis done here, we assume that given N observations of the model output at times $t_0, t_1, \ldots, t_N$, the data can be expressed as

$$Y_i = g(t_i, x(t_i), \theta) + \epsilon_i, \qquad i = 1, 2, \ldots, N, \text{ where } \epsilon_i \sim \mathcal{N}(0, \sigma^2) \tag{4.5}$$

for some unknown variance σ^2 [Banks et al., 2009]. The data shown in Figure (4.2) can be expressed in this form, where σ^2 is known to be either 0, 25, or 200.

4.2 Least Squares Formulation

To fit the mathematical model to the data, an inverse least squares formulation is used to find a parameter set that minimizes the least squares error between the model output and the data. The residual vector is given by $R = (r_1, r_2, \ldots, r_N)^T$, where $r_i = g(t_i, x(t_i) - Y_i, \theta), i = 1, 2, \ldots, N$ and the least squares error J is defined as

$$J(\theta) = R^T R. \tag{4.6}$$

Then the optimal parameter set is given by

$$\hat{\theta} = \arg\min_{\theta} J(\theta). \tag{4.7}$$

Sensitivity and identifiability analysis are used to lessen the complexity of the optimization problem by determining a subset of sensitive and uncorrelated parameters.

4.3 Sensitivity Analysis

Sensitivity analysis can be used to assess the variation of the model output in response to small perturbations in the parameter values. Sensitivities can be computed on either a local or global level. *Local sensitivity analysis* quantifies how a model changes in response to small perturbations of the model parameters, while *global sensitivity analysis* describes how a model changes in response to varying the parameters over a subspace of the parameter space [Kiparissides et al., 2009]. The methods described here will focus on local sensitivities.

Assuming a model output $y = I$, given by solving (4.2), the sensitivity matrix χ is defined by

$$
\chi = \frac{\partial y}{\partial \theta} = \begin{bmatrix} \frac{\partial y_1(t_1)}{\partial \theta_1} & \cdots & \frac{\partial y_1(t_1)}{\partial \theta_q} \\ \vdots & \ddots & \vdots \\ \frac{\partial y_1(t_N)}{\partial \theta_1} & \cdots & \frac{\partial y_1(t_N)}{\partial \theta_q} \\ \frac{\partial y_2(t_1)}{\partial \theta_1} & \cdots & \frac{\partial y_2(t_1)}{\partial \theta_q} \\ \vdots & \ddots & \vdots \\ \frac{\partial y_m(t_N)}{\partial \theta_1} & \cdots & \frac{\partial y_m(t_N)}{\partial \theta_q} \end{bmatrix}, \tag{4.8}
$$

where $y_i(t_j)$ is the ith model output evaluated at time t_j. For simple problems where an analytical solution of the ODEs can be obtained, the sensitivities can be computed analytically [Banks & Tran, 2009; Ellwein, 2008; Valdez-Jasso et al., 2008], while more complex models require numerical evaluation. The latter can be done using numerical methods, including *automatic differentiation* [Griewank, 1989] and *finite differencing*.

From (4.3), sensitivities of the model output to the parameters $\frac{\partial x}{\partial \theta}$ can be computed from the sensitivity equations

$$
\frac{d}{dt}\left(\frac{\partial x}{\partial \theta}\right) = \frac{\partial}{\partial \theta}\left(\frac{dx}{dt}\right) = \frac{df}{dx}\frac{\partial x}{\partial \theta} + \frac{df}{d\theta}.
$$

The parameter Jacobian $\frac{df}{d\theta}$ and the model Jacobian $\frac{df}{dx}$ can be computed analytically, using automatic differentiation, or via finite differences. From this, the sensitivity matrix χ can be computed using the chain rule on the output function $y = g(t, x(t, \theta), \theta)$.

For the mSIRS model, the model output is $y = I$ and the sensitivity matrix is given by

$$
\chi = \begin{pmatrix} I_\delta(t_1) & I_\gamma(t_1) & I_k(t_1) & I_r(t_1) \\ \vdots & \vdots & \vdots & \vdots \\ I_\delta(t_N) & I_\gamma(t_N) & I_k(t_N) & I_r(t_N) \end{pmatrix},
$$

where $I_{\theta_i} = \frac{\partial I}{\partial \theta_i}$, for $\theta_i \in (\delta, \gamma, k, r)$. This can be computed analytically by finding solutions to the

system of ODEs given in (4.2), along with the sensitivity equations given by

$$\frac{dS_\delta}{dt} = -\delta S_\delta - \gamma k S I_\delta - \gamma k S_\delta I + (N-S) \qquad \frac{dI_\delta}{dt} = \gamma k S I_\delta + \gamma k S_\delta I - (r+\delta)I_\delta - I$$

$$\frac{dS_\gamma}{dt} = -\delta S_\gamma - \gamma k S I_\gamma - \gamma k S_\gamma I - k S I \qquad \frac{dI_\gamma}{dt} = \gamma k S I_\delta + \gamma k S_\gamma I - (r+\delta)I_\gamma + k S I$$

$$\frac{dS_k}{dt} = -\delta S_k - \gamma k S I_k - \gamma k S_k I - \gamma S I \qquad \frac{dI_k}{dt} = \gamma k S I_k + \gamma k S_k I - (r+\delta)I_k + \gamma S I$$

$$\frac{dS_r}{dt} = -\delta S_r - \gamma k S I_r - \gamma k S_r I \qquad \frac{dI_r}{dt} = \gamma k S I_r + \gamma k S_r I - (r+\delta)I_r - I,$$

where $S_{\theta_i} = \frac{\partial S}{\partial \theta_i}$ for $\theta_i \in (\delta, \gamma, k, r)$.

The simplest, but least accurate way, to compute sensitivities numerically is via forward differences, where the solutions are first order accurate and are computed from the first term in the Taylor series expansion as

$$\chi_{\theta_j}(t_i) = \frac{g(t_i, x(t_i), \theta + h e_j) - g(t_i, x(t_i), \theta)}{h}, \tag{4.9}$$

where h is a step based on the precision of the model output; if the relative error tolerance of the ordinary differential equation (ODE) is φ, then $h = \sqrt{\varphi}$. The variable e_j represents the unit vector in the jth direction [Pope et al., 2009]. The advantage of forward differences is that they are easy to compute, requiring $q+1$ evaluations of the model output. On the other hand, sensitivities computed using a central difference scheme given by

$$\chi_{\theta_j}(t_i) = \frac{g(t_i, x(t_i), \theta + h e_j) - g(t_i, x(t_i), \theta - h e_j)}{2h} \tag{4.10}$$

are 2nd order accurate, yet they require $2q$ evaluations of the model.

Since the parameter values and model output may have different units, it may be beneficial to instead compute the relative sensitivity matrix, given by

$$\tilde{\chi} = \frac{\partial y}{\partial \theta} \frac{\theta}{\bar{y}}, \tag{4.11}$$

where $\bar{y}$ is the mean, max, or another characteristic value for y. Given that sensitivities are evaluated at a fixed parameter value, typically the nominal or the optimal parameter values, the sensitivities are valid locally in a region near the parameter values. A global sensitivity may be more beneficial if the parameters exhibit a high level of uncertainty [Kiparissides et al., 2009] or if the model is highly nonlinear.

34

(a) Time varying sensitivities.

(b) Ranked sensitivities using the 2-norm of the sensitivity matrix.
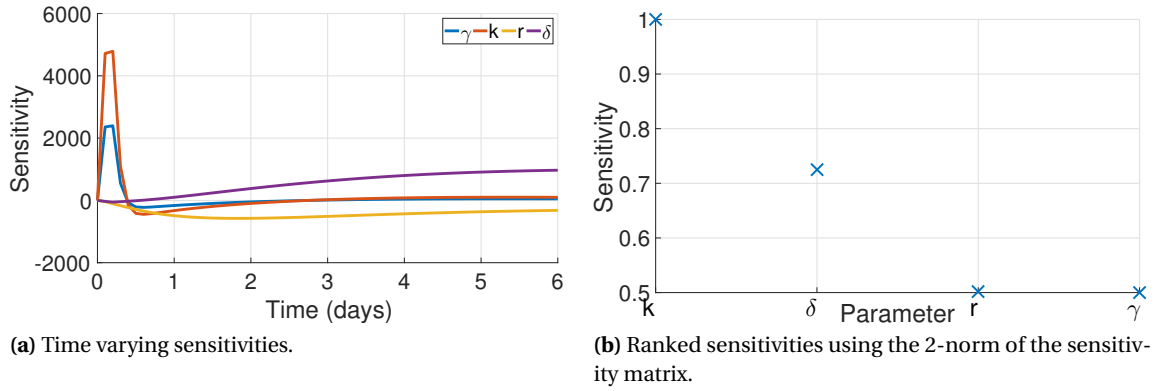
Figure 4.3 *Sensitivities of the mSIRS model.* (a) Sensitivity of each parameter with respect to time and (b) ranked sensitivities.

To compare the sensitivities between the parameters, the ranked sensitivities can be computed by, for instance, taking the norm of the sensitivity matrix ($\|\chi\|_\infty, \|\chi\|_2$), or finding the area under the curve. The method chosen depends on the behavior of the sensitivity curves. For the mSIRS model, sensitivities are ranked using the two-norm, $\|\chi\|_2$. If φ is the integration tolerance in numerically solving the differential equations and the sensitivities are computed using finite differences, then the error of the sensitivities are $\mathcal{O}(\sqrt{\varphi})$ [Pope et al., 2009]. Since the error of the sensitivities is an approximation, the cutoff is set at $\phi = 10\sqrt{\varphi}$. This cutoff separates the parameters into the p sensitive and $q - p$ insensitive parameters. The parameters of the mSIRS model have been ranked using the two-norm after computing the relative sensitivities with the forward difference approximation. Based on the results of this analysis, shown in Figure 4.3, and using a cutoff of $\phi = 10\sqrt{10^{-8}}$ it can be concluded that all four parameters are sensitive.

4.4 Identifiability Analysis & Subset Selection

A parameter is identifiable if it can be uniquely determined. Two types of identifiability will be discussed here: *practical* and *structural* identifiability.

4.4.1 Structural Identifiability

Definition 1. *Structurally Identifiable. The system given by (4.3) and (4.4) is structurally identifiable if a meromorphic function*

$$\Phi = \Phi(\theta, y, \dot{y}, \ldots, y^{(k)}), \Phi \in \mathbb{R}^q,$$

can be constructed after a finite number of steps of algebraic calculation or differentiation such that $\Phi = 0$ *and* $\det \frac{\partial \Phi}{\partial \theta} \neq 0$ *hold on the interval* $[t_0, t_1]$ *for any* (θ, x_0) *in an open and dense subset of* $\Theta \times M$, *where k is any positive integer and* $\dot{y}, \ldots, y^{(k)}$ *are the derivatives of y.*

This definition states that a system is structurally identifiable if and only if it is possible to uniquely determine the parameter values given the model output for all possible input functions. Structural identifiability considers the structure of the mathematical model, not the data.

Input-Output Equation

For the mSIRS model, structural identifiability can be determined by computing the input-output equation [Bearup et al., 2013]; that is, the equation of the model output y as a function of the parameters θ. Since $y = I$, the system in (4.2) can be rewritten as

$$\dot{S} \;=\; \delta(N-S)-\gamma k S y \tag{4.12}$$

$$\dot{y} \;=\; \gamma k S y - (r+\delta)y, \tag{4.13}$$

where $\dot{S} = \frac{dS}{dt}$ and $\dot{y} = \frac{dy}{dt}$. Solving $\dot{y}$ for S yields

$$S = \frac{\dot{y} + y(r+\delta)}{\gamma k y}.$$

Differentiating this and substituting it back into (4.12) gives

$$\delta N - \left(\frac{\delta \dot{y} + \delta(r+\delta)y}{\gamma k y} \right) - \dot{y} - (r+\delta)y = \frac{y\ddot{y} - (\dot{y})^2}{\gamma k y^2}$$

$$\implies (\delta N \gamma k - \delta r - \delta^2)y^2 - (\gamma k r + \delta \gamma k)y^3 - \delta y \dot{y} - \gamma k y^2 \dot{y} + \dot{y}^2 - y\ddot{y} = 0. \tag{4.14}$$

Now suppose there is an alternative parameter set $\overline{\theta} = (\overline{\delta}, \overline{\gamma}, \overline{k}, \overline{r})$ satisfying (4.14). Then

$$\delta N \gamma k - \delta r - \delta^2 \;=\; \overline{\delta} N \overline{\gamma} \overline{k} - \overline{\delta}\,\overline{r} - \overline{\delta}^2$$

$$\gamma k r + \delta \gamma k \;=\; \overline{\gamma}\overline{k}\overline{r} + \overline{\delta}\overline{\gamma}\overline{k}$$

$$\delta \;=\; \overline{\delta}$$

$$\gamma k \;=\; \overline{\gamma}\overline{k}.$$

Solving these equations for the $\overline{\theta}$ gives

$$\delta = \overline{\delta}, \quad r = \overline{r}, \quad \gamma k = \overline{\gamma}\overline{k}.$$

Thus, δ and r are structurally identifiable and γ and k are structurally unidentifiable. By definition, a model is structurally unidentifiable if any parameter is unidentifiable, so the mSIRS model is structurally unidentifiable. Thus, either γ or k can be set to its nominal value, while the other is analyzed for practical identifiability. The decision between the two parameters is dependent upon the structure of the model, as well as the available data. For this study, the least sensitive parameter, γ, is fixed at its nominal value, while the other parameters are analyzed further.

4.4.2 Practical Identifiability

Definition 2. *Practically Identifiable. The system given by equations (4.3) and (4.4) is practically identifiable if θ can be uniquely determined from the measurable system output $y(t)$ [Miao et al., 2011].*

Unlike structural identifiability, practical identifiability depends on both the structure of the mathematical model and the data. Structurally identifiability is a necessary but not sufficient condition for practical identifiability so the mSIRS model is not practically identifiability [Miao et al., 2011; Olufsen & Ottesen, 2013]. In a biological sense, it may be important to determine what parameters can be included in this subset. To demonstrate the importance of practical identifiability, we will include all four parameters in the analysis and show that the model is also not practically identifiable.

Two methods for practical identifiability analysis will be presented here: the *structural correlation method (SCM)* [Olufsen & Ottesen, 2013] and *singular value decomposition followed by QR factorization* [Pope et al., 2009]. The structural correlation method is based on the structured analysis of parameter correlations from the covariance matrix. Using singular value decomposition (SVD) on the sensitivity matrix followed by QR decomposition identifies a set of identifiable parameters that are sensitive as a group, rather than individually. Other methods for subset selection include the orthogonal method and the eigenvalue method, which is closely related to the method of SVD followed by QR factorization. For a full description of these methods, please see the review by Miao et al. [2011].

The methods presented here are local methods that will find an identifiable parameter subset in a given neighborhood of the parameter values. Global methods, such as the sampling method used by the Delayed Rejective Adaptive Metropolis (DRAM) algorithm, which will be discussed in section 4.6.2, are able to identify pairwise parameter correlations, both linear and nonlinear. However, these methods are far more computationally expensive than the local methods.

Structural Correlation Method

The structural correlation method examines pairwise linear correlations between parameters by analyzing the model covariance matrix $C = F^{-1}$, where F is the Fisher information matrix (FIM), a non-negative symmetric matrix defined by

$$F = \chi^T \chi, \quad \text{where} \quad \chi = \frac{\partial y}{\partial \theta}.$$

The methodology is developed by considering the first order Taylor expansion of the system output given in (4.4) at a point θ^* near the nominal parameter vector θ

$$y_i(\theta^*) = g(t_i, x(t_i), \theta^*) \approx y(t_i, x(t_i), \theta) + \frac{\partial y(t_i, x(t_i), \theta)}{\partial \theta)}(\theta^* - \theta), \tag{4.15}$$

where $i = 1, 2, \ldots k$. By definition, $y(t_i, x(t_i), \theta)$ is the measurement at t_i without error. Letting $\Delta\theta = \theta^* - \theta$, the residual sum of squares between the exact measurement and the linear approximation is

$$
\begin{aligned}
J(\theta) &= \sum_{i=1}^{d} \Big[y(t_i, x(t_i), \theta) - y(t_i, x(t_i), \theta) - \frac{\partial y(t_i, x(t_i), \theta)}{\partial \theta)}(\theta^* - \theta) \Big]^2 \\
&= \sum_{i=1}^{d} \Big[-\frac{\partial y(t_i, x(t_i), \theta)}{\partial \theta)}(\theta^* - \theta) \Big]^2 \\
&= (\chi \Delta\theta)^T \chi \Delta\theta,
\end{aligned}
\tag{4.16}
$$

The minimum of $J(\theta)$ is reached when $F\Delta\theta = 0$. If F has full rank, then the unique solution of $F\Delta\theta = 0$ is $\hat{\theta} = \theta$. This implies that the model parameters θ^* are locally identifiable at θ. If F is singular, then there exists at least one non-trivial solution $\hat{\theta} \neq \theta$. Thus, the model parameters are unidentifiable [Miao et al., 2011]. It should be noted that global identifiability cannot be inferred from this analysis since the linear approximation is used in (4.15).

If F is not of full rank, then two or more parameters are related. Correlations can be computed from the covariance matrix as

$$c_{ij} = \frac{C_{ij}}{\sqrt{C_{ii}C_{jj}}}. \tag{4.17}$$

If a parameter pair shows a strong correlation, that is if $|c_{ij}| > \zeta$ for $\zeta \to 1$, then it is not feasible to estimate both parameters. Thus, one parameter, can be removed from the subset and the correlations recalculated for the new subset. For the analysis presented here, the least sensitive parameter will be removed from the subset. Unfortunately, no theoretical predictions exists to define an appropriate

value for ζ; it is generally chosen to be relatively close to 1.

NOTE: The covariance matrix cannot be computed if $\chi^T \chi \in \mathbb{R}^q$ is singular or close to singular. The condition number of $\chi^T \chi$ gives a measure of how close the matrix is to singular. The condition number is defined as

$$\kappa(\chi^T \chi) = \frac{\sigma_1}{\sigma_q},$$

where σ_1 and σ_q are the largest and smallest singular values of χ, respectively. The smallest singular value is given by $\sigma_q(\chi) = \sqrt{\lambda_q(\chi^T \chi)}$, where λ_q is the smallest eigenvalue of χ. If the condition number is large, then the matrix is ill-conditioned and thus, close to singular. If λ_q is small, then $\kappa(\chi)$ will be large. If this is the case, then correlations will have to be manually removed by analyzing the relationships between the parameters of the model and then removing the columns of the sensitivity matrix χ corresponding to the correlations.

Algorithm 1. *Structured Correlation Method Algorithm*

1. *Check that $\chi^T \chi$ is nonsingular.*

2. *Compute c using (4.17) and identify all correlated parameters. That is, determine all parameter pairs for which $|c_{ij}| > \zeta$.*

3. *For the parameter pair with the largest $|c_{ij}|$, remove the least sensitive parameter.*

4. *Continue from 1 until $|c_{ij}| < \zeta, \forall i, j$.*

The parameters of the mSIRS model have been analyzed for pairwise correlations using the correlation coefficients defined above. The correlation cutoff ζ was chosen to be on the interval $[0.90, 1)$. As shown in Figure 4.3, the ranked sensitivities (from most to least sensitive) are $\theta = (k, \delta, r, \gamma)$. If the parameter γ is included in the SCM analysis, the correlation matrix

$$c = \begin{matrix} & \gamma & k & r & \delta & \\ & \begin{bmatrix} 0 & -1 & 0.0251 & 0.0212 \\ & 0 & -0.0251 & -0.0212 \\ & & 0 & 0.8216 \\ & & & 0 \end{bmatrix} & \begin{matrix} \gamma \\ k \\ r \\ \delta \end{matrix} \end{matrix}, \tag{4.18}$$

reveals that k and γ are correlated. Fixing γ and recomputing the correlation matrix results in no correlations between the remaining three parameters k, δ, and r. The condition number of the Fisher information matrix, prior to removing γ, was $\kappa(\chi^T \chi) = 3.23 \times 10^7$, making it evident that

$\chi^T \chi$ is close to singular. Thus, it is not surprising that γ and k have a correlation coefficient exactly equaled to 1. After removing γ, the condition number of $\chi^T \chi$ became $\kappa(\chi^T \chi) = 16.72$.

SVD Decomposition Followed by QR Factorization

While the SCM determines the identifiable parameters among a subset of sensitive parameters, singular value decomposition followed by QR factorization can be used on the nominal set to determine parameters that are both sensitive and identifiable. It does so by using singular value decomposition to obtain a numerical rank of the sensitivity matrix S. This numeral rank is then used to determine ρ, the number of identifiable parameters.

Algorithm 2. *Singular Value Decomposition Followed by QR Factorization*

1. *Compute the singular value decomposition $\chi = U \Sigma V^T$, where Σ is a diagonal matrix containing the singular values of χ in decreasing order and V is an orthogonal matrix of right singular vectors.*

2. *Determine ℓ, the smallest allowable singular value by analyzing the relative error tolerance of the ODE, φ. To guarantee consistency with the cutoff used for the sensitivity analysis, a cutoff of $10\sqrt{\varphi}$ will suffice.*

3. *Partition $V = \begin{bmatrix} V_\ell & V_{q-\ell} \end{bmatrix}$, where q is the total number of parameters.*

4. *Determine a permutation matrix P by constructing a QR factorization with column pivoting for V_ℓ^T. That is, determine P such that*

$$V_\ell^T P = QR,$$

   where Q is an orthogonal matrix and the first ℓ columns of R form an upper triangular matrix with diagonal elements in non-increasing order.

5. *Use P to reorder the parameters θ according to $\tilde{\theta} = P^T \theta$.*

6. *Partition $\tilde{\theta} = \begin{bmatrix} \tilde{\theta}_\ell & \tilde{\theta}_{q-\ell} \end{bmatrix}$, where $\tilde{\theta}_l$ contains the first ℓ elements of $\tilde{\theta}$. Fix $\tilde{\theta}_{q-\ell}$ at the a priori values. Estimate $\tilde{\theta}_\ell$.*

Using this method on the mSIRS model resulted in the subset (k, r, δ), validating the results obtained using the SCM. Generally, the subset obtained after SVD with QR factorization is not guaranteed to be the same as that obtained via the SCM. The subset obtained via the SVD-QR

method may contain correlated parameters so it may be beneficial to use the SCM on the new subset to guarantee the best results.

Additionally, the resulting subset depends upon which parameter is removed once correlations are identified. Each time a parameter is fixed, the solution is biased by that parameter. Since the least sensitive parameter affects the model output the least, it is usually fixed if it is correlated. It may be beneficial to generate a correlation tree, as done in [Olufsen & Ottesen, 2013], to identify all of the possible parameter subsets.

4.5 Optimization

The local sensitivity analysis and subset selection methods previously described identify a set of parameters that are sensitive and linearly uncorrelated. There are numerous optimization techniques available, both local and global, that can be used to find a parameter set that accurately models the data. For example, the DIRECT Method [Kelley, 1999], genetic algorithms [Gen & Cheng, 2000] and Monte Carlo sampling methods [Haario et al., 2006] are global optimization techniques that are effective when the nominal set is not close to the true parameter set. For this study, we compare two local methods: the Nelder-Mead simplex method [Seber & Wild, 2003] and the Levenberg-Marquardt algorithm [Kelley, 1999; Madsen et al., 2004; Marquardt, 1963]. Each of these methods is computationally inexpensive, when compared to the global methods, and produce accurate results, given that the nominal parameter set is close to the true set.

4.5.1 Nelder-Mead

The Nelder-Mead simplex method aims to minimize the least squares cost, shown in (4.6), through a direct search. A simplex, a triangle in ℓ dimensions, is formed using the initial guess for the ℓ parameters that are to be optimized. The algorithm is a pattern search that compares the values of the objective (cost) function f at the vertices of the simplex. The worst vertex, that is where the objective function is the largest, is rejected and replaced with a new vertex [Mathews & Fink, 1998]. This process continues until the difference between the function value at the current and previous iteration is small or the user-specified maximum number of iterations has been reached.

Algorithm 3. *Nelder Mead*

1. *Define the vertices of the simplex S as the columns of the matrix V, where*

$$
V = \begin{array}{ccccccc}
x_1 & x_2 & x_3 & x_4 & \cdots & x_{\ell+1} \\
\begin{bmatrix} \theta_1 \\ \theta_2 \\ \theta_3 \\ \vdots \\ \theta_\ell \end{bmatrix} & \begin{matrix} \theta_1 + \Delta\theta_1 \\ \theta_2 \\ \theta_3 \\ \vdots \\ \theta_\ell \end{matrix} & \begin{matrix} \theta_1 \\ \theta_2 + \Delta\theta_2 \\ \theta_3 \\ \vdots \\ \theta_\ell \end{matrix} & \begin{matrix} \theta_1 \\ \theta_2 \\ \theta_3 + \Delta\theta_3 \\ \vdots \\ \theta_\ell \end{matrix} & \begin{matrix} \cdots \\ \cdots \\ \cdots \\ \ddots \\ \cdots \end{matrix} & \begin{matrix} \theta_1 \\ \theta_2 \\ \theta_3 \\ \vdots \\ \theta_\ell + \Delta\theta_\ell \end{bmatrix}
\end{array}
$$

2. *Evaluate f at the vertices of S and sort the vertices of S such that*

$$
f(x_1) \le f(x_2) \le \cdots \le f(x_{\ell+1}).
$$

3. *Let*

$$
x(\mu) = (1+\mu)\overline{x} - \mu x_{\ell+1}, \quad \text{where} \quad \overline{x} = \frac{1}{\ell}\sum_{i=1}^{\ell} x_i.
$$

4. *Let $f_{count} = \ell + 1$.*
5. *While $f(x_{\ell+1}) - f(x_1) > \tau$*

    (a) **REFLECT**
       Let $x(\mu_r) = 2\overline{x} - x_{\ell+1}$. Then

$$
\begin{aligned}
f_r &= f(x(\mu_r)) = f(2\overline{x} - x_{\ell+1}) \\
&= 2f_m - f(x_{\ell+1})
\end{aligned}
$$

$$
f_{count} = f_{count} + 1.
$$

    (b) *If $f_{count} = k_{max}$, then exit.*
       Otherwise, if $f(x_1) \le f_r < f(x_\ell)$, then let $x_{\ell+1} = x(\mu_r)$. Go to step 5f.
    (c) **EXPAND**
       If $f_{count} = k_{max}$, then exit.
       Otherwise, if $f_r < f(x_1)$, then let $x(\mu_e) = 3\overline{x} - 2x_{\ell+1}$. Then

$$
\begin{aligned}
f_e &= f(x(\mu_e)) = 3f_m - 2f(x_{\ell+1}) \\
&= 2f_r - f_m
\end{aligned}
$$

$$f_{count} = f_{count} + 1.$$

If $f_e < f_r$, then let $x_{\ell+1} = x(\mu_e)$ and go to step 5f. Otherwise, let $x_{\ell+1} = x(\mu_r)$ and go to step 5f.

(d) **OUTSIDE CONTRACTION**

If $f_{count} = k_{max}$, then exit.

Otherwise, if $f(x_l) \le f_r < f(x_{\ell+1})$, then let $x(\mu_{oc}) = 1.5\overline{x} - 0.5x_{\ell+1}$. Then

$$f_{oc} = 1.5f_m - 0.5f(x_{\ell+1})$$

$$f_{count} = f_{count} + 1.$$

If $f_{oc} \le f(x_r)$, then let $x_{\ell+1} = x(\mu_{oc})$ and go to step 3f. Otherwise go to step 3f.

(e) **INSIDE CONTRACTION**

If $f_{count} = k_{max}$, then exit.

Otherwise, if $f_r \ge f(x_{\ell+1})$, then let $x(\mu_{ic}) = 0.5\overline{x} + 0.5x_{\ell+1}$. Then

$$f_{ic} = 0.5f_m + 0.5f(x_{\ell+1})$$

$$f_{count} = f_{count} + 1.$$

If $f_{ic} < f(x_{\ell+1})$, then let $x_{\ell+1} = x(\mu_{ic})$ and go to step 3f. Otherwise go to step 3e.

(f) **SHRINK**

If $f_{count} \ge k_{max} - \ell$, then exit.

Otherwise, for $2 \le i \le \ell + 1$, let $x_i = x_1 - (x_i - x_1)/2$. Compute $f(x_i)$.

(g) Sort the vertices of S so that (2) holds.

The Nelder-Mead method typically only requires one or two function evaluations per iteration, except in the case of a shrink transformation, which rarely occurs. In addition, it is relatively simple to understand and implement. One of the disadvantages of this method is that it may not be able to move beyond a non-optimal parameter value. That is, it can take a large number of iterations with negligible improvements in the cost, despite being no where near the minimum. Thus, it is not guaranteed to converge to an optimal value.

The parameters for the mSIRS model were estimated using MATLAB's built-in optimization function fminsearch, a multidimensional unconstrained optimizer that uses the Nelder-Mead direct search method. The optimal parameter values for the mSIRS model are shown in Table 4.1 on page 46.

4.5.2 Levenberg-Marquardt

The Levenberg-Marquardt method uses a combination of the gradient descent method and the Gauss-Newton method [Bjorcl, 1996]. Its objective is to find a perturbation h to the parameters θ that will reduce J. The gradient descent method updates the parameters in the direction of steepest descent, while the Gauss-Newton Method assumes that the least squares function is locally quadratic and then finds the minimum of the quadratic. To ensure that the optimal parameter value is local, compared to the nominal, bounds can be given to the optimizer.

For gradient descent method, the parameter update h that moves the parameters in the direction of steepest descent is given by

$$h_{gd} = \alpha \chi^T (Y - y), \tag{4.19}$$

where χ is the sensitivity matrix defined in (4.8) and $\alpha > 0$ determines the length of the step in the steepest-descent direction. The value w_i is a measure of the error in measurement $Y(t_i)$.

For the Gauss-Newton method, the parameter update h is given by solving

$$\left[\chi^T \chi \right] h_{gn} = \chi^T (Y - y). \tag{4.20}$$

The Levenberg-Marquardt method adaptively varies the parameter updates between the gradient descent update and the Gauss-Newton update. Mathematically, its found by solving

$$\left[\chi^T \chi + \lambda I \right] h_{lm} = \chi^T (Y - y), \tag{4.21}$$

where small values of λ result in a Gauss-Newton update and large values result in a gradient descent update. Initially, λ is set to be large, resulting in a gradient descent update. If a new iteration is a worse approximation, then λ is increased. As the solution improves, the Levenberg-Marquardt method approaches the Gauss-Newton method, and the solution typically moves to the local minimum.

Given an initial λ_0 and initial parameter set θ_0, the Levenberg-Marquardt method is executed by the functions `levmar` and `trtestlm`, summarized in Algorithm 4.

Algorithm 4. $\hat{\theta} = \text{levmar}(\theta, f, tol, k_{max})$

   1. For $k = 1, \ldots, k_{max}$

      (a) Compute

$$y = g(t, x, \theta), \quad R = Y - y, \quad J(\theta) = R^T R, \quad \chi = \frac{\partial y}{\partial \theta}, \quad \nabla(\theta) = \chi^T R \tag{4.22}$$

      (b) Let $\lambda = \|\nabla(\theta)\|_2$.

(c) While $\lambda > tol$

    i. Let $h = (\chi^T \chi + \lambda I)^{-1} \nabla(\theta)$ and $\theta_t = \theta + h$.

    ii. Solve $[\theta, \lambda] = \texttt{trtestlm}(\theta, \theta_t, J(\theta), \chi, \nabla(\theta), \lambda, \lambda_0)$.

    iii. Compute $y, R, J(\theta), \chi$, and $\nabla(\theta)$ as defined in (4.22).

2. Let $\hat{\theta} = \theta$.

  Given the trust region parameters $0 < \omega_{down} < 1 < \omega_{up}$ and $\mu_0 \leq \mu_{low} < \mu_{high}$, the $\texttt{trtestlm}$ algorithm is summarized next.

Algorithm 5. $[\theta, \lambda] = \texttt{trtestlm}(\theta, \theta_t, J(\theta), \chi, \nabla(\theta), \lambda, \lambda_0)$.

1. Let $z = \theta$.

2. While $z = \theta$

    (a) Compute $J(\theta_t)$ and let

$$s = \theta_t - \theta, \qquad ared = J(\theta) - J(\theta_t), \qquad pred = -\frac{1}{2}(\nabla(\theta)s).$$

    Then define $\Gamma = ared/pred$.

    i. If $\Gamma < \mu_0$, then let

$$\lambda = \max(\lambda \omega_{up}, \lambda_0), \qquad h = (\chi^T \chi + \lambda I)^{-1} \nabla(\theta_t), \qquad and \qquad \theta_t = \theta + h.$$

    Otherwise, if $\Gamma < \mu_{low}$, then let $z = \theta_t$ and $\lambda = \max(\lambda \omega_{up}, \lambda_0)$.
    If neither of these conditions are satisfied, then let $z = \theta_t$ and if $\Gamma > \mu_{hi}$, then let
    $\lambda = \omega_{down} \lambda$. If $\lambda < \lambda_0$, then let $\lambda = 0$.

3. Let $\theta = z$.

  Due to the gradient descent portion of the Levenberg-Marquardt method, the $\nabla(\theta)$ will decrease at every iteration, increasing the likelihood that R will be minimized. Additionally, the algorithm allows for bounds to be on imposed on the parameter values, thus preventing the parameters from becoming unrealistic. However, if the nominal parameter value is far from the true parameter, then the algorithm may not converge. If convergence is achieved, the process will be slow and in some cases, it will converge to the bounds preset by the user. If this happens, it is likely that the optimal parameter set will have large parameter confidence intervals (discussed in section 4.6.1. Further details on the Levenberg-Marquardt method, as well as the trust region parameters, can be found in [Kelley, 1999].

Table 4.1 *Optimal parameters for the mSIRS model.* Sensitivity and correlation analysis identified γ as sensitive, but correlated. Thus, it was fixed at its nominal value. The remaining three parameters k, δ, and r were estimated using the Nelder-Mead and Levenberg-Marquardt methods using different variances, $\sigma^2 = 25$ and $\sigma^2 = 200$.

Parameter	True	$\sigma^2 = 25$		$\sigma^2 = 200$	
		$\hat{\theta}_{NM}$	$\hat{\theta}_{LM}$	$\hat{\theta}_{NM}$	$\hat{\theta}_{LM}$
k	0.10	0.108	0.108	0.117	0.117
δ	0.15	0.156	0.156	0.173	0.173
r	0.60	0.611	0.611	0.682	0.682

4.5.2.1 Optimization Results

To the accuracy of the mSIRS model, the optimal parameters produced using the Nelder-Mead method and the Levenberg-Marquardt methods are the same for each value of σ^2, as shown in Table 4.1. This may be due to the fact that the data was created using the true parameter set. In the typical inverse problem, experimental data is given and the inverse problem is solved to find the parameter values that characterize the system. The Nelder-Mead optimization took 1.1270 seconds to find the optimal values, while the optimization using Levenberg-Marquardt took 1.1507 seconds using `MATLAB` version R2016a. The optimized model results are shown in Figure 4.5 on page 50 for $\sigma = 25$ and $\sigma = 200$.

The residuals as a function of the model output, shown in the middle panel of Figure 4.4, show that the model is able to predict the data well for both $\sigma = 25$ and $\sigma = 200$. Had there been a clear relationship between the model output and the residuals, then it could be concluded that there are underlying factors of the data that the model is failing to capture. The right panels of Figure 4.4 show the effect of generating the data directly from the model. Due to how the synthetic data was generated, the model is almost completely aligned with the data. Generally, this will not be the case and the regression line, shown in blue, will differ from the line $y = x$, shown in red.

4.6 Uncertainty Quantification

Uncertainty quantification involves determining parameter output uncertainties from uncertainties in the model formulation and experimental measurements. There are two approaches to accomplish this, namely *frequentist* methods and *Bayesian* methods. In the frequentist framework, parameters are described by an estimate of the true value. It is assumed that the errors of the model are normally distributed, though this is usually not the case. Thus, the frequentist approach may not be as useful
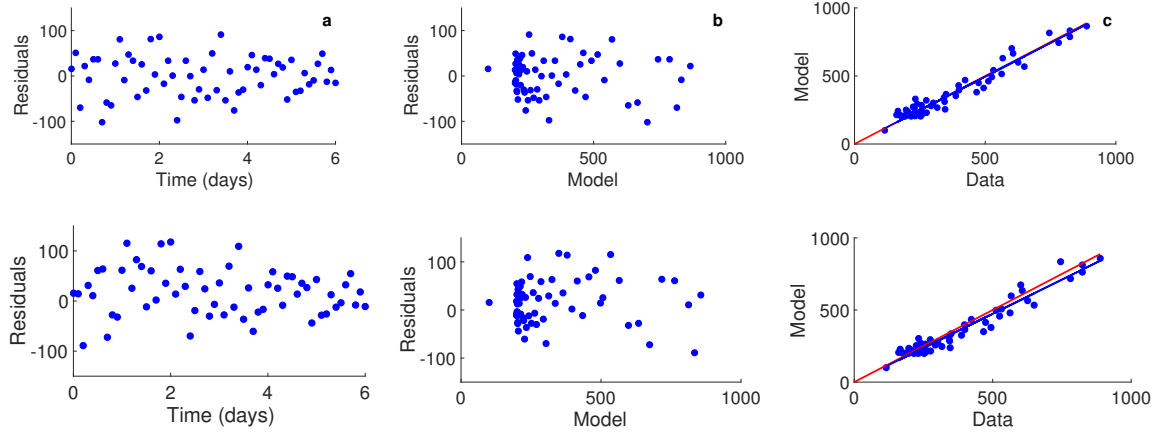
Figure 4.4 *Residuals plots for the mSIRS model.* Residuals are computed using the optimal values shown in Table 4.1 for $\sigma = 25$ (top panels) and $\sigma = 200$ (bottom panels). The line $y = x$ is shown by the red line and the regression line $y_{\text{model}} = m\, y_{\text{data}}$ is shown by the blue line.

in the estimation of the uncertainty in the model output [Smith, 2014]. More precise, yet more computationally expensive, results can be achieved through Bayesian sampling methods, such as Delayed Metropolis Adaptive Rejection (DRAM) [Haario et al., 2006]. These methods are more adaptive in how the parameter distributions can vary across different data sets and are able to identify pairwise parameter correlations that identifiability analysis fails to identify.

4.6.1 Frequentist Methods

The *parameter confidence interval* provides information on the extent of uncertainty involved in estimating the true, but typically unknown, parameter set [Banks & Tran, 2009]. The uncertainty in the predicted parameter values can be propagated through the model to obtain uncertainty measurements in the form of prediction and confidence intervals. The *prediction interval* provides information about the distribution of the model output values, while the *confidence interval* is used to measure the precision of the model in predicting the mean response.

Parameter Confidence Intervals

To compute the parameter confidence interval, recall that the covariance matrix is defined as $C = (\chi^T \chi)^{-1}$, where χ is defined in (4.8). From (4.5) it is assumed that ϵ_i are i.i.d. $\mathcal{N}(0, \sigma^2)$. Then $\hat{\theta} \sim \mathcal{N}_q(\bar{\theta}, \sigma^2(\chi^T \chi)^{-1})$, where $\bar{\theta}$ is the unknown true parameter set and $\hat{\theta}$ is the (optimal) estimator

Table 4.2 *Parameter confidence intervals for the mSIRS model.* Intervals are shown using varying levels of σ^2. Sensitivity and correlation analysis identified γ as sensitive, but correlated. Parameter confidence intervals are shown for the remaining 3 parameters.

Parameter	True	$\sigma^2 = 25$ $\hat{\theta} \pm \Delta\theta$	$\sigma^2 = 100$ $\hat{\theta} \pm \Delta\theta$
k	0.10	0.108 ± 0.0147	0.117 ± 0.0340
δ	0.15	0.156 ± 0.0321	0.173 ± 0.0697
r	0.60	0.611 ± 0.0470	0.682 ± 0.1116

of $\bar{\theta}$. The confidence interval for the jth element of $\hat{\theta}$ is given by

$$\hat{\theta} \pm t_{N-\ell}^{\alpha/2} s \sqrt{C_{jj}} = \hat{\theta} \pm \Delta\theta,$$

where N is the total number of data points, ℓ is the total number of parameters estimated, $t_{N-q}^{\alpha/2}$ is the t-value for the $1-\alpha/2$ quartile with $N-\ell$ degrees of freedom, and

$$s^2 = \frac{1}{N-q} J(\hat{\theta})$$

is an estimator of the variance σ^2. The parameter confidence intervals for the optimal parameter values $\hat{\theta}$ are given in Table 4.2. As the variance in the data increases, the widths of the parameter confidence intervals also increases. Thus, the closer the optimal parameters are to the true parameter values, the thinner the parameter confidence intervals will be.

Prediction Interval

To obtain a prediction interval for y at $t = t_1, t_2, \ldots, t_N$, let

$$y_i = g(t_i, x(t_i), \bar{\theta}) + \epsilon_i, \quad \epsilon_i \sim \mathcal{N}(0, \sigma^2).$$

Then an obvious estimator of y_i is $\hat{y}_i = g(t_i, x(t_i), \hat{\theta})$. For large N, $\hat{\theta}$ is close to the true value $\bar{\theta}$, so we can use the Taylor series expansion

$$g(t_i, x(t_i), \bar{\theta}) \approx g(t_i, x(t_i), \hat{\theta}) + g_i^T(\hat{\theta} - \bar{\theta}),$$

where

$$g_i^T = \left(\frac{\partial g(t_i, x(t_i), \hat{\theta})}{\partial \hat{\theta}_1}, \quad \frac{\partial g(t_i, x(t_i), \hat{\theta})}{\partial \hat{\theta}_2}, \quad \ldots, \quad \frac{\partial g(t_i, x(t_i), \hat{\theta})}{\partial \hat{\theta}_q} \right).$$

Thus,

$$y_i - \hat{y}_i \approx y_i - \left(g(t_i, x(t_i), \bar{\theta}) - g_i^T(\hat{\theta} - \bar{\theta})\right) = \epsilon_i + g_i^T(\hat{\theta} - \bar{\theta}).$$

This implies that

$$\mathbb{E}[y_i - \hat{y}_i] \approx \mathbb{E}[\epsilon_i] + g_i^T \mathbb{E}(\hat{\theta} - \bar{\theta}) \approx 0.$$

Moreover,

$$\begin{aligned}
\text{var}[y_i - \hat{y}_i] &\approx \text{var}[\epsilon_i] + \text{var}(g_i^T(\hat{\theta} - \bar{\theta})) \\
&\approx \sigma^2 + \sigma^2 g_i^T (\chi^T \chi)^{-1} g_i \\
&= \sigma^2(1 + v_0),
\end{aligned}$$

where $v_0 = g_i^T(\chi^T\chi)^{-1}g_i$. Thus, $y_i - \hat{y}_i$ is asymptotically $\mathcal{N}(0, \sigma^2(1 + v_0))$. s^2 is independent of y_i and is asymptotically independent of $\hat{\theta}$, so that s^2 is asymptotically independent of $y_i - \hat{y}_i$ by the Central Limit Theorem. Hence, asymptotically

$$\frac{y_i - \hat{y}_i}{s\sqrt{1 + v_0}} \sim t_{N-\ell}$$

has a t-distribution with $N - \ell$ degrees of freedom. So the prediction interval for y at $t = t_i$ is given by

$$\hat{y}_i \pm t_{N-q}^{\alpha/2} s(1 + g_i^T(\chi^T\chi)^{-1}g_i)^{1/2}. \tag{4.23}$$

Confidence Interval

To obtain a confidence interval for the mean response, note that

$$\hat{y}_i = g(t_i, x(t_i), \hat{\theta})$$

is an estimation of the mean response. Then

$$\mathbb{E}[\hat{y}_i] = \bar{y}_i,$$

where $\bar{y}_i$ is the mean response, and

$$\text{var}[\hat{y}_i] = \sigma^2 g_i^T (\chi^T\chi)^{-1} g_i.$$

49

(a) $\sigma^2 = 25$ **(b)** $\sigma^2 = 100$
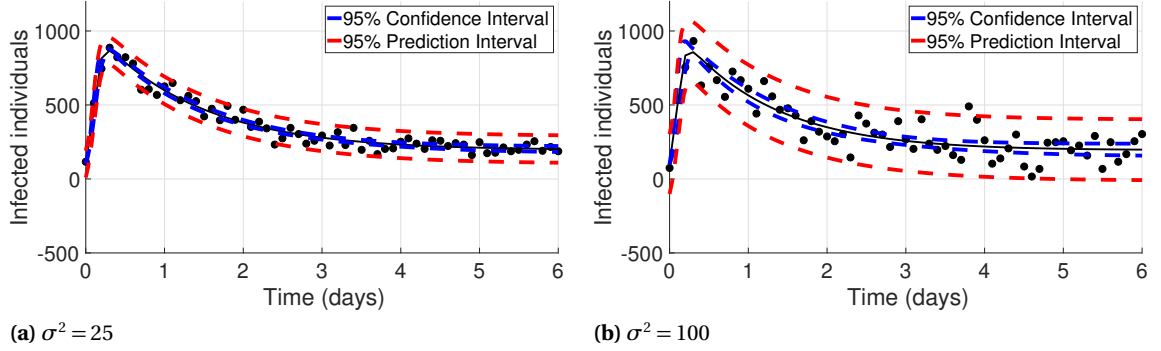
Figure 4.5 *Model predictions with frequentist confidence and prediction intervals.* Frequentist prediction (red dashed line) and confidence intervals (blue dashed line) for the mSIRS model output $y = I$ (black line) with varying levels of σ^2.

This implies that

$$\frac{\hat{y}_i - \bar{y}_i}{s\sqrt{v_0}} \sim t_{N-\ell}$$

has a t-distribution with $N - \ell$ degrees of freedom. So the confidence interval for y at $t = t_i$ is given by

$$\hat{y}_i \pm t_{N-q}^{\alpha/2} s (g_i^T (\chi^T \chi)^{-1} g_i)^{1/2}. \tag{4.24}$$

For further details of the derivation, please see [Seber & Wild, 2003; Smith, 2014]. The prediction and confidence intervals for the mSIRS model are shown in Figure 4.5. Similar to the parameter confidence intervals, increasing the amount of variance from the model output attained with the true parameter values results in larger confidence and prediction intervals.

4.6.2 Bayesian Methods

Using synthetic data ensures that the assumption of normally distributed errors holds. However, when experimental data is used, this assumption does not always hold. Bayesian methods allow the parameter distributions to vary according to the given data set. The Bayesian credible and prediction intervals are calculated using a sampling method. The prerequisite condition to using a sampling method is to have defined uncertainty distributions for the model inputs (parameters). The parameter chains built from Delayed Metropolis Adaptive Rejection (DRAM) provide these distributions. Frequentist methodology is fundamentally rooted in quantifying uncertainty in terms of repeating the data generating procedure. However, in a Bayesian context, inference is conditioned on the single data set that is observed; this allows for uncertainty about parameters to be expressed

with probability distributions. Thus in the Bayesian framework, $\hat{\theta}$ refers to a vector of random variables and rather than searching for a point estimate, it is desired to estimate the distribution associated with the random variables. Given the observations $Y = [Y_1, Y_2, \ldots, Y_N]$, Bayes formula

$$\pi(\hat{\theta}|Y) = \frac{\pi(Y|\hat{\theta})\pi(\hat{\theta})}{\pi(Y)} \tag{4.25}$$

is used to describe the relationship between the prior parameter density $\pi(\hat{\theta})$, the posterior density $\pi(\hat{\theta}|Y)$, and the likelihoood $\pi(Y|\hat{\theta})$ of observing the data Y for the model given $\hat{\theta}$. $\pi(Y)$ is the marginal density of the data but in practice functions as a normalization factor and can be determined by $\int \pi(Y|\hat{\theta})\pi(\hat{\theta})\mathrm{d}\hat{\theta}$.

Assuming the statistical hypothesis in equation (4.5), it follows that

$$\pi(Y|\hat{\theta}) = \frac{e^{-J(\hat{\theta})/2\sigma^2}}{(2\pi\sigma^2)^{d/2}},$$

where $J(\hat{\theta})$ is typically defined as the least squares error, however it can be replaced with any cost function. With the likelihood function given, it is possible to estimate the posterior density $\pi(\hat{\theta}|Y)$. While this route is theoretically possible for some low-dimensional problems, the evaluation of high-dimensional integrals is a difficult and expensive task and is currently an active research area (see sparse grids [Heiss & Winschel, 2008] and quasi-Monte Carlo methods [Dick et al., 2013]).

Delayed Rejection Adaptive Metropolis (DRAM)

A practical alternative is to randomly sample directly from the density $\pi(Y|\hat{\theta})$ through the use of the DRAM, which combines two methods for improving efficiency of Metropolis-Hastings type Markov chain Monte Carlo (MCMC) algorithms: Delayed Rejection and Adaptive Metropolis. Metropolis algorithms are acceptance-rejection algorithms that accept new parameter samples only if the likelihood of the new candidate is higher than the current sample. Delayed rejection allows the algorithm to try additional proposals per step if the initially proposed step is not accepted. This increases the acceptance rate and thereby mixing of the chain, which results in better estimates of the posterior densities. Adaptive metropolis allows the metropolis algorithm to update the covariance matrix based on the history of the chain. This helps the algorithm make better proposals, and move to the correct posterior distribution faster; reducing what is called the "burn-in" period.

Note that updating the proposal function using history of the chain breaks the Markov property, and other properties need to be established for guaranteed sampling from the posterior distribution [Haario et al., 2006; Smith, 2014]. Results from Bayesian sampling methods such as DRAM are able

to identify pairwise relationships among the parameter distributions and capture the entirety of the nonlinear interactions between parameters by representing them as a joint density of random variables.

The plot shown in Figure 4.6c shows an exponential correlation between γ and k, as well as a linear correlation between δ and r for the mSIRS model. While correlation analysis is far less computationally expensive than DRAM, it only provides a first-order linearization of parameter interactions. Thus correlation analysis may fail to capture the nuance of parameter interactions in models with complicated nonlinear parameterizations, as well as less obvious linear correlations.
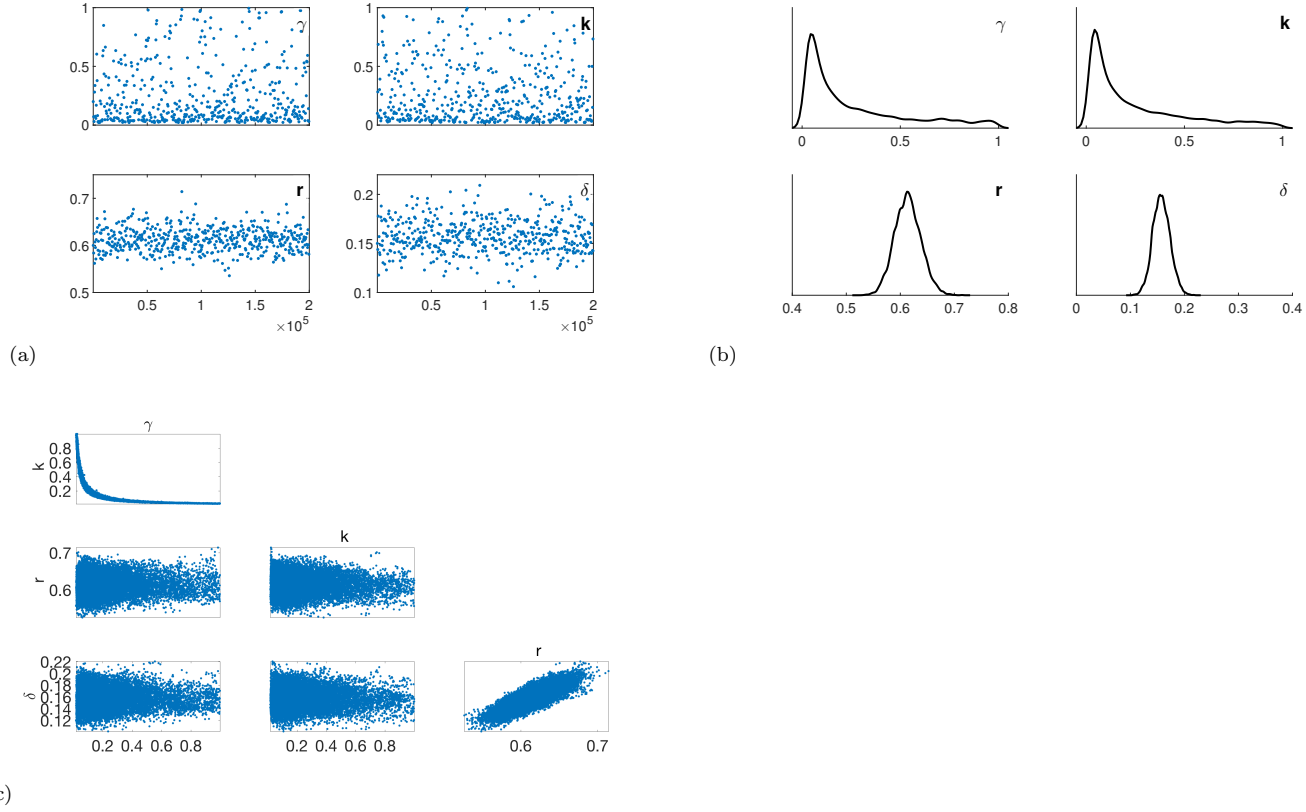
Figure 1: *DRAM results for the mSIRS model with* $\theta = (\delta, \gamma, k, r)$. (a)Parameter chains, (b) parameter distributions, and (c) correlations for $\sigma^2 = 25$. While r and δ have converged to their optimal values, the correlated parameters γ and k are unable to due to the exponential relationship between k and γ. Simulations were ran with 200,000 samples with a burn-in period of 40,000.

The differences between the parameter chains with and without the least sensitive parameter γ, shown in Figures 4.6a and 4.7a respectively, show that removing γ results in better convergence of the chains towards the optimal parameter values. However, DRAM continued to identify a correlation between r and δ, as shown in Figure 4.7b. The structural correlation method failed to recognize this correlation, leading to doubt in the accuracy of the optimal parameter set. Revisiting the correlation matrix shown in (4.18), the correlation coefficient between r and δ is 0.82. Thus, had the cutoff been set between 0.80 and 1, rather than between 0.90 and 1, r would have been omitted from the set of parameters to be estimated.

Comparing the parameter probability distributions shown in Figure 4.6 and 4.7 shows the effect of including correlated parameters in the set to be estimate. Not accounting for the exponential correlation between γ and k resulted in skewed distributions for each of them. The long tails in the distributions for γ and k may be evidence of the correlation between these parameters. Based on the structure of the model, a large value of γ should require a lower value for k and vice versa. Once γ is removed, the parameter samples were able to stay around the mean values of 0.1, 0.6, and 0.15 for k, r, and δ, respectively, as expected based on the parameter confidence intervals shown in Table 4.2. It is interesting to note that the possible correlation between r and δ did not affect the resulting parameter distributions. This solidifies the argument for the cutoff for the structured correlation method to be between 0.90 and 1. Removing r may have resulted in optimal parameter values that did not fully capture the characteristics of the system.

Though DRAM may be more effective in identifying nonlinear pairwise correlations, running DRAM typically requires performing some form of frequentist parameter estimation to set a good starting point of the sampling to prevent the algorithm from getting stuck in an undesirable local minimum of the predefined cost function $J(\theta)$. This is to say that tools such as correlation analysis might be a better option over DRAM in the early stages of model calibration. The real benefit and power of using Bayesian MCMC algorithms like DRAM comes from the ease in propagating the parameter densities through the model the calculate Bayesian credible and prediction intervals to quantify the uncertainty of our model predictions. The prediction and credible intervals for the mSIRS model produced by DRAM are shown in Figure 4.8. As expected, the intervals are almost identical to those obtained using frequentist methods, shown in Figure 4.5 on page 50. This may be due to the fact that the parameters were optimized from the nominal set used to generate the data. In general, this will not be the case.

More about the nuances of these sampling methods can be found in [Haario et al., 2006; Smith, 2014]. Furthermore, the MCMC `MATLAB` toolbox by Haario et al. [2006] contains code that performs Bayesian uncertainty propagation.
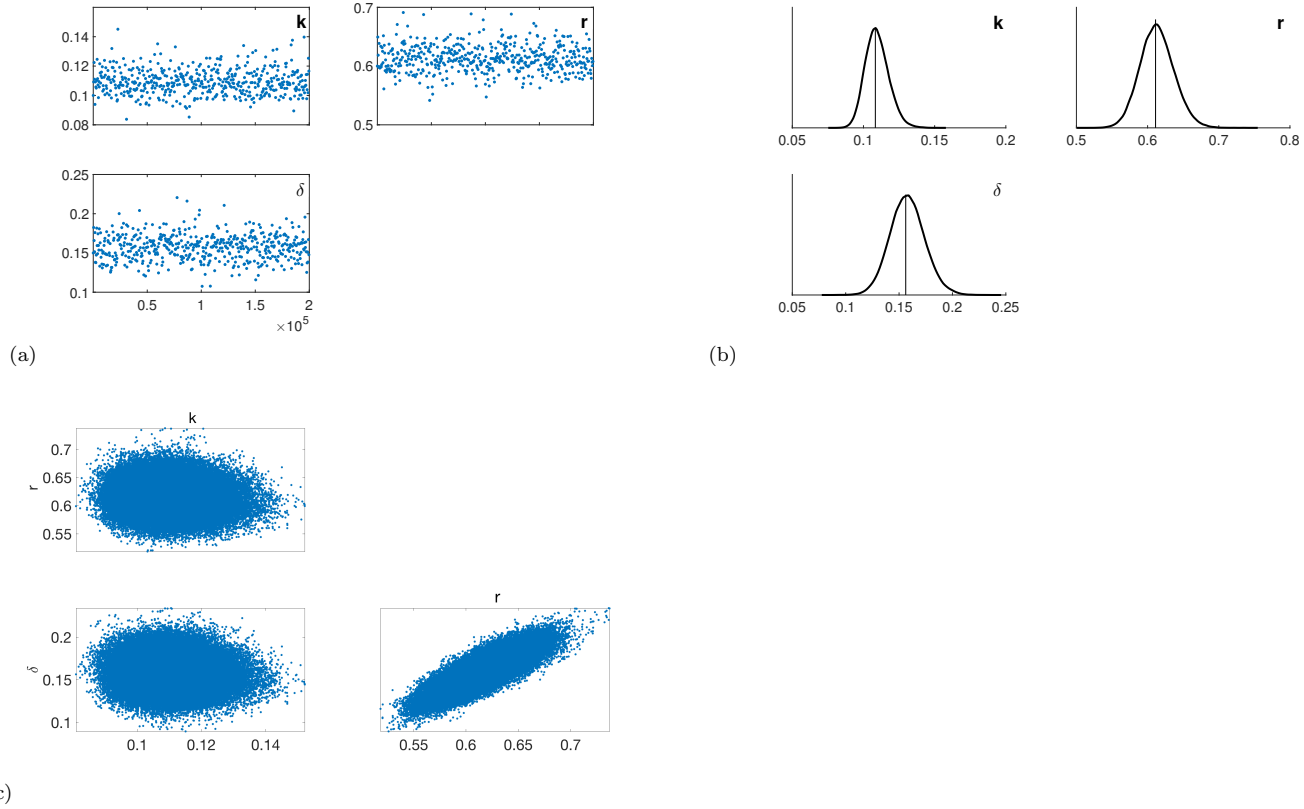
Figure 1: *DRAM results for the mSIRS model with $\theta = (\delta, k, r)$.* (a) Parameter chains, (b) parameter distributions, and (c) correlations, and subsequent distributions when $\sigma^2 = 25$ after excluding the least sensitive and correlated parameter γ. After removing γ, all three parameters were able to converge to their optimal values. Simulations were ran with 200,000 samples with a burn-in period of 40,000.
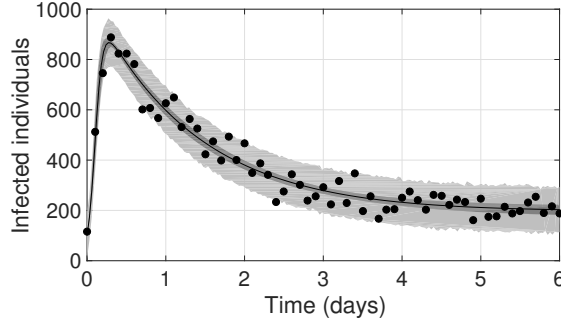
Figure 4.8 *Credible and prediction intervals for the mSIRS model using DRAM.* Credible intervals are shown in light gray and prediction intervals are in dark gray.

4.7 Discussion

The concepts of sensitivity and identifiability analysis have been introduced. Though global methods exist [Cacuci, 2003; Haario et al., 2006], the methods for quantifying the sensitivity of the model to changes in the parameter values were focused on the the local sensitivities. Two methods for practical identifiability analysis were discussed, namely the structural correlation method and SVD followed by QR factorization. These methods were tested and analyzed using the mSIRS model, with comparable results. The structural correlation method provides more reliable results than the SVD followed by QR factorization method. However, the lack of a concrete cutoff value for the correlation coefficient can result in linear correlations being included in the parameter estimation.

Parameter estimation techniques were also discussed, in particular, the local Levenberg-Marquart and Nelder-Mead algorithms. The Nelder-Mead algorithm tends to be more computationally expensive than the Levenberg-Marquardt algorithm, as it finds an absolute minimum. However, since it does not depend on numerical or analytic gradients, it does return the sensitivity matrix, covariance matrix, or mean squared error, thus making Levenberg-Marquardt more attractive. Levenberg-Marquardt finds a local minimum which can produce parameters that accurately describe the system if the nominal parameters are close to the true values. However, if they are not, the optimizer may stall and produce model output that do not accurately predict the behavior of the system. Uncertainty quantification was used to quantify the amount of uncertainty

in estimating parameters for the model. Both frequentist and Bayesian methods were discussed. The Bayesian methods also provided a global practical identifiability analysis, unlike the methods previously discussed. DRAM was able to identify nonlinear pairwise correlations that the linear methods could not.

CHAPTER

5

MODELING THE INFLAMMATORY RESPONSE

Generalized mathematical models of the acute inflammatory response have been used to understand how to regulate the response and to maintain homeostasis. However, a large number of those models address the response in mice [Chow et al., 2005; Copeland et al., 2005], as well as in swine [Nieman et al., 2012], and cannot be effectively used to model the response in humans. Simple models of the response in humans [Day et al., 2006; Kumar et al., 2004; Reynolds et al., 2006] have been developed, allowing for rigorous mathematical analysis and simplified biological assumptions. However, very few of these models include the analysis of experimental data and have been tailored specifically for individual patients.

This chapter presents the development of the mathematical model of the acute inflammatory response to an endotoxin challenge. The components of the model and their corresponding equations are presented in Section 5.1. The parameterization is explained in Section 5.2, including

the parameterization of Hill functions and details on parameter scaling, creating a patient-specific parameter set.

5.1   Mathematical Model

The mathematical model developed here incorporates several key components of the acute inflammatory response, including the endotoxin P, resting and activated monocytes M_R and M_A and circulating inflammatory mediators (TNF-α, IL-6, IL-8, and IL-10). The model is formulated as a system of seven ordinary differential equations describing the dynamics of the endotoxin, blood monocytes, and circulating mediators and 43 parameters quantifying their interactions, illustrated in Figure 5.1.

Endotoxin

Upon endotoxin injection, the pathogenic ligand is bound to the toll-like receptor 4 (TLR4) [24, 25] on resting circulating monocytes that will mediate its clearance from the body. This process is modeled using exponential decay with an initial value of $P(0) = 2$ ng/kg with an equation of the form

$$\frac{dP}{dt} = -k_P P, \tag{5.1}$$

where k_P is the decay rate. This is similar to the equation used in the model by [Chow et al., 2005; Copeland et al., 2005; Reynolds et al., 2006]. An alternative model of the pathogen is given by

$$\frac{dP}{dt} = -k_P P M_A,$$

i.e. the decay of the pathogen depends explicitly on the number of resting monocytes present, which was used to model the interaction between the monocytes and pathogen in the model by Reynolds et al. [2006]. However, the initial decay of the P is rapid in comparison to the transition between the resting and activated phases. Thus, we chose to use an exponential decay function for P.

Monocytes

The resting monocytes are formed in the bone marrow, and are released into the circulation as a means of the ongoing immune activation. The circulating monocytes are activated by endotoxin via TLR4 signaling. The circulating activated monocytes trigger the production of pro-inflammatory mediators such as TNF-α and also leads to the production of IL-6, IL-8, as well as the anti-inflammatory mediator IL-10. Moreover, via autocrine loops TNF-α amplifies the inflammatory response by further activating monocytes to release the IL-6 and IL-8. TNF-α also stimulates the activated monocytes to produce IL-10, which exert negative feedback on the system, due to its anti-inflammatory properties.

The interactions between the components acting on the resting monocytes are described by the equation

$$\frac{dM_R}{dt} = -H_M^U(P)\Big(k_M + k_{M\text{TNF}}H_M^U(\text{TNF})\Big)H_M^D(\text{IL10})M_R + k_{MR}M_R\Big(1 - \frac{M_R}{M_\infty}\Big) \tag{5.2}$$

where k_M is the rate of decrease in the number of resting monocytes as a result of the pathogen, in the absence of TNF-α. Once TNF-α is produced, the number of resting monocytes decreases further as a result of both the pathogen and TNF-α. The up- and down-regulation of the monocytes are represented by increasing and decreasing Hill functions,

$$H_M^U(X) = \frac{X^h}{\eta_{YX}^h + X^h} \quad \text{and} \quad H_M^D(X) = \frac{\eta_{YX}^h}{\eta_{YX}^h + X^h}, \tag{5.3}$$

respectively; as shown in Figure 5.2 each Hill function ranges between zero and one. Unlike proportional or inversely proportional relations, modeling these interactions with equations of this form allow for the rate of increase/decrease to vary, depending on the magnitude of the regulatory component. For small values of X, $H_Y^U(X)$ is approaching zero, while $H_Y^D(X)$ is approaching one. This restricts the effect of the regulatory component to the portion where the magnitude of X is changing significantly.

The resting monocytes are up-regulated by TNF-α and down-regulated by IL-10. The positive feedback of the resting monocytes on themselves is accounted for by the additional M_R in the first term of the equation. The final term in (5.2) is the natural recruitment and decay of the resting

monocytes modeled with a logistic growth term. The k's are rate constants describing activation or elimination rates and M_∞ is the maximum number of monocytes present. In the absence of a pathogen, as the number of resting monocytes approaches the carrying capacity M_∞, the rate of increase will decrease, forcing the number of resting monocytes to M_∞. The logistic growth imposes a limit on the total number of monocytes circulating.

The activated monocytes are represented by

$$\frac{dM_A}{dt} = H_M^U(P)\Big(k_M + k_{M\text{TNF}}H_M^U(\text{TNF})\Big)H_M^D(\text{IL10})M_R - k_{MA}M_A \tag{5.4}$$

which is almost identical to equation (5.2), however the first term is positive and the last term is the natural decay of the activated monocytes. The activated monocytes come from the resting phase so its equation does not include a natural growth term. The change from negative to positive in the first term represents the monocytes going from the resting phase to the activated phase.

Mediators

The rate of change of the mediators is described as a combination of the number of active monocytes present and the influence from the pro- and anti-inflammatory mediators. For the pro-inflammatory mediators, these interactions are described by the equations

$$\frac{d\text{TNF}}{dt} = k_{\text{TNF}M}H_{\text{TNF}}^D(\text{IL6})H_{\text{TNF}}^D(\text{IL10})M_A - k_{\text{TNF}}(\text{TNF}-q_{\text{TNF}}), \tag{5.5}$$

$$\frac{d\text{IL6}}{dt} = \Big(k_{6M} + k_{6\text{TNF}}H_{\text{IL6}}^U(\text{TNF})\Big)H_{\text{IL6}}^D(\text{IL6})H_{\text{IL6}}^D(\text{IL10})M_A - k_6(\text{IL6}-q_{\text{IL6}}), \tag{5.6}$$

$$\frac{d\text{IL8}}{dt} = \Big(k_{8M} + k_{8\text{TNF}}H_{\text{IL8}}^U(\text{TNF})\Big)H_{\text{IL8}}^D(\text{IL10})M_A - k_8(\text{IL8}-q_{\text{IL8}}), \tag{5.7}$$

where the Hill functions model the up- and down-regulation and the k's are the rate constants. Down-regulation by the anti-inflammatory cytokine IL-10 is modeled by a decreasing Hill function $H_Y^D(\text{IL10})$. Though categorized as a pro-inflammatory mediator, IL-6 exhibits an anti-inflammatory effect on TNF-α, as well as on itself [Schulte et al., 2013; Starkie et al., 2003]. The down-regulation by both IL-6 and IL-10 is modeled by a product of decreasing Hill functions, namely $H_Y^D(IL6)H_Y^D(IL10)$. The net growth of each mediator, that is, the behavior of the mediator without the presence of an endotoxin, is represented by the last term $-k(X-q)$, where the source term q represents the

amount of mediator present in the absence of an endotoxin.

The anti-inflammatory mediator IL-10 is modeled by the equation

$$\frac{d\,\text{IL}10}{d\,t} = \Big(k_{10M} + k_{106} H_{\text{IL}10}^{U}(\text{IL}6)\Big)M_A - k_{10}(\text{IL}10 - q_{\text{IL}10}). \tag{5.8}$$

Note that IL-10 is not down-regulated by any other mediator. Thus, (5.8) only consists of the initial production by the activated monocytes and the up-regulation by IL-6. As before, $-k_{10}(\text{IL}10 - q_{10})$ represents the natural source and decay of IL-10.

5.2 Parameterization

To parameterize the model, we 1) consider the behavior of the monocytes and inflammatory mediators in the absence of a pathogen. Next we 2) consider the three-state subsystem comprised of the monocytes and the pathogen, and then 3) combine the two subsystems. Once each of the model components has been included, parameter scaling is used to ensure that the model output attains the proper magnitude.

5.2.1 The Monocyte-Mediator Subsystem

In the absence of a pathogen, the net growth of the monocytes can be modeled as

$$\frac{d\,M_R}{d\,t} = k_{MR} M_R\Big(1 - \frac{M_R}{M_\infty}\Big), \qquad M_R(0) = 28200,$$
$$\frac{d\,M_A}{d\,t} = -k_{MA} M_A, \qquad\qquad M_A(0) = 0,$$

where the initial condition for M_R and carrying capacity, M_∞, are obtained from literature [Deventer et al., 1990]. Since we are not modeling an intermediate step between the resting and activated phases, the growth of the activated monocytes is completely dependent upon the number of resting monocytes. Without activation by the pathogen, the activated monocytes will remain at zero due to the exponential decay.

The net growth of the inflammatory mediators are determined by equations of the form

$$\frac{dX}{dt} = -k(X - q), \quad \text{where} \quad X(0) = q.$$

The intrinsic level of each mediator, q, is extracted from the experimental data. That is, the value of each mediator prior to the introduction of the pathogen. From the equation, it is clear that $X = q$ is an equilibrium point so if the mediators start at q, then they will remain at q.

5.2.2 The Monocyte-Pathogen Subsystem

When the pathogen is introduced at $t = 0$, the monocytes begin their transition from resting to activated. This is represented by

$$\frac{dM_R}{dt} = -k_M H_M^U(P)M_R + k_{MR}M_R\left(1 - \frac{M_R}{M_\infty}\right) \quad \text{and} \quad \frac{dM_A}{dt} = k_M H_M^U(P)M_R - k_{MA}M_A.$$

The value for k_M is chosen such that the number of activated monocytes increases relative to the amount of pathogen present. The parameterization of the Hill function $H_M^U(P)$ and all of the Hill functions to follow are explained in Section 5.2.4.

5.2.3 The Monocyte-Pathogen-Mediator System

The activation of the monocytes triggers the production of TNF-α. This is modeled by

$$\frac{d\text{TNF}}{dt} = k_{\text{TNFM}}M_A - k_{\text{TNF}}(\text{TNF} - q_{\text{TNF}}).$$

The values for k_{TNFM} and k_{TNF} are adjusted to control the rate of growth and decay in the presence of the monocytes. This production encourages the activation of the monocytes, modeled by

$$\begin{aligned}
\frac{dM_R}{dt} &= -H_M^U(P)\left(k_M + k_{\text{MTNF}}H_M^U(\text{TNF})\right)M_R + k_{MR}M_R\left(1 - \frac{M_R}{M_\infty}\right), \\
\frac{dM_A}{dt} &= H_M^U(P)\left(k_M + k_{\text{MTNF}}H_M^U(\text{TNF})\right)M_R - k_{MA}M_A.
\end{aligned}$$

The value for $k_{M\text{TNF}}$ is chosen such that the growth of the activated monocytes is larger than the growth found in literature [Deventer et al., 1990] since the down-regulation from IL-10 has not been incorporated. In response to TNF-α's growth, IL-6 and IL-8 are produced and their production is up-regulated by TNF-α. Thus, we have

$$\frac{d\text{IL6}}{dt} = \left(k_{6M} + k_{6\text{TNF}}H_{\text{IL6}}^{U}(\text{TNF})\right)M_A - k_6(\text{IL6} - q_{\text{IL6}}),$$

$$\frac{d\text{IL8}}{dt} = \left(k_{8M} + k_{8\text{TNF}}H_{\text{IL8}}^{U}(\text{TNF})\right)M_A - k_8(\text{IL8} - q_{\text{IL8}}).$$

The values of $k_{6\text{TNF}}$ and $k_{8\text{TNF}}$ are chosen such that the observed increase in IL-6 and IL-8 is more than the amounts in the experimental data since the down-regulation from IL-10 has not been incorporated.

About an hour after the pathogen is injected, the anti-inflammatory mediator IL-10 is produced by the activated monocytes and is up-regulated by IL-6. These interactions are modeled by

$$\frac{d\text{IL10}}{dt} = \left(k_{10M} + k_{106}H_{\text{IL10}}^{U}(\text{IL6})\right)M_A - k_{10}(\text{IL10} - q_{\text{IL10}}).$$

Finally, the down-regulation from IL-10 on the pro-inflammatory cytokines and monocytes, as well as the down-regulation of TNF-α and IL-6 by IL-6, are incorporated into the model giving

$$\frac{dM_R}{dt} = -H_M^{U}(P)\left(k_M + k_{M\text{TNF}}H_M^{U}(\text{TNF})\right)H_M^{D}(\text{IL10})M_R + k_{MR}M_R\left(1 - \frac{M_R}{M_\infty}\right),$$

$$\frac{dM_A}{dt} = H_M^{U}(P)\left(k_M + k_{M\text{TNF}}H_M^{U}(\text{TNF})\right)H_M^{D}(\text{IL10})M_R - k_{MA}M_A,$$

$$\frac{d\text{TNF}}{dt} = k_{\text{TNFM}}H_{\text{TNF}}^{D}(\text{IL6})H_{\text{TNF}}^{D}(\text{IL10})M_A - k_{\text{TNF}}(\text{TNF} - q_{\text{TNF}}),$$

$$\frac{d\text{IL6}}{dt} = \left(k_{6M} + k_{6\text{TNF}}H_{\text{IL6}}^{U}(\text{TNF})\right)H_{\text{IL6}}^{D}(\text{IL6})H_{\text{IL6}}^{D}(\text{IL10})M_A - k_6(\text{IL6} - q_{\text{IL6}}),$$

$$\frac{d\text{IL8}}{dt} = \left(k_{8M} + k_{8\text{TNF}}H_{\text{IL8}}^{U}(\text{TNF})\right)H_{\text{IL8}}^{D}(\text{IL10})M_A - k_8(\text{IL8} - q_{\text{IL8}}).$$

5.2.4   Parameterization of Hill Functions

Ideally, the values for the half-maximum constants and exponents should be chosen by fitting a Hill function to a curve representing the interaction between X and Y. However, available experimental data fails to isolate these relationships. Thus, the parameters of the Hill function were parameterized using the relationships found in previous literature [Chow et al., 2005; Clermont et al., 2004b], as well as by studying the behavior of the model output in response to changes in the parameter values.

Since our overall goal is to fit the model to data, it is beneficial to reduce the number of parameters, if possible. To do so, if mediator A is up-regulating mediators B and C, then the same half-maximum value is chosen to represent this interaction in the corresponding equation. That is, if the interaction between mediators (A, B) and between mediators (A, C) are represented by

$$\frac{A^{h_B}}{\eta_{BA}^{h_B} + A^{h_B}} \quad \text{and} \quad \frac{A^{h_C}}{\eta_{CA}^{h_C} + A^{h_C}}, \tag{5.9}$$

respectively, then $\eta_{BA} = \eta_{CA}$. This half-maximum value is initially chosen to be approximately 50% of the maximal value of mediator A, and subsequently increased/decreased to attain the necessary increase or decrease in the state. A similar approach is used to find the half-maximum values for the down-regulatory interactions. Note that the exponents in each sigmoidal equation are able to vary between interactions; that is, $h_B \neq h_C$. This approach is similar to the one used by Clermont et al. [2004].

Recall that for $\eta_{YX} \gg X$, where η_{YX} is the half-maximum value, H_Y^U approaches zero, while H_Y^D approaches one. Conversely, for $\eta_{YX} \ll X, H_Y^U$ approaches one, while H_Y^D approaches zero. An illustration of this effect is shown in Figure 5.3. Thus, while the half-maximum values and exponents need to ensure the the necessary increase or decrease, its also necessary to verify that they are not primarily approaching zero or one. This can be done by analyzing the plots of H versus time and of H versus X.

5.2.5   Parameter Scaling

The parameter values chosen produce relative increases/decreases in the state variables. However, the magnitude of these dynamics are not guaranteed to agree with the experimental data. This can

be rectified by scaling the model output and then incorporating this scaling into the parameter values. That is, state X can be scaled by a factor ν, which in turn causes all of the parameters associated with X to be scaled by ν.

For example, when TNF-α is incorporated into the equation for IL-6, parameters are changed until a relative increase in IL-6 is observed. If the output for IL-6 needs to be scaled by a factor of ν in order to get the model output to have the same magnitude as the mean response, then

$$\widetilde{\text{IL6}} = \nu\text{IL6} \quad \Rightarrow \quad \text{IL6} = \frac{1}{\nu}\widetilde{\text{IL6}}.$$

Differentiating $\widetilde{\text{IL6}}$ gives

$$
\begin{aligned}
\frac{d\widetilde{\text{IL6}}}{dt} &= \nu\Big((k_{6M} + k_{6TNF}H_{\text{IL6}}^{U}(\text{TNF}))H_{\text{IL6}}^{D}(\text{IL6})H_{\text{IL6}}^{D}(\text{IL10})M_A\Big) - \nu k_6(\text{IL6} - q_{\text{IL6}}) \\
&= \nu\Big((k_{6M} + k_{6TNF}H_{\text{IL6}}^{U}(\text{TNF}))H_{\text{IL6}}^{D}(\text{IL6})H_{\text{IL6}}^{D}(\text{IL10})M_A\Big) - k_6(\widetilde{\text{IL6}} - \nu q_{\text{IL6}}).
\end{aligned}
$$

Thus, k_{6M}, k_{6TNF}, and q_{IL6} need to be scaled by ν. Each of the Hill functions with IL6 as its independent variable also needs to be rewritten in terms of $\widetilde{\text{IL6}}$. That is, $H_{\text{IL6}}^{D}(\text{IL6}), H_{\text{TNF}}^{D}(\text{IL6})$ and $H_{\text{IL10}}^{U}(\text{IL6})$ need to be rewritten in terms of $\widetilde{\text{IL6}}$. For $H_{\text{Y}}^{D}(\text{IL6})$, we have

$$
\begin{aligned}
H_{\text{Y}}^{D}(\text{IL6}) &= \frac{\eta^h}{\eta^h + \text{IL6}^h} \\
&= \frac{\eta^h}{\eta^h + \left(\frac{1}{\nu}\widetilde{\text{IL6}}\right)^h} \\
&= \frac{(\nu\eta)^h}{(\nu\eta)^h + \widetilde{\text{IL6}}} \\
&= H_{\text{Y}}^{D}(\widetilde{\text{IL6}}),
\end{aligned}
$$

where $Y \in \{\text{TNF-}\alpha, \text{IL-6}\}$ and the nominal half-maximum value $\eta = \eta_{Y\text{IL6}}$ is scaled to become $\nu\eta$. Thus, each of the half-maximum values associated with IL-6 down-regulating another component of the model will need to be scaled by ν. A similar calculation for $H_{\text{IL10}}^{U}(\text{IL6})$, can be used to find that the half-maximum value associated with IL-6 up-regulating IL-10 needs to also be scaled by

ν.

After incorporating the scaling into the initial parameterization, each parameter value was verified to be physiologically sound by removing pathways and verifying that the dynamics were as expected. For example, removing the pathogen prevented the activation of the monocytes (i.e. $M_A = 0, \forall t$) and the mediators remained at steady state. Similarly, removing TNF-α caused a decrease in each of the remaining mediators since their production depends on the concentration of TNF-α. The half-maximum values were also compared against those found in literature [Copeland et al., 2005; Deventer et al., 1990; Martich et al., 1991; Pajkrt et al., 1997b; Poll et al., 1997]. The nominal parameter values are given in Table 5.1.
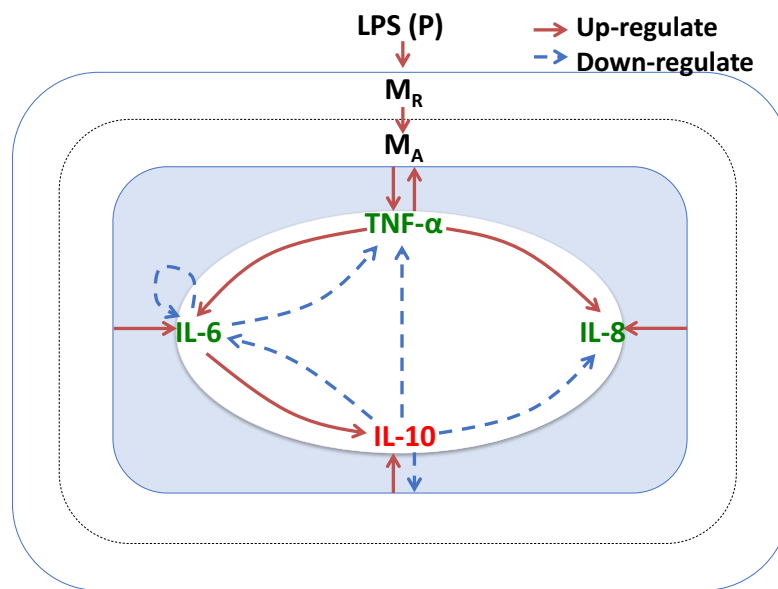
Figure 5.1 *Interactions between the main components of the inflammatory response to endotoxin.* Intravenous injection of LPS activates circulating monocytes M_R, changing them into activated monocytes M_A. This initiates the production of TNF-α. At the same time, monocytes are activated to produce IL-6 and IL-8. All three mediators work in a positive feedback loop, amplifying the inflammatory response by activating more monocytes to stimulate production of IL-6, IL-8, and TNF-α. The production of the anti-inflammatory mediator IL-10 is stimulated by LPS and the elevated levels of the pro-inflammatory mediators; this protects against an excessive inflammatory response. The solid lines represent up-regulation, while the dashed lines represent down-regulation.
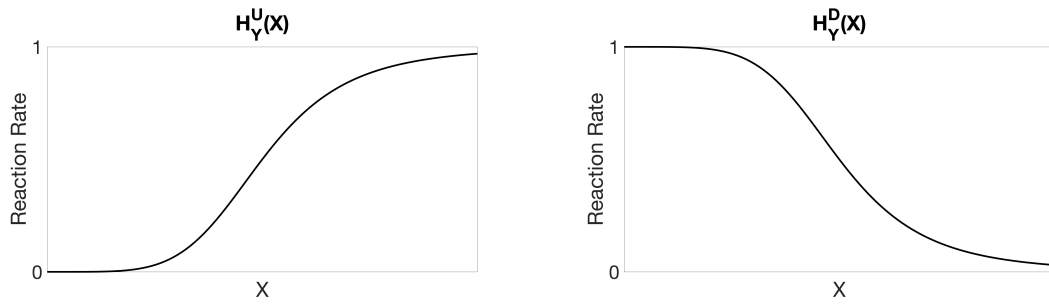
Figure 5.2 *Up- and down-regulation Hill functions.* The up-regulatory function is shown on the left, while the down-regulatory function is shown on the right. The reaction rate, H, is a function of the half-maximum value η, the exponent h, and the substrate concentration X.
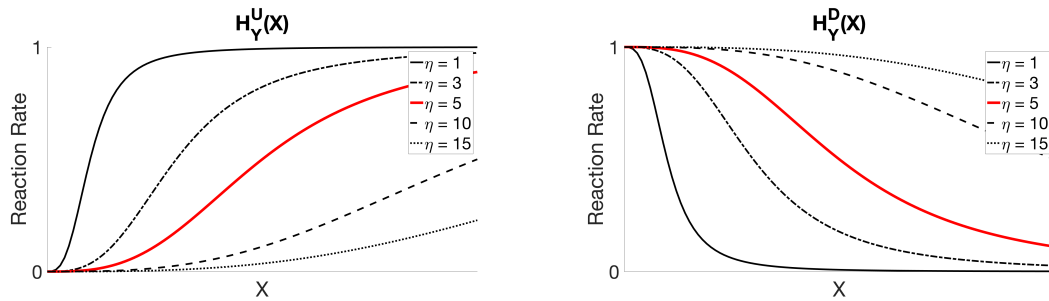
Figure 5.3 *Comparison of Hill functions using varying levels of the half-maximum value.* For each plot, the exponent remains constant, while the half-maximum value is allowed to vary, where $X \in [0, 10]$ and $h = 3$.

Table 5.1 *Inflammatory model nominal parameter values and units.*

No.	Parameter	Value	Unit	No.	Parameter	Value	Unit
1	k_{10}	0.8	hr^{-1}	23	h_{106}	3.68	-
2	k_{10M}	0.0191	$\frac{\text{pg}}{\text{mL}\cdot\text{hr}\cdot\text{noc}}$	24	$h_{t6\text{TNF}}$	2	-
3	k_6	0.66	hr^{-1}	25	h_{66}	1	-
4	k_{6M}	0.81	$\frac{\text{pg}}{\text{mL}\cdot\text{hr}\cdot\text{noc}}$	26	h_{610}	4	-
5	k_8	0.66	hr^{-1}	27	$h_{8\text{TNF}}$	3	-
6	k_{8M}	0.56	$\frac{\text{pg}}{\text{mL}\cdot\text{hr}\cdot\text{noc}}$	28	h_{810}	1.5	-
7	k_{TNF}	1	hr^{-1}	29	$h_{\text{TNF}10}$	3	-
8	$k_{\text{TNF}M}$	0.6	$\frac{\text{pg}}{\text{mL}\cdot\text{hr}\cdot\text{noc}}$	30	$h_{\text{TNF}6}$	2	-
9	k_{MA}	2.51	hr^{-1}	31	h_{M10}	0.3	-
10	k_{MR}	0.006	hr^{-1}	32	$h_{M\text{TNF}}$	3.16	-
11	k_P	1.01	hr^{-1}	33	h_{MP}	1	-
12	η_{610}	34.8	pg/mL	34	q_{TNF}	1.08	pg/mL
13	η_{66}	560	pg/mL	35	$q_{\text{IL}10}$	0.248	pg/mL
14	$\eta_{6\text{TNF}}$	185	pg/mL	36	$q_{\text{IL}8}$	1.42	pg/mL
15	η_{810}	17.4	pg/mL	37	$q_{\text{IL}6}$	0.317	pg/mL
16	$\eta_{8\text{TNF}}$	185	pg/mL	38	k_M	0.0414	hr^{-1}
17	η_{106}	560	pg/mL	39	M_∞	30000	# of cells
18	$\eta_{\text{TNF}10}$	17.4	pg/mL	40	$k_{6\text{TNF}}$	0.81	$\frac{\text{pg}}{\text{mL}\cdot\text{hr}\cdot\text{noc}}$
19	$\eta_{\text{TNF}6}$	560	pg/mL	41	$k_{8\text{TNF}}$	0.56	$\frac{\text{pg}}{\text{mL}\cdot\text{hr}\cdot\text{noc}}$
20	η_{MP}	3.3	ng/kg	42	k_{106}	0.0191	$\frac{\text{pg}}{\text{mL}\cdot\text{hr}\cdot\text{noc}}$
21	η_{M10}	4.35	pg/mL	43	$k_{M\text{TNF}}$	4.14E-06	hr^{-1}
22	$\eta_{M\text{TNF}}$	100	pg/mL				

The abbreviation noc is the number of cells present.

CHAPTER

6

INFLAMMATORY MODEL ANALYSIS &
RESULTS

The sensitivity analysis, identifiability analysis, and optimization techniques presented in Chapter 4 have been applied to the inflammatory model and the results are presented in Sections 6.2, 6.3, and 6.5, respectively. Uncertainty quantification was used to verify the results of the local methods. These results are shown and discussed in Section 6.6.

6.1 Least Squares Formulation

To personalize the mathematical model of the inflammatory response, discussed in Chapter 5, we aim to find a parameter set $\hat{\theta}$ that minimizes the square of the error between the computed and

measured values of the inflammatory mediators, TNF-α, IL-10, IL-6, and IL-8. That is,

$$\hat{\theta} = \arg \min_{\theta} J(\theta), \quad \text{where } J(\theta) = R^T R. \tag{6.1}$$

The model output y and data Y given by

$$y = [\text{TNF-}\alpha_1^C, \ldots, \text{TNF-}\alpha_N^C, \text{IL-}10_1^C, \ldots, \text{IL-}10_N^C, \text{IL-}6_1^C, \ldots, \text{IL-}6_N^C, \text{IL-}8_1^C, \ldots \text{IL-}8_N^C],$$

$$Y = [\text{TNF-}\alpha_1^D, \ldots, \text{TNF-}\alpha_N^D, \text{IL-}10_1^D, \ldots, \text{IL-}10_N^D, \text{IL-}6_1^D, \ldots, \text{IL-}6_N^D, \text{IL-}8_1^D, \ldots \text{IL-}8_N^D]$$

respectively, are used to define the residual $R \in \mathbb{R}^{4N}$ between the model output and the data. Due to differences in the magnitudes of the mediators, it is necessary to divide by the mean of the data so that the residual R is defined as

$$R = \frac{1}{\sqrt{N}} \left[\frac{\text{TNF-}\alpha^C - \text{TNF-}\alpha^D}{\overline{\text{TNF-}\alpha^D}}, \frac{\text{IL-}10^C - \text{IL-}10^D}{\overline{\text{IL-}10^D}}, \frac{\text{IL-}6^C - \text{IL-}6^D}{\overline{\text{IL-}6^D}}, \frac{\text{IL-}8^C - \text{IL-}8^D}{\overline{\text{IL-}8^D}} \right]^T.$$

Prior to finding $\hat{\theta}$, sensitivity and identifiability analysis are used to reduce the parameter set into the sensitive and uncorrelated parameters.

6.2 Sensitivity Analysis

Recall from Chapter 4 that the sensitivity of the model to changes in the parameters can be computed from the sensitivity matrix defined by $\chi = \frac{\partial y}{\partial \theta}$. For the inflammatory model, we use

$$\chi = \frac{\partial R}{\partial \theta} = \begin{bmatrix} \frac{\partial y_1(t_1)}{\partial \theta_1} & \cdots & \frac{\partial y_1(t_1)}{\partial \theta_q} \\ \vdots & \ddots & \vdots \\ \frac{\partial y_1(t_N)}{\partial \theta_1} & \cdots & \frac{\partial y_1(t_N)}{\partial \theta_q} \\ \frac{\partial y_2(t_1)}{\partial \theta_1} & \cdots & \frac{\partial y_2(t_1)}{\partial \theta_q} \\ \vdots & \ddots & \vdots \\ \frac{\partial y_m(t_N)}{\partial \theta_1} & \cdots & \frac{\partial y_m(t_N)}{\partial \theta_q} \end{bmatrix}. \tag{6.2}$$

Figure 6.1 *Sensitivities of the inflammatory model.* Relative parameter sensitivities ranked the most to the least sensitive. The black line shows the cutoff between sensitive and insensitive parameters. The cutoff ϕ was chosen to be $10\sqrt{\varphi}$, where $\varphi = 10^{-8}$ is the integration tolerance. Red squares and parameters listed in red denote sensitive parameters that are considered for optimization.

To ensure that the parameter values remain positive during the optimization, we use $\tilde{\theta} = \log\theta$. Then

$$\chi = \frac{\partial R}{\partial \tilde{\theta}} = \frac{\partial R}{\partial \log\theta} = \frac{\partial R}{\partial \theta}\theta.$$

Thus, χ is actually a relative sensitivity matrix $\tilde{\chi}$. The ranked sensitivities, computed by taking the two-norm of the sensitivity matrix, are shown in Figure 6.1. Using a cutoff of $\phi = 10\sqrt{\varphi}$, the parameters are divided into 39 sensitive and 4 insensitive parameters.

6.3   Identifiability Analysis & Subset Selection

Among the 39 sensitive parameters, identifiability analysis and subset selection are used to identify parameters that cannot be uniquely estimated due to the structure of the model and linear correlations.

Due to the complexity of the inflammatory model, the input-output method used for the mSIRS model in Chapter 4 cannot be replicated for the inflammatory model. However, additional insight can be obtained by analyzing the equations and parameters of the model, particularly the Hill functions and rate constants.

Hill Functions

Recall that the Hill functions, shown in Figure 5.3 of Chapter 5, as well as their respective equations

$$H_Y^U(X) = \frac{X^h}{\eta_{YX}^h + X^h} \quad \text{and} \quad H_Y^D(X) = \frac{\eta_{YX}^h}{\eta_{YX}^H + X^h},$$

show that for $\eta_{YX} \gg X$, H_Y^U approaches 0, while H_Y^D approaches 1. Conversely, for $\eta_{YX} \ll X$, H_Y^U approaches 1, while H_Y^D approaches 0. Without proper bounds on η_{YX}, attempting to fit the model to the experimental data can force these values to become either very large or very small, depending on the equation. Thus, we have chosen to fix the half-maximum values and their respective exponents at their nominal values.

Rate Constants

Although both k_M and k_{MTNF} are sensitive, as shown in Figure 6.1, prior attempts at optimizing both parameters have resulted in k_M being very large and k_{MTNF} being very small. If that is the case, then from

$$\frac{dM_R}{dt} = -H_M^U(P)(k_M + k_{MTNF}H_M^U(TNF))H_M^D(IL10)M_R + k_{MR}M_R\left(1 - M_R/M_\infty\right),$$

that means that the pathway between TNF-α and the monocytes becomes nonexistent. Literature shows that this an essential pathway in the activation of the monocytes and further production of the inflammatory mediators [Chow et al., 2005; Rossol et al., 2011; Schulte et al., 2013]. Thus, both parameters cannot be accurately estimated so one will have to remain fixed, while the other is estimated. The same condition is necessary for the pairs $(k_{6M}, k_{6TNF}), (k_{8M}, k_{8TNF})$, and (k_{10M}, k_{106}).

As mentioned in Chapter 5, the carrying capacity M_∞ of the monocytes and the source term q_i for each inflammatory mediator are also fixed at its nominal value, as their values are based on

the values found in literature [Deventer et al., 1990] and the experimental data. The time-varying sensitivities for the remaining 15 sensitive parameters are shown in Figure 6.2.

Practical Identifiability

The structural correlation method (SCM) [Olufsen & Ottesen, 2013], described in Chapter 4, is used on the remaining 15 parameters to test for linear pairwise correlations. Using a correlation tree, similar to that found in [Olufsen & Ottesen, 2013], three parameter subsets are identified. Subsequently, Delayed Rejection Adaptive Metropolis (DRAM) is used to verify the results of this analysis, explained in Section 6.6.2.

Subset 1

Subset 1 is found by first fixing k_M, k_{6M}, k_{8M}, and k_{10M}. Following the algorithm given in Chapter 4, the relative sensitivity matrix, $\tilde{\chi}$, is recomputed using the new subset and the parameters are ranked from most to least sensitive. Computing the correlation coefficients, c_{ij}, defined in (4.17) of Chapter 4, removing the least sensitive correlated parameter and repeating this process produces a subset with 10 parameters,

$$\text{Subset 1: } \{k_{10}, k_6, k_8, k_{\text{TNF}}, k_{\text{TNF}M}, k_{MA}, k_P, k_{8\text{TNF}}, k_{106}, k_{M\text{TNF}}\}. \tag{6.3}$$

Subset 2

For Subset 2, k_{MTNF}, k_{6TNF}, k_{8TNF}, and k_{106} are fixed and the SCM produces a second subset, containing 8 parameters given by

$$\text{Subset 2: } \{k_{10}, k_{10M}, k_6, k_8, k_{\text{TNF}}, k_{\text{TNFM}}, k_P, k_{8M}\}. \tag{6.4}$$

Subset 3

Notice that for Subset 2, at least two parameters are being included for each inflammatory mediator, except for IL-6. For instance $k_{\text{TNF}M}$ and k_{TNF} for TNF-α and k_{10} and k_{10M} for IL10. Appending k_{6M} to Subset 2 does not produce any additional pairwise linear correlations, creating another subset,
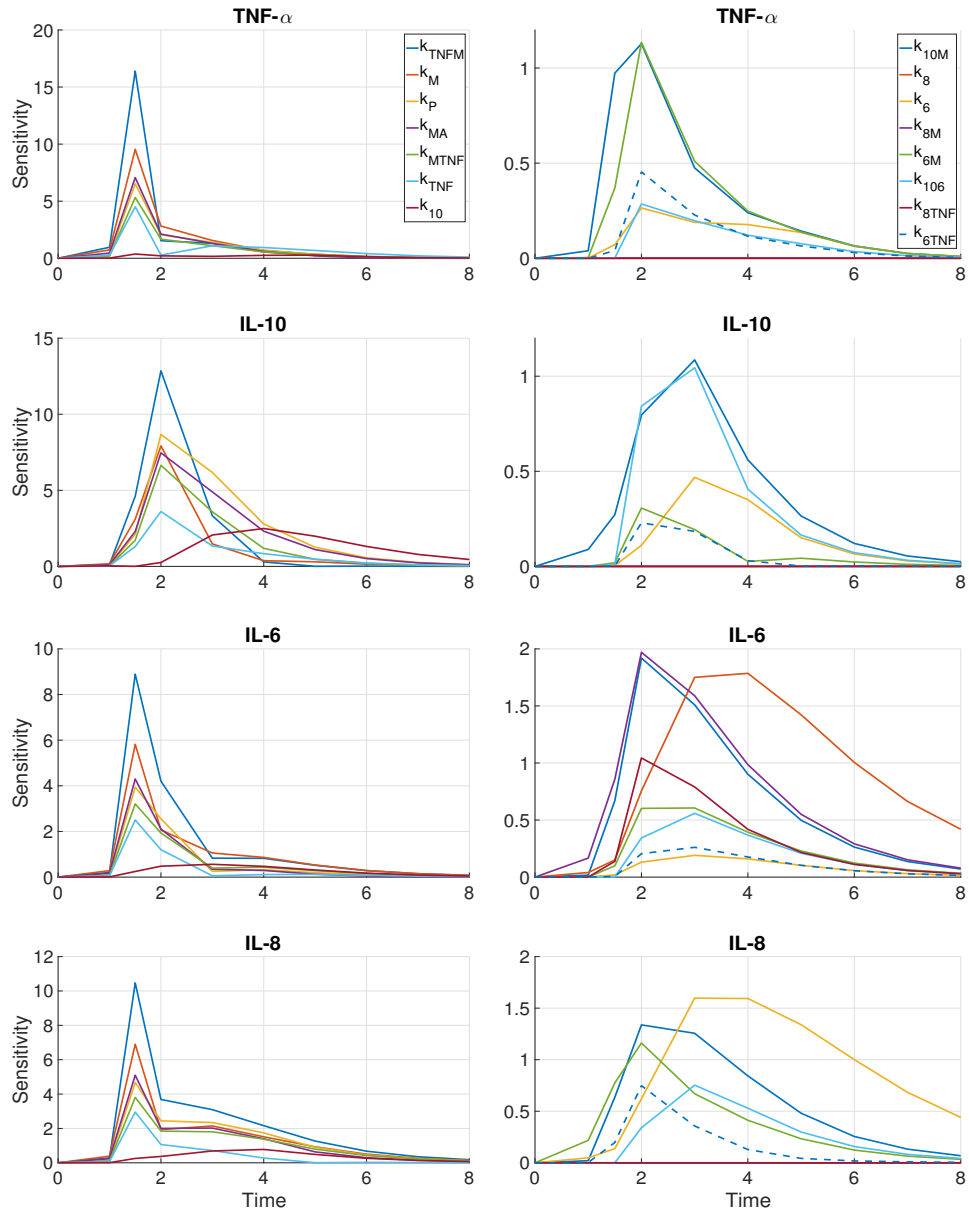
Figure 6.2 *Time-varying sensitivities for the sensitive parameters considered for optimization (evaluated at times where data was available).* The columns on the left include the seven most sensitive parameters and the columns on the right include the final eight parameters.

namely

$$\text{Subset 3: } \{k_{10}, k_{10M}, k_6, k_{6M}, k_8, k_{\text{TNF}}, k_{\text{TNF}M}, k_P, k_{8M}\}. \tag{6.5}$$

6.4   Parameter Estimation

To render the model patient-specific, the parameters are optimized using a combination of the Nelder-Mead and Levenberg-Marquardt algorithms for the three subsets defined above. The lower and upper bounds for Levenberg-Marquardt are set to be one-quarter of and four times the nominal parameter values, respectively. Imposing these bounds ensures that the optimization results are physiologically sound.

The scaling technique explained in Section 5.2.5 of Chapter 5 is used to create a patient-specific nominal parameter set for each data set. This allows for a better approximation of the optimal parameter set and provides an efficient way to determine the half-maximum values of a function without optimization. It is important to verify that the scaling has not caused the Hill function to go toward zero or one and in the case of terms of the form $k_1 + k_2 H_Y^U(X)$, it is important to verify that k_1 and k_2 remain individually identifiable.

Figure 6.3 shows the effect of scaling the half-maximum values η_{Y6}, as well as k_{6M}, $k_{6\text{TNF}}$, and q_6 by $\nu_1 < 1$. In the Hill function

$$H_{\text{IL}10}^U(\text{IL}6) = \frac{\text{IL}6^h}{\eta_{106}^h + \text{IL}6^h},$$

η_{106} is multiplied by ν_1, causing the Hill function to increase. This scaling results in a decrease in IL-6, without changing IL-10. This scaling is further incorporated into all terms involving the remaining mediators so that they remain unchanged as well. Notice that this scaling does not cause the Hill function to be flat (i.e. primarily close to 0 or 1).

In Figure 6.4, each of the half-maximum values associated with IL-10, η_{Y10}, as well as the k_{106} and k_{10M} terms are scaled by $\nu_2 > 1$. For these parameters, the Hill function (shown in the top left) does not change since the half-maximum value associated with this equation is $\eta_{Y\text{IL}6}$. However, when combined with the scalings of k_{10M} and k_{106}, IL-10 decreases. Combining the scalings used for IL-6 and IL-10 results in a decrease in both IL-6 and IL-10, shown in Figure 6.5.

After incorporating the appropriate scaling, each parameter subset, (6.3), (6.4) and (6.5), is
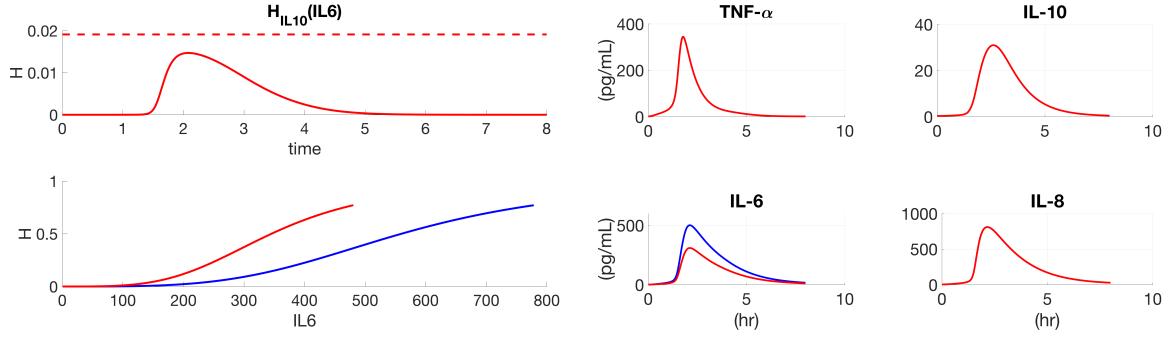
Figure 6.3 *Effects of scaling parameters associated with IL-6.* Changes in the Hill function $H_{\text{IL}10}^{U}(\text{IL6})$ and model output in response to scaling the IL-6 model output (scaled η_{Y6}, k_{6M}, $k_{6\text{TNF}}$, and q_6 by $v_1 < 1$). Blue lines are with nominal parameter set and red lines are with scaled parameter set. Top left panel shows $k_{106}H_{\text{IL}10}^{U}(\text{IL6})$ (solid line) and k_{10M} (dashed line) versus time. Bottom left panel shows $H_{\text{IL}10}^{U}(\text{IL6})$ versus IL-6. Inflammatory mediator outputs (right).
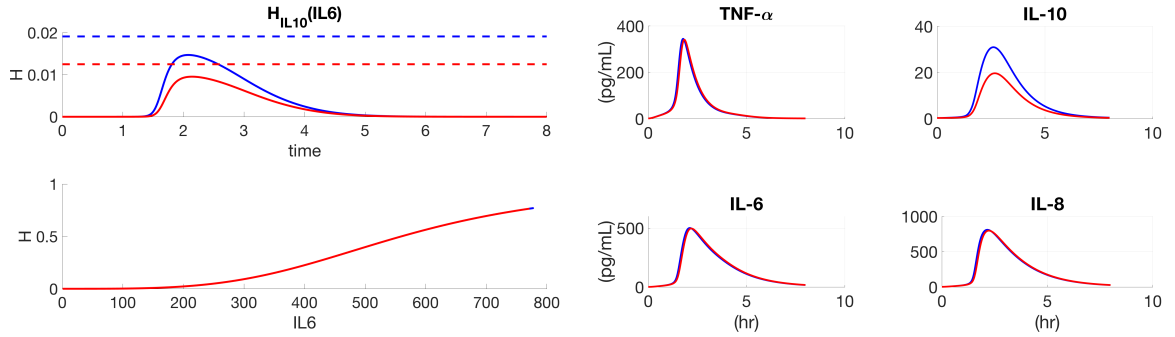
Figure 6.4 *Effects of scaling parameters associated with IL-10.* Changes in the Hill function $H_{\text{IL}10}^{U}(\text{IL6})$ and model output in response to scaling the IL-10 model output (scaled η_{Y10}, k_{106} and k_{10M} by $v_2 > 1$). Blue lines are with nominal parameter set and red lines are with scaled parameter set. Top left panel shows $k_{106}H_{\text{IL}10}^{U}(\text{IL6})$ (solid line) and k_{10M} (dashed line) versus time. Bottom left panel shows $H_{\text{IL}10}^{U}(\text{IL6})$ versus IL-6. Inflammatory mediator outputs (right).
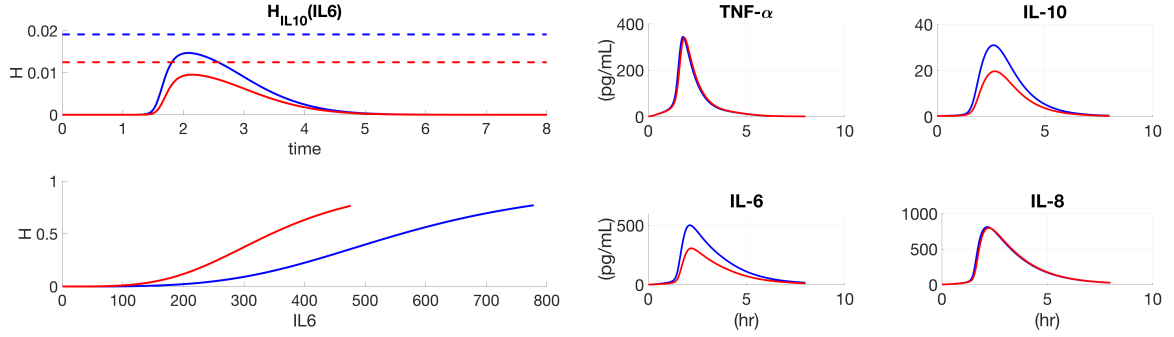
Figure 6.5 *Effects of scaling parameters associated with IL-6 and IL-10.*Changes in the Hill function H_{IL10}^U(IL6) and model output in response to scaling both the IL-6 & IL-10 model outputs (scaled $\eta_{Y6}, k_{6M}, k_{6\text{TNF}}, q_6, \eta_{Y10}, k_{106}$ and k_{10M}). Blue lines are with nominal parameter set and red lines are with scaled parameter set. $k_{106}H_{\text{IL10}}^U$(IL6) versus time (solid line) and k_{10M} (dashed line) (top left). H_{IL10}^U(IL6) versus IL6 (bottom left). Inflammatory mediator outputs (right).

optimized. Recall from Chapter 4 that the Levenberg-Marquardt algorithm is a gradient based method, which requires a "good" nominal set in order to find the local minimum of the cost function, J. Due to its ability to find an absolute, rather than local, minimum of J, the parameters are first optimized using Nelder-Mead. These subsequent parameters define a new nominal set that is then optimized using Levenberg-Marquardt. Alternatively, assuming that the scaled parameter values constitute a "good" nominal set, Levenberg-Marquardt can used without using Nelder-Mead first. Consequently, three separate results are obtained for each subset: (1) Nelder-Mead only, (2) Levenberg-Marquardt only, and (3) Nelder-Mead followed by Levenberg-Marquardt.

6.5   Results

The R^2 statistic was used to quantify the accuracy of the model. It provides a measure of how well the data are replicated by the model, computed by taking the ratio of the sum of squares explained

by the regression model and the total sum of squares error around the mean. That is,

$$R^2 = 1 - \frac{SSE}{SST},$$

where

$$SSE = \sum_i^N (y_i - Y_i)^2 \quad \text{and} \quad SST = \sum_i^N (Y_i - \overline{Y})^2.$$

Between the three optimal parameter sets (Levenberg-Marquardt only, Nelder-Mead only, and Nelder-Mead followed by Levenberg Marquardt), the set with the largest R^2 values is accepted as the optimal set.

Figure 3.2 of Chapter 3 depicts the data set that most resembles the mean response. Subsequent results will be shown against this data set, unless stated otherwise. The optimal parameter values using Subsets 1 through 3 for this data set are shown in Table 6.1 and the fits to the data are shown in Figure 6.6. Table 6.1 also includes the mean plus/minus the standard deviation, excluding these abnormal responses, which were identified using box-and-whisker plots (discussed in Chapter 3).

Subset 1

For Subset 1, Figure 6.6 and Table 6.1 show that the R^2 values are significantly higher than for other other subsets and the model fits the data well. However, to obtain these fits, the optimized values obtained using Levenberg-Marquardt were forced to their upper and lower bounds. Using the imposed bounds of $\theta/4$ and 4θ, where θ was the nominal scaled parameter set, the optimizer forced k_P, k_{106}, and/or k_{MTNF} to touch the lower bound in 16 out of the 20 datasets. Expanding those bounds to be $\theta/8$ and 8θ resulted in the same issue. Thus, Subset 1 actually provides worse results than the other two subsets.

Subsets 2 & 3

The model fits and R^2 values for Subsets 2 and 3 are shown n Figure 6.6. Although the R^2 values are lower than those of Subset 1, the Levenberg-Marquardt optimizer did not force the parameters to their upper or lower bounds. Table 6.2 shows that Subset 3 outperforms Subset 2 in accurately modeling the response over all of the data sets; particularly, in modeling the IL-6 response, which

Table 6.1 *Nominal parameter values and optimal parameter values for Subsets 1 through 3.* Nominal and optimal parameter values are for a particular subject after scaling and then optimizing using Nelder-Mead and Levenberg-Marquardt. The mean plus/minus the standard deviation for each subset is also included. The final two rows show the minimum and maximum R^2 over all mediators for all data sets.

Parameter	Nominal θ	Subset 1 $\hat{\theta}$	Subset 1 Mean ± Std	Subset 2 $\hat{\theta}$	Subset 2 Mean ± Std	Subset 3 $\hat{\theta}$	Subset 3 Mean ± Std
k_{10}	0.800	0.866	0.776 ± 0.199	0.883	0.826 ± 0.191	0.976	0.870 ± 0.281
k_{10M}	0.019			0.009	0.011 ± 0.007	0.008	0.009 ± 0.004
k_6	0.660	0.870	0.885 ± 0.209	0.775	0.897 ± 0.319	0.669	0.751 ± 0.198
k_{6M}	0.810					0.271	0.343 ± 0.178
k_8	0.660	0.846	0.776 ± 0.115	0.705	0.710 ± 0.109	0.691	0.663 ± 0.095
k_{8M}	0.560			0.539	0.671 ± 0.191	0.338	0.278 ± 0.126
k_{TNF}	1.000	1.708	1.579 ± 0.195	1.402	0.788 ± 0.489	1.611	1.710 ± 0.370
$k_{\text{TNF}M}$	0.600	0.781	0.898 ± 0.517	0.661	0.788 ± 0.386	0.620	0.721 ± 0.442
k_{MA}	2.510	2.946	3.659 ± 1.653				
k_P	1.010	0.236	0.267 ± 0.042	1.006	1.062 ± 0.088	0.795	0.769 ± 0.229
$k_{8\text{TNF}}$	0.560	0.608	0.680 ± 0.255				
k_{106}	0.019	2.87E-03	9.90E-03 ± 7.82E-03				
$k_{M\text{TNF}}$	4.14E-06	1.74E-06	5.48E-05 ± 1.87E-04				
R^2_{min}		0.8		0.71		0.71	
R^2_{max}		1		0.99		1	

may be attributed to estimating k_{6M} in Subset 3, but not in Subset 2. Subset 3 also predicts the maximum of the response better than the remaining subsets, as shown in Figure 6.6. Additionally the regression line for Subset 3, shown by the black lines in Figure 6.7, align with $y = x$ better than for Subset 2. Thus, all subsequent results will be shown using optimal parameters from Subset 3.

DRAM was also used to identify correlations between parameters globally. The results, shown in Section 6.6.2, support the argument that Subset 3 is the best.

6.5.1 Normal versus Abnormal Responses

As previously mentioned, the data was separated into a set of normal and abnormal responders, using Box-and-Whisker plots. To understand what is causing one type of response versus another,
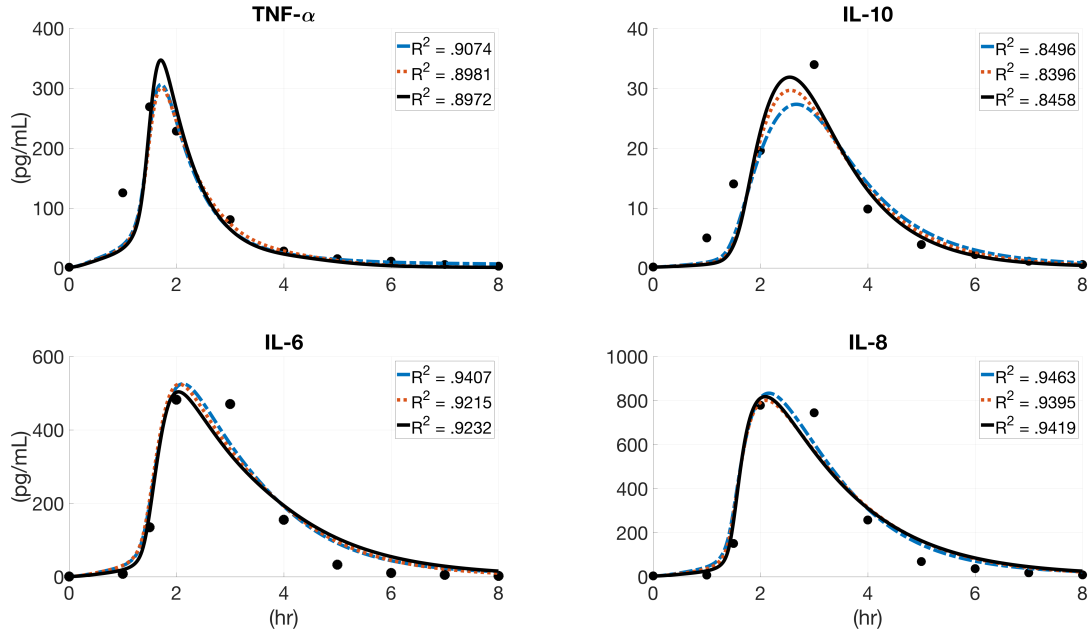
Figure 6.6 *Comparison of model predictions of Subsets 1 through 3.* Data (black circles) and model fits for mean data set (shown in red in Figure 3.2) after intravenous administration of endotoxin. Optimization using Subsets 1,2, and 3 are denoted by the blue dashed, red dashed line, and black solid lines, respectively. The participant was given 2 ng/kg body weight of endotoxin at $t = 0h$, and inflammatory mediator levels were measured at $t = -2, 0, 1, 1.5, 2h$ and hourly for the next 4 hours. Pseudodata was added at $t = 7$ and 8h to ensure that mediators had appropriate time to decay.

we compared the response between a normal responder (the subject depicted in Figure 6.6) and an abnormal responder, shown in Figure 6.8.

The differences in the observed responses caused noteworthy contrasts in the parameter values. Major differences include $k_{\mathrm{TNF}M}$, the rate responsible for the production of TNF-α by the activated monocytes, was almost two times larger in the normal response (normal: 0.620, abnormal: 0.383). In contrast, k_{10M}, the rate responsible for the production of IL-10 by the activated monocytes, was half as large in the normal response (normal: 0.008, abnormal: 0.018). Additionally, k_{6M} was significantly larger in the abnormal response (normal: 0.271, abnormal: 1.220). The decay rate of IL-6, k_6, was almost two times larger in the abnormal response (normal: 0.669, abnormal:

Table 6.2 *Comparison of the average, minimum, and maximum R^2 values for Subsets 1 through 3. R^2* average, minimum, and maximum over all data sets after scaling and then optimizing using Nelder-Mead and Levenberg-Marquardt.

Mediator	R^2	S1	S2	S3	Mediator	R^2	S1	S2	S3
TNF-α	Av	0.94	0.92	0.93	**IL-6**	Av	0.94	0.93	0.94
	Min	0.84	0.71	0.71		Min	0.86	0.71	0.73
	Max	0.99	0.98	0.99		Max	1.00	0.99	1.00
IL-10	Av	0.90	0.89	0.89	**IL-8**	Av	0.94	0.94	0.94
	Min	0.80	0.79	0.78		Min	0.88	0.88	0.87
	Max	0.97	0.96	0.96		Max	0.98	0.97	0.99

1.217).

The abnormal response shown in Figure 6.8 demonstrates a particular type of response. In classifying the abnormal responders, three individuals exhibited a low level of TNF-α accompanied by high levels of IL-10, two individuals had high levels of both TNF-α and IL-10, and one individual had an increased level of IL-6 and IL-8.

6.5.2 Model Validation

As mentioned in Chapter 3, the analysis of the inflammatory model was developed using the Day A data only. The model was validated by running the model with the optimal parameters for Day A against the data for Day B. It should be noted that the initial conditions and source terms q were set based on the data for Day B. A comparison of the results for a particular subject for Day A versus Day B is shown in Figure 6.9. For this individual, the R^2 values changed by 0.11 or less. The average change in the R^2 values over the subjects classified as normal for both days was between 0.03 and 0.12. For those classified as abnormal for both study days, the average change in the R^2 values was between 0.02 and 0.17.

6.6 Uncertainty Quantification

Recall from Chapter 4 that frequentist and Bayesian methods can be used to quantify the uncertainty in a model. The global Bayesian method DRAM, as well as frequentist parameter confidence intervals, were used to verify the local identifiability analysis results presented above. Prediction,
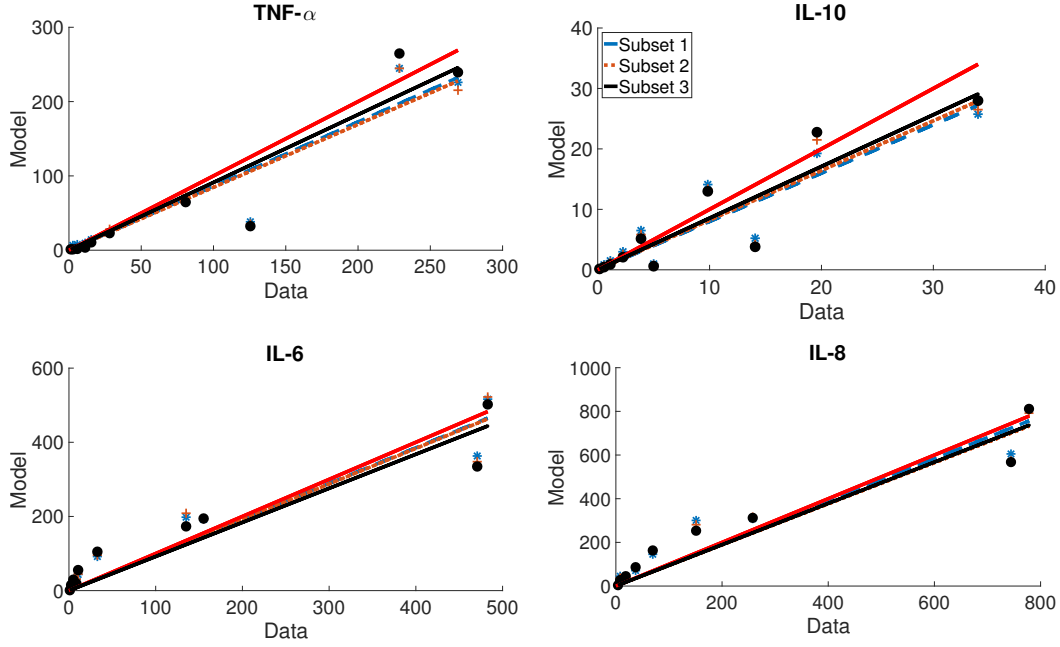
Figure 6.7 *Comparison of the residual plots for Subsets 1 through 3.* Residuals of Subsets 1 through 3 versus the data. The regression lines $y_{\text{model}} = m\, y_{\text{data}}$ are shown by the vertical lines and $y = x$ is shown by the red line.

confidence, and credible intervals were used to quantify the accuracy of the model in predicting the response.

6.6.1 Frequentist Methods

The parameter confidence intervals, given in Table 6.3 verify that Subset 3 is the best. For Subset 1, the parameter confidence intervals for $k_{MA}, k_P, k_{8\text{TNF}}, k_{106}$, and $k_{M\text{TNF}}$ show that there is a high level of uncertainty in estimating these parameters. Comparing the parameter confidence intervals between each subset for k_P show that it can be estimated with confidence once the unidentifiable rate constants are removed. The parameter confidence intervals changed by less than 4% between Subsets 2 and 3 after k_{6M} was included. Thus, the parameters of Subset 3 were the best to optimize.
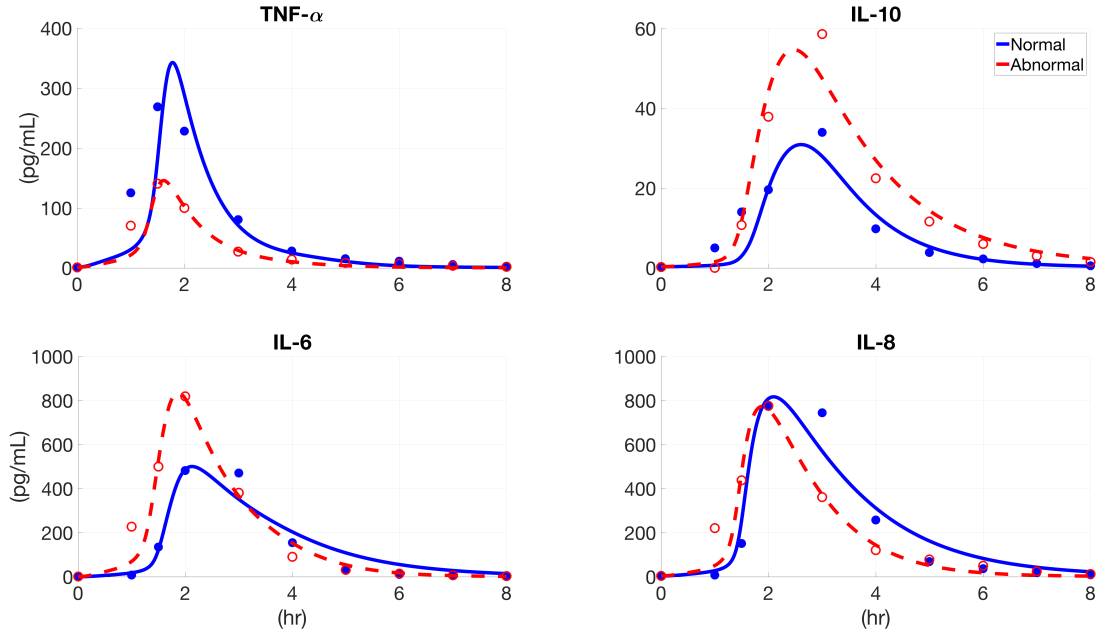
Figure 6.8 *Comparison of model fits between a normal and an abnormal responder.* Model fits for a normal data set (blue line) against the data (blue circles) and for an abnormal data set (red dashed line) against data (red unfilled circles) are shown. Participants were given 2 ng/kg body weight of endotoxin at $t = 0h$, and inflammatory mediator levels were measured at $t = -2, 0, 1, 1.5, 2$ h and hourly for the next 4 hours. Pseudodata was added at $t = 7$ and 8h to ensure that mediators had appropriate time to decay.

Subsets 2 and 3 after k_{6M} was included. Thus, the parameters of Subset 3 were the best to optimize.

The confidence and prediction intervals for the mean data set are shown in Figure 6.10. The width of the intervals show that the model accurately depicts the mean response and that the optimized parameter values provide a reasonable prediction of the data.

6.6.2 Delayed Rejection Adaptive Metropolis

As demonstrated in Chapter 4, DRAM can be used to determine parameter distributions. Figure 6.11 shows the DRAM simulations using the 15 sensitive parameters, previously identified in Figure 6.1. Like the Levenberg-Marquardt method, bounds can be imposed on the parameters in DRAM and
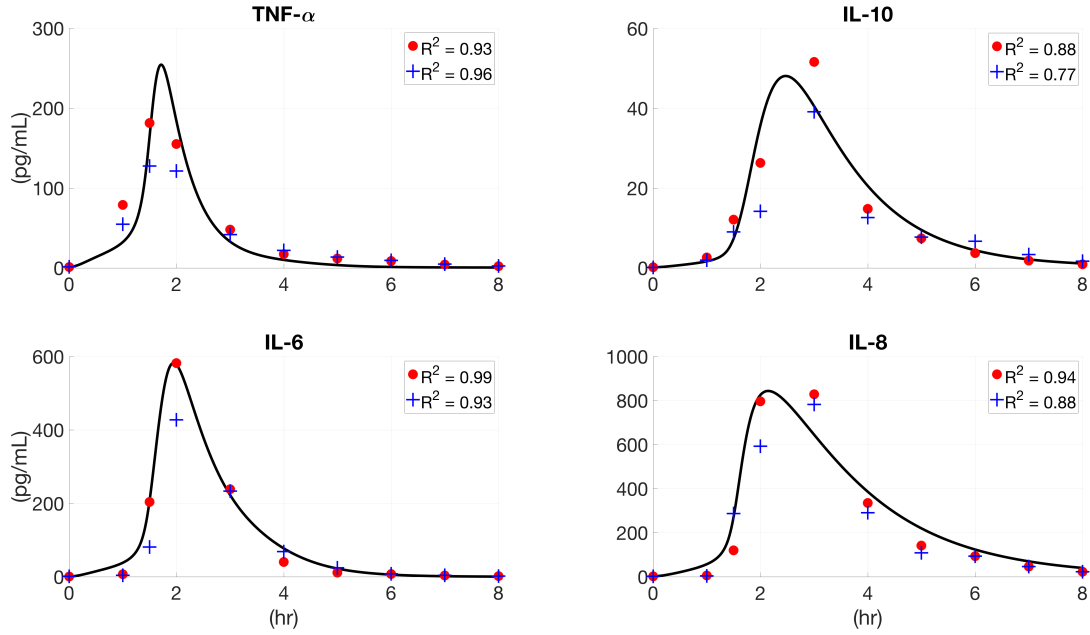
Figure 6.9 *Comparison of model fit to Day A and Day B data.* Model prediction for individual subject plotted against data for Day A (red circles) and Day B (blue crosses). The model was initially optimized against Day A data. Participants were given 2 ng/kg body weight of endotoxin at $t = 0h$, and inflammatory mediator levels were measured at $t = -2, 0, 1, 1.5, 2$h and hourly for the next 4 hours. Pseudodata was added at $t = 7$ and 8h to ensure that mediators had appropriate time to decay.

parameters are expected to converge to an optimal value. The parameter chains and densities in Figure 6.11 demonstrate the difficulty in estimating k_{MA}, k_{6TNF}, k_{8TNF}, and k_{106}, as well as k_{6M}, k_{8M}, and k_P. Figure 6.14 shows an attempt by DRAM to identify any pairwise correlations (i.e. the chains bounce between the bounds and consequently do not converge). The lack of convergence in the parameter chains makes it difficult for DRAM to identify these correlations.

To generate the parameter chains and densities, the DRAM toolbox by Haario et al. requires that an estimator of the variance s^2 is provided. If

$$s^2 = \frac{1}{N-q} J(\hat{\theta}),$$

Table 6.3 *Parameter confidence intervals for Subsets 1 through 3.* Intervals are for the dataset shown in red in Figure 3.2. Highlighted rows show parameter confidence intervals that are significantly large, which is evidence of the uncertainty in estimating said parameter.

Parameter	Subset 1		Subset 2		Subset 3	
	$\hat{\theta}$	$\Delta\hat{\theta}$	$\hat{\theta}$	$\Delta\hat{\theta}$	$\hat{\theta}$	$\Delta\hat{\theta}$
k_{10}	0.866	1.5442	0.883	1.2616	0.976	1.4089
k_{10M}			0.009	0.7576	0.008	0.7846
k_6	0.870	1.6901	0.775	0.9162	0.669	0.9199
k_{6M}					0.271	1.3444
k_8	0.846	1.3681	0.705	0.8910	0.691	0.8767
k_{8M}			0.539	1.4443	0.338	1.7909
k_{TNF}	1.708	2.8330	1.402	2.0561	1.611	2.8596
$k_{\text{TNF}M}$	0.781	0.9587	0.661	0.4945	0.620	0.5118
k_{MA}	2.946	22.4404				
k_P	0.236	5.7398	1.006	1.0049	0.795	1.2897
$k_{8\text{TNF}}$	0.608	2.2291				
k_{106}	2.87E-03	5.6132				
$k_{M\text{TNF}}$	1.74E-06	1.2397				

where the cost function J is defined in 6.1, then s^2 will be large for a small N. Bayesian methods for uncertainty quantification propogate the parameter densities through the model to calculate the credible and prediction intervals. However, having a low number of data points will cause the variance estimator s^2 to be large. Generating synthetic data is necessary to guarantee that this is not the case. To generate the data, the data Y_i is interpolated at the times where the model output is produced. Next, the residual R is computed and using this, we obtain s^2. Thus, the synthetic data is given by

$$Y_{s_i} = g(\tilde{t}_i, x(\tilde{t}_i), \hat{\theta}) + \epsilon, \quad \text{where } \epsilon \sim \mathcal{N}(0, s^2),$$

where $\tilde{t}_i$ are the times that the model output is produced.

Though the optimal parameter values were able to fit the model data well for Subset 1 through 3, DRAM simulations confirmed the problem with estimating particular parameters. As shown in Figure 6.13, the parameter chains produced for Subset 1 hit the pre-set bounds for four out of the ten parameters being estimated, even after they were widened. As a result, the parameter
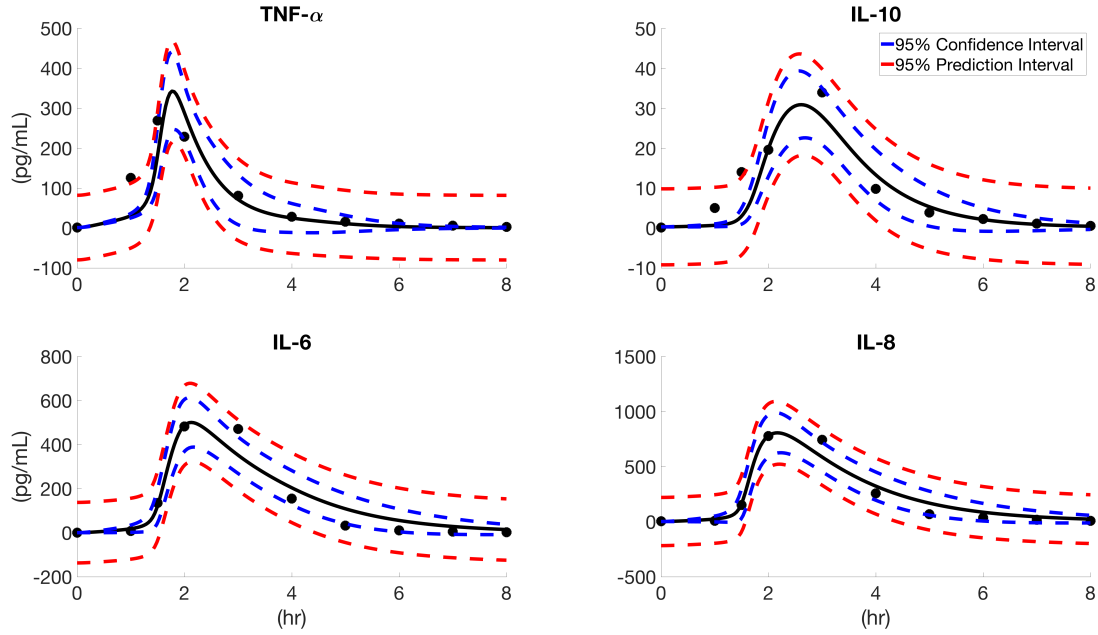
Figure 6.10 *Model fits with confidence and prediction intervals.* Data and model fits for the mean data set after intravenous administration of endotoxin (black). Confidence (blue) and prediction (red) intervals are also shown. The participant was given 2 ng/kg body weight of endotoxin at $t = 0h$, and inflammatory mediator levels were measured at $t = -2, 0, 1, 1.5, 2h$ and hourly for the next 4 hours. Pseudodata was added at $t = 7$ and 8h to ensure that mediators had appropriate time to decay.

densities were wide and inaccurate. Additionally, the parameter chains for k_{MA}, k_P, k_{106}, and $k_{M\text{TNF}}$ produced by DRAM did not converge to an optimal parameter value. The parameter chains and distributions for Subset 3 are shown in Figure 6.13.

For Subset 2, the parameter chains and densities converged well and did not hit the bounds. Thus, this subset can effectively estimate parameters for the model. Recall that the difference between Subsets 2 and 3 was the inclusion of k_{6M}. Including k_{6M} resulted in parameter chains that converged faster than or remained the same as those for Subset 2. Additionally, k_{6M} did not reveal any parameter correlations, though the SCM has previously identified correlations between k_{6M} and the parameters $k_{\text{TNF}M}, k_M, k_P, k_{10M}$ and k_{8M} when k_M and k_{MA} had previously been included
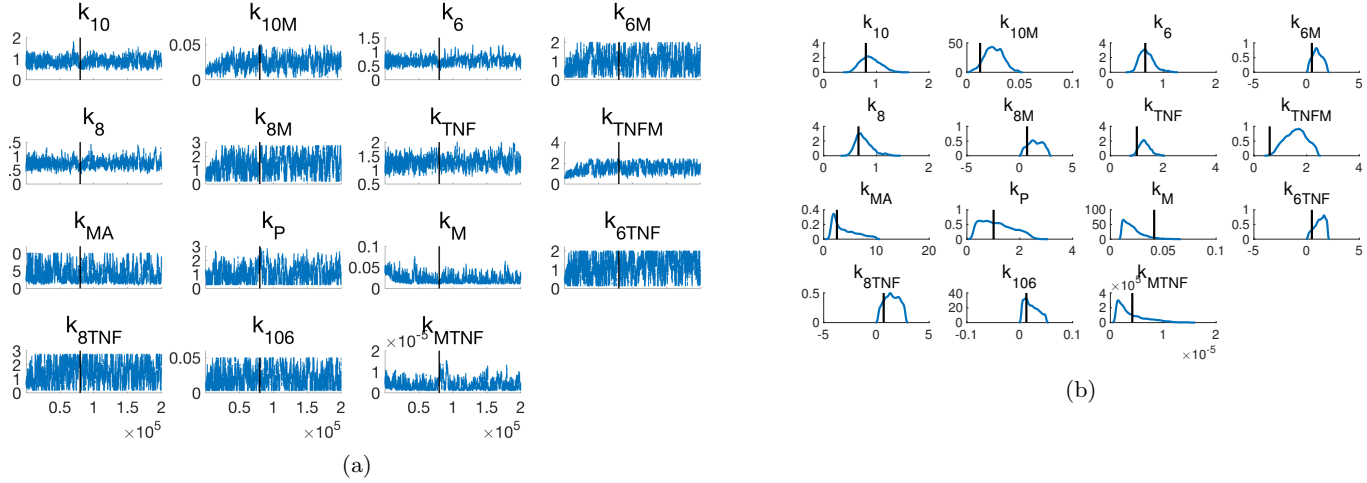
Figure 1: *DRAM results varying the 15 sensitive parameters (identified in Figure 6.1) of the inflammatory model.* (a) Parameter chains and (b) parameter distributions Simulations were done using 200,000 samples with a burn-in period of 40,000. Black line signifies in (a) end of burn-in period. Black line in (b) signifies optimal parameter values $\hat{\theta}$.

90
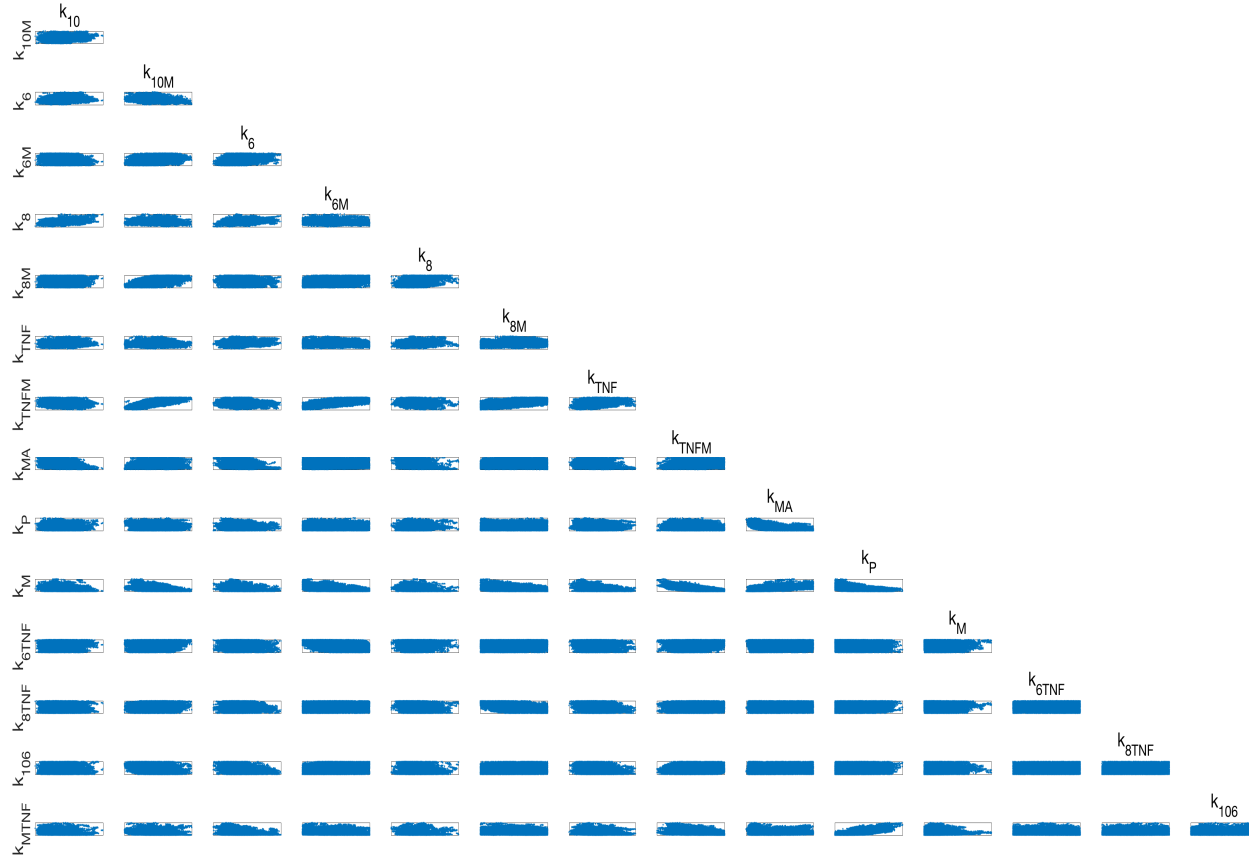
Figure 1: *DRAM parameter correlations for the 15 sensitive parameters (identified in Figure 6.1) of the inflammatory model.* Due to the unidentifiability of parameters such as k_{6TNF}, k_{8TNF}, and k_{106}, DRAM simulations are unable to identify the parameter correlations. Simulations were done using 200,000 samples.
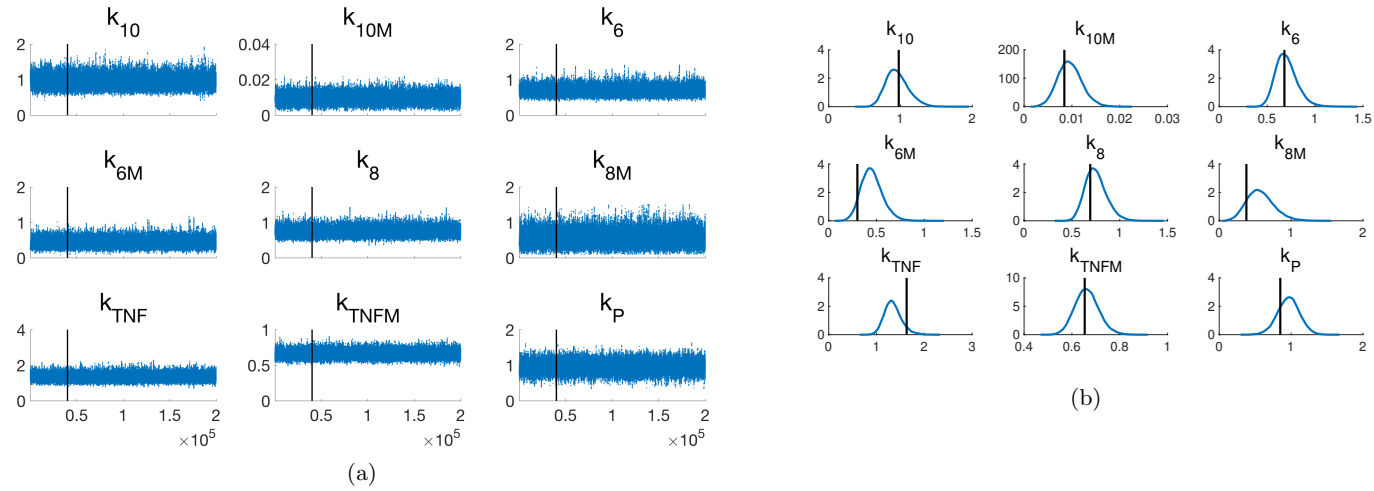
Figure 1: *DRAM results for the parameters of Subset 1.* Shows parameter (a) chains and (b) distributions. Simulations were done using 200,000 samples with a burn-in period of 40,000. Black line signifies in (a) end of burn-in period. Black line in (b) signifies optimal parameter values $\hat{\theta}$.
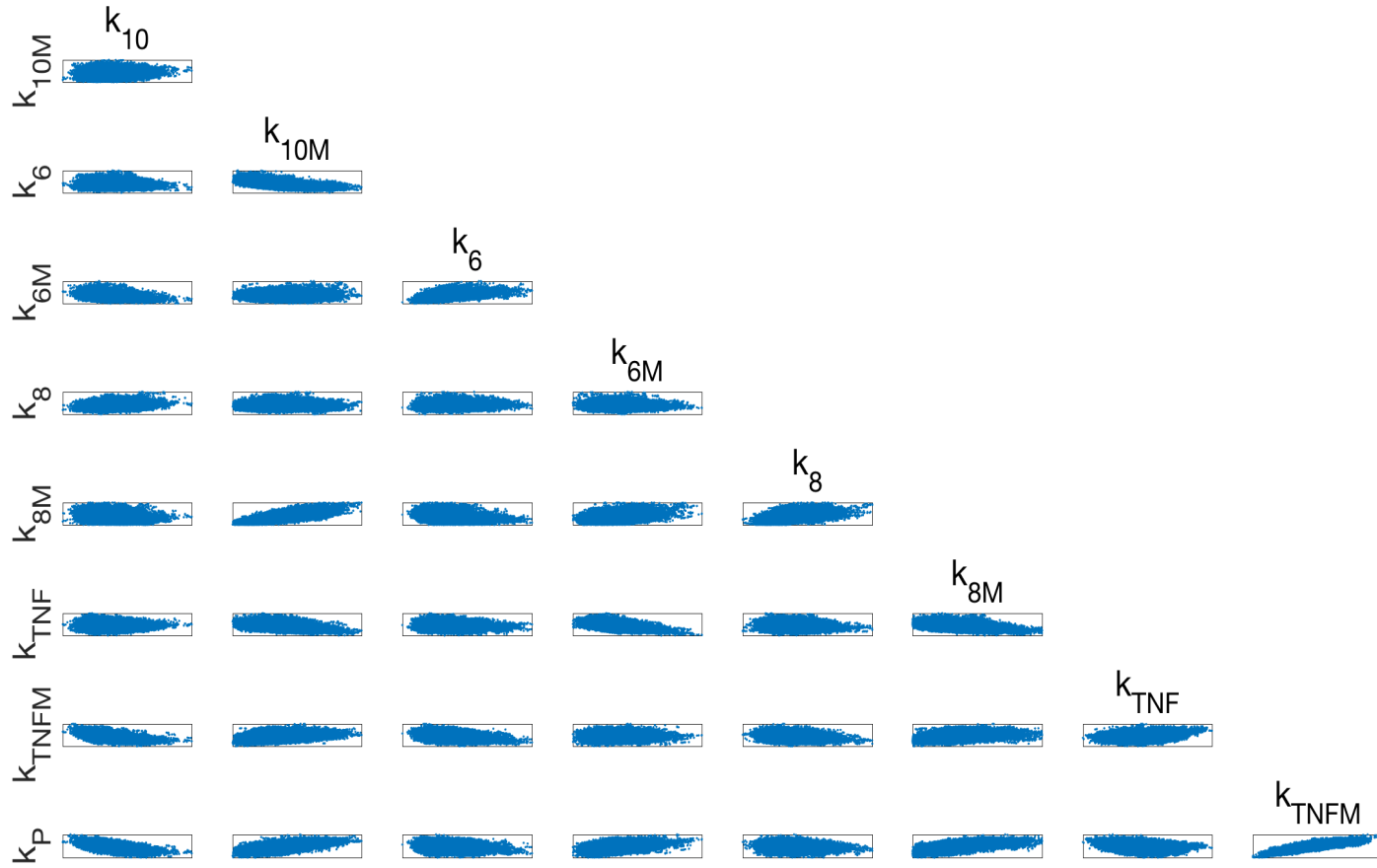
Figure 1: *DRAM parameter correlations for the Subset 1.* Parameter correlations for Subset 1 produced by DRAM. Simulations were ran 200,000 times with a burn-in period of 40,000.

in the SCM analysis.

Along with the parameter confidence intervals, shown in Table 6.3 and the prediction and confidence intervals shown in Figure 6.10, the Bayesian prediction and credible intervals were used to quantify the accuracy of the model. The prediction and credible intervals for the abnormal and normal responses (shown in Figure 6.8) are shown in Figure 6.15. The differences in the optimal parameters used to produce the model output for each of these responses is evident in the parameter chains and distributions, shown in Figure 6.16.

6.7 Discussion

In this study, a personalized model of the inflammatory response based on systemic inflammatory mediator production after a low dose intravenous endotoxin injection in healthy young men has been developed. Inter- and intra-individual variations such as those shown in Figures 6.8 and 6.9, demonstrates the importance in modeling individual dynamics. It is clear that the abnormal response is significantly different than the normal response for TNF-α, IL-10, and IL-6. This could be due to the fact that IL-6 has an inhibitory effect on TNF-α [Schulte et al., 2013; Starkie et al., 2003], so a high level of IL-6 can result in lower levels of TNF-α. Additionally, TNF-α and IL-10 have opposing roles in the inflammatory response, which can lead to a high level of IL-10 when TNF-α is low.

The variation in the responses between the two individuals can be explained by differences in the optimal parameter values. IL-6 is produced in response to the activation of the monocytes and then up-regulated by TNF-α. The parameters responsible for these interactions are k_{6M} and k_{6TNF}, respectively. The increase in k_{6M} in the abnormal response makes k_{6M} significantly higher than $k_{6TNF} H_{IL6}^{U}(\text{TNF-}\alpha)$. Thus, the majority of the IL-6 production is in response to the activated monocytes. When combined with a faster decay in the pathogen, evident by an increase in k_P, the resulting faster activation of the resting monocytes results in a higher concentration of IL-6. Due to the inhibitory effect of IL-6 on TNF-α, TNF-α decreases prematurely.

The ability of the mathematical model to predict the Day B response using the parameters optimized for Day A indicates that the model is a useful predictor of the inflammatory response in both normal and abnormal responses. It should be noted that although the experiment was performed under the same condition each day, differences among the responses may be due to
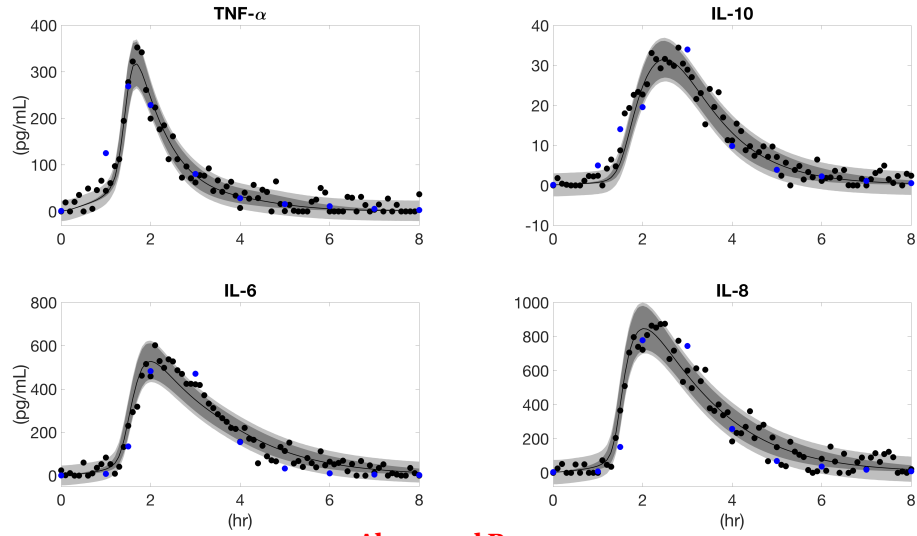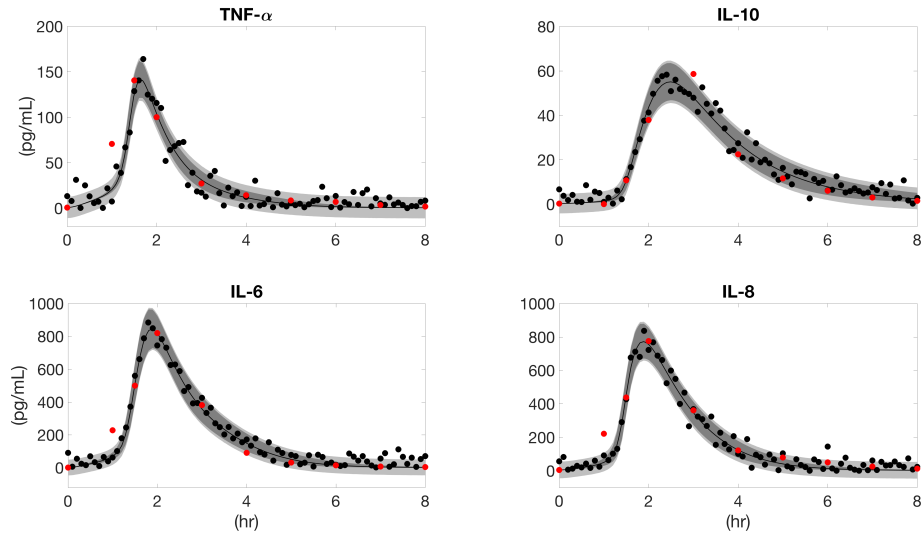
Figure 6.15 *Comparison of Bayesian prediction and credible intervals between normal and abnormal responders.* Prediction (light gray) and credible (dark gray) intervals produced by DRAM for the normal and abnormal responses in Figure 6.8. Black dots are synthetic data, while blue (red) dots are experimental data for normal (abnormal) response.

95
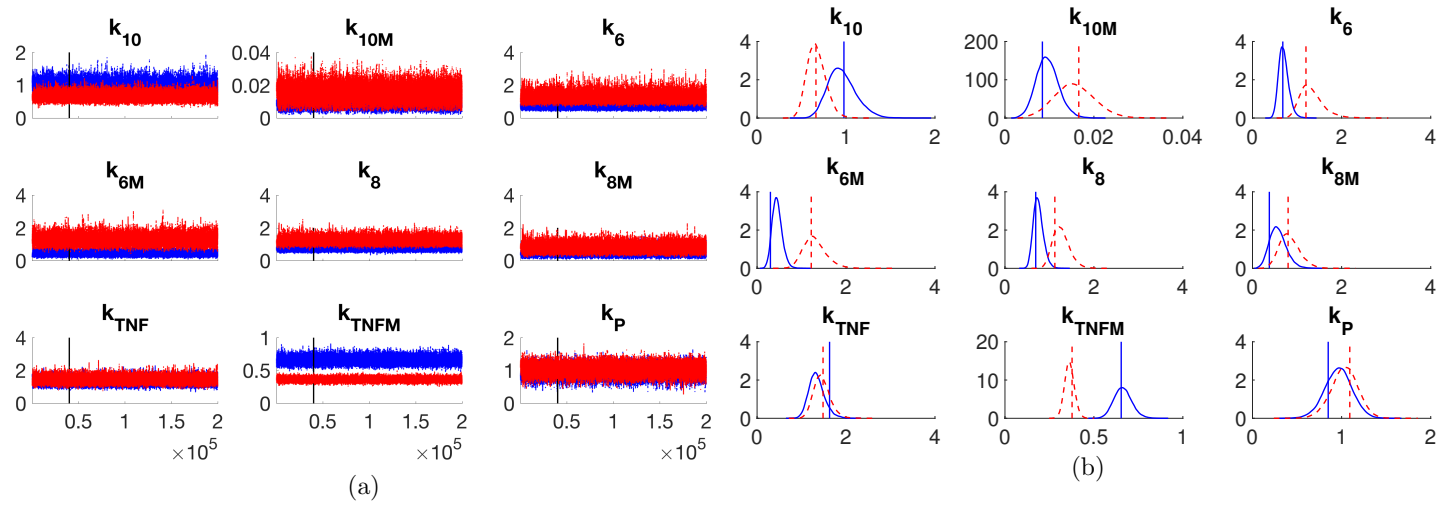
Figure 1: *Comparison of DRAM parameter chains and densities for a normal and an abnormal responder.* DRAM parameter chains (a) and parameter densities (b) for abnormal (red) and normal (b) responders, shown in Figure 6.8.

the subject developing a tolerance to the endotoxin, experiencing anxiety on the second day or preparing for the experiment differently than they did on the first day. Additionally, while responses classified as abnormal are assumed to be abnormal due to significant differences in their responses compared to the other subjects, this classification could be as a result of measurement error.

7

COUPLED CARDIOVASCULAR-INFLAMMATORY MODEL

In 2010, it was estimated that 2.5 million individuals have had a total hip replacement and that 4.7 million individuals have had a total knee replacement by the age of 80 [Maradit Kremers et al., 2015], in the U.S. alone. Current trends indicate a substantial rise in prevalence over time, with a shift towards younger people. Those who undergo knee or hip replacement surgery are encouraged to regain mobilization for a rapid and functional recovery [Guerra et al., 2015; Pearse et al., 2007]. This strategy improves outcomes, yet many patients experience orthostatic intolerance (OI), the inability to maintain blood pressure and flow in response to postural changes, when attempting to rise from bed [Cowie et al., 2004; Jans et al., 2012].

It is known that an uncontrolled, excessive production of pro-inflammatory mediators from

immune cells and traumatized tissues can cause systemic inflammatory response syndromes such as sepsis. That is, whole-body inflammation accompanied by low blood pressure [Schulte et al., 2013]. Sepsis is estimated to be one of the ten leading causes of death in the United States and one of the three leading causes of death in the intensive care unit [Fried et al., 2011]. The production of inflammatory mediators, in particular TNF-α, IL-6, and IL-1β, causes afferent neural firing to the brain, resulting in a fever [Schulte et al., 2013]. Additionally, this type of inflammatory event (i.e. endotoxin, surgery, trauma, etc.) causes a decrease in the body's pain perception threshold (PPT) [Janum et al., 2016; Zhang & An, 2007].

Copeland et al. [2005] conducted an experiment in which mice and humans were given equivalent doses of endotoxin to compare response levels of the pro-inflammatory mediators TNF-α and IL-6, as well as the anti-inflammatory mediators TNF soluble receptor I (TNF-SRI) and IL-1 receptor antagonist (IL-1RA) were measured and compared. The level of dosage was chosen to induce an IL-6 concentration in plasma of 1000 pg/mL. Results showed that the levels of TNF-α and IL-6 in plasma peaked 2h after the endotoxin injection and returned to baseline levels by 4 to 6 h. IL-1RA and TNF-SRI were upregulated in both mice and humans, but were upregulated more in humans. The study found that humans experienced a rapid physiological response, consisting of fever, tachycardia, and slight hypotension, which was not evident in mice. Thus, it was concluded that the autonomic control system is affected by the inflammatory response in humans, but likely not in mice. Tracey [2002] proposed the existence of a cholinergic anti-inflammatory pathway, which inhibits the release of inflammatory mediators from the activated monocytes via acetylcholine (ACh). That is, the brain recognizes the pathogen and sends efferent signals to the reticuloendothelial system, including the liver, spleen, heart, and gastrointestinal tract. This leads to ACh release, which inhibits the production of pro-inflammatory mediators via an ACh receptor on the activated monocytes. The increased efferent activity along the vagus nerve also increases heart rate variability.

These findings show that the cardiovascular system has an effect on the inflammatory response and conversely, the inflammatory response has an effect on the dynamics of the cardiovascular system. In this chapter, we focus on the effect of inflammation on the cardiovascular system dynamics in response to endotoxin. We hypothesize that the heart rate increase, observed in humans and not in mice, is caused by the increase in the temperature set point, while the rise in blood pressure is caused by the decrease in pain perception tolerance (PPT). This effect is

combated by a decrease in pressure caused by the vasodilator nitric oxide (NO) several hours later. These interactions are summarized in Figure 7.4 on page 115. To date, the pathway from the inflammatory response to changes in cardiovascular dynamics has not been well-defined and to our knowledge, we are the first to set forth a pathway of this sort. Clearly defining the effect of inflammation on the cardiovascular dynamics, through the analysis of specific biomarkers, can aid in the development of preoperative therapy to prevent sepsis propagation.

This chapter begins with a brief review of the inflammatory model in Section 7.1, followed by a description of the cardiovascular model in Section 7.2. Using the effectors NO, temperature, and pain perception, the cardiovascular model is coupled with the inflammatory model. This is discussed in Section 7.3. Finally, the parameterization is explained in Section 7.4.

7.1 Inflammatory Model

Recall from Chapter 5 that the inflammatory response to endotoxin activates the monocytes, which produce the inflammatory mediators that mediate the response. In particular, the pro-inflammatory mediators TNF-α, IL-6, and IL-8 increase the levels of inflammation, while the anti-inflammatory mediator IL-10 regulates the response by reducing the inflammation. Each component of the response works with the other to restore homeostasis to the system. Once the pathogen is cleared, the response subsides and the mediators return to their basal levels.

7.2 Cardiovascular Model

The cardiovascular dynamics determining heart rate and blood pressure are typically analyzed using either multi-dimensional models, describing fluid dynamics as functions of space and time or system-level models lumping vessels into compartments. Multi-dimensional models are useful when determining local behavior in a specific part of the circulation, such as the flow through a bypass configuration. In contrast, system-level models lump several regions of the body into compartments and the flow between these are predicted using an analogue to RC-electrical circuits. In this model type, blood pressure is equivalent to voltage, flow is equivalent to current, volume is equivalent to charge, capacitance is equivalent to compliance, while resistance is the same in both formulations. Multidimensional models are almost always pulsatile, while system-level models

can be either pulsatile or non-pulsatile.

Pulsatile compartmental models account for the dynamics within heart beats, therefore producing beat-to-beat changes in arterial blood pressure. In such models, the pumping of the heart is typically represented by a time-varying elastance function [Heldt et al., 2002; Mukkamala & Cohen, 2001; Olufsen et al., 2005; Ursino, 1998]. In contrast, non-pulsatile models predict the average behavior (i.e. mean blood pressure, flow, and volume) by integrating the effect of the heart [Batzel et al., 2007; Kappel & Peer, 1993]. One of the advantages of non-pulsatile models is that they are less complex, allowing for easier coupling with more advanced models, since the opening and closing of the heart valves is not being accounted for. In this study, the inflammatory model is analyzed over 8 hours and it is more computationally efficient to couple this model with a non-pulsatile model as computations are significantly faster than with a pulsatile model. Furthermore, on this timescale, we are not interested in beat-to-beat behavior.

Numerous researchers have used system-level models to investigate events within the cardiac cycle. Ursino [1998] developed an eight-compartmental pulsatile mathematical model to study the pulsating heart and its interactions with the carotid baroreflex control system. This model included both the pulmonary and systemic circulation. To account for the pulsatility of the heart, the resistance in the left ventricle was modeled as a linear function of the isometric left ventricle pressure. Olufsen et al. [2005] developed an 11-compartmental model predicting dynamic changes in beat-to-beat arterial blood pressure during a postural change from sitting to standing. Unlike the model by Ursino, this model focused solely on the systemic circulation. The resistances in the left ventricle were modeled as pressure-dependent exponential functions and the resistances in the large systemic arteries were modeled using nonlinear functions of pressure.

Mukkamala & Cohen [2001] developed a six-compartmental pulsatile model for the analysis of beat-to-beat fluctuations in non-invasively measured heart rate, blood pressure, and instantaneous lung volume. The model included compartments for the systemic and pulmonary veins and arteries, as well as the left and right ventricles. The aim of this study was to validate a previously developed cardiovascular system identification method [Mukkamala, 2000]. This identification method mathematically analyzed hemodynamic signals to provide a dynamical characterization of the physiological mechanisms responsible for generating them. Heldt et al. [2002] developed a ten-compartmental pulsatile model of the short-term transient and steady-state hemodynamic responses to head-up tilt and lower body negative pressure. This was a closed-loop lumped-

parameter model of the systemic and pulmonary circulations connected to set-point model of the arterial and cardiopulmonary baroreflexes.

The cardiovascular model described in this chapter is adapted from the pulsatile model by Williams et al. [2013]. Similar to the model by Olufsen et al. [2005], the resistors of the heart valves are modeled as time-varying functions of the pressure. Additionally, an elastance function, initially proposed by Ellwein [2008], is used to model the pumping of the heart. As previously mentioned, it is advantageous to use a non-pulsatile model to analyze dynamics over longer time-scales (minutes-hours). Thus, from the pulsatile model, a non-pulsatile model is developed that can predict blood pressure and heart rate. This non-pulsatile model is interchangeable with the pulsatile model since it is obtained by integrating the pulsatile model, using the same parameters. We start by describing the pulsatile model and then showing how to convert it to the non-pulsatile model by eliminating the left heart compartment, as shown in Figure 7.1b.

7.2.1 Pulsatile Cardiovascular Model

The cardiovascular model, shown in Figure 7.1, predicts flow (q), pressure (p), and volume (V) in the systemic circulation. The compartmental model contains two arterial and two venous compartments representing the arteries and veins in the upper body and organs beds.

By the conservation of volume, the change in volume in compartment i is given by

$$\frac{dV_i}{dt} = q_{in} - q_{out}, \tag{7.1}$$

where q_{in} and q_{out} denote the volumetric flow coming in and going out of the compartment, respectively. Using Ohm's Law, flow can be predicted as

$$q = \frac{p_{in} - p_{out}}{R}, \tag{7.2}$$

where p_{in} and p_{out} are the pressures on either side of the resistor R.

For each compartment, the pressure and volume are related by

$$V_i - V_{un} = C_i(p_i - p_{ext}), \tag{7.3}$$
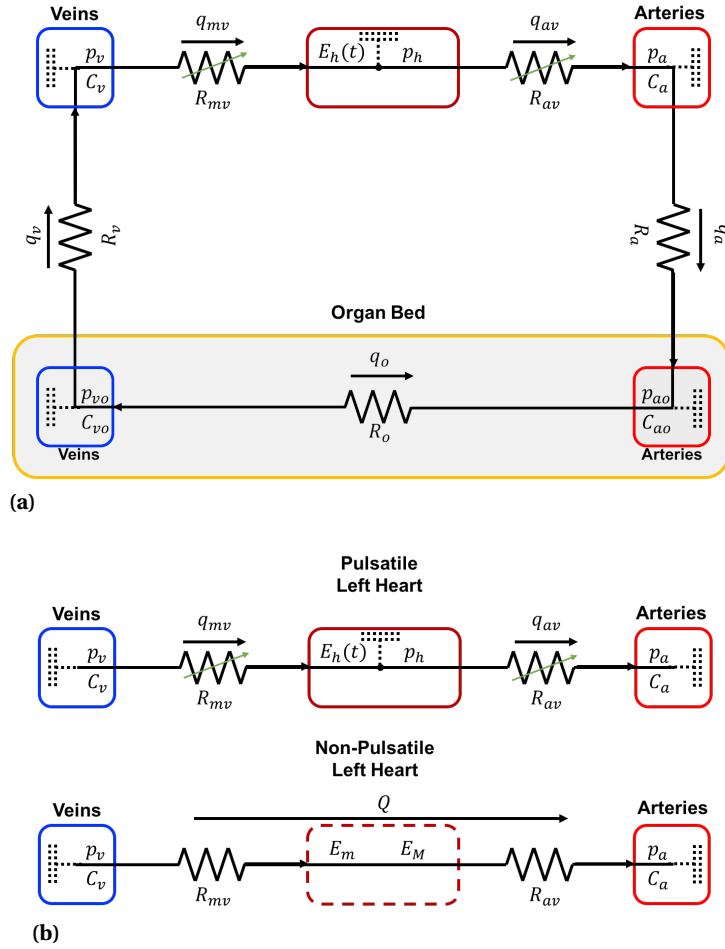
Figure 7.1 *Compartmental model predicting cardiovascular dynamics.* (a) Each compartment has an associated blood pressure p (mmHg), volume V (mL), and compliance C (mL/mmHg). The compartments represent the systemic arteries, arteries in the organ bed, veins in the organ bed, veins, and the left heart (subscripts a, ao, vo, v, and h, respectively). Resistances R (mmHg s/mL) are placed between all compartments. q_{av} and q_{mv} represent the aortic and mitral valves, respectively. (b) Note that the left heart compartment is omitted in the non-pulsatile model.

103

where V_{un} is the unstressed volume, C_i is the compliance, p_i is the instantaneous blood pressure, and p_{ext} is the pressure in the surrounding tissue. For the left heart, pressure is predicted using the pressure-volume relation

$$p_h = E_h(t)(V_h - V_{\text{un}}),\tag{7.4}$$

where V_h is the left heart volume and $E_h(t)$ is the time-varying elastance of the left heart (the reciprocal of its compliance), given by

$$E_h(t) = \begin{cases} \dfrac{E_M - E_m}{2}\left[1 - \cos\left(\dfrac{\pi\tilde{t}}{T_S}\right)\right] + E_m, & 0 \le \tilde{t} \le T_S, \\[2ex] \dfrac{E_M - E_m}{2}\left[\cos\left(\dfrac{\pi(\tilde{t} - T_S)}{T_R - T_S}\right) + 1\right] + E_m, & T_S \le \tilde{t} \le T_R, \\[2ex] E_m, & T_R \le \tilde{t} \le T, \end{cases}$$

where $\tilde{t}$ is the time within a cardiac cycle $T = 1/H$ [Ellwein, 2008]. The minimum and maximum elastances are represented by E_m and E_M, respectively. For each cardiac cycle, elastance is increased during systole for $0 < \tilde{t} < T_S$. During diastole, elastance is decreased for $T_S < \tilde{t} < T_R$ and kept constant at its minimum value E_m for the remainder of the cardiac cycle. The elastance function is shown in Figure 7.2.

The volume in each compartment, shown in Figure 7.1a, are obtained by solving the differential equations

$$\begin{aligned} \frac{dV_v}{dt} &= q_v - q_{mv}, & \frac{dV_{ao}}{dt} &= q_a - q_o, \\[1ex] \frac{dV_{vo}}{dt} &= q_o - q_v, & \frac{dV_h}{dt} &= q_{mv} - q_{av}, \\[1ex] \frac{dV_a}{dt} &= q_{av} - q_a, \end{aligned}\tag{7.5}$$

where

$$q_a = \frac{p_a - p_{ao}}{R_a}, \qquad q_o = \frac{p_{ao} - p_{vo}}{R_o}, \qquad q_v = \frac{p_{vo} - p_v}{R_v}.\tag{7.6}$$

The flows through the aortic and mitral valves (q_{av} and q_{mv}, respectively) each depend on the difference between the pressure within the heart and the arterial and venous pressures. If the pressure in the heart is less than the arterial pressure, then $q_{av} = 0$. This is the case from the beginning of the cardiac cycle until the end of the isovolumic contraction and between T_S and
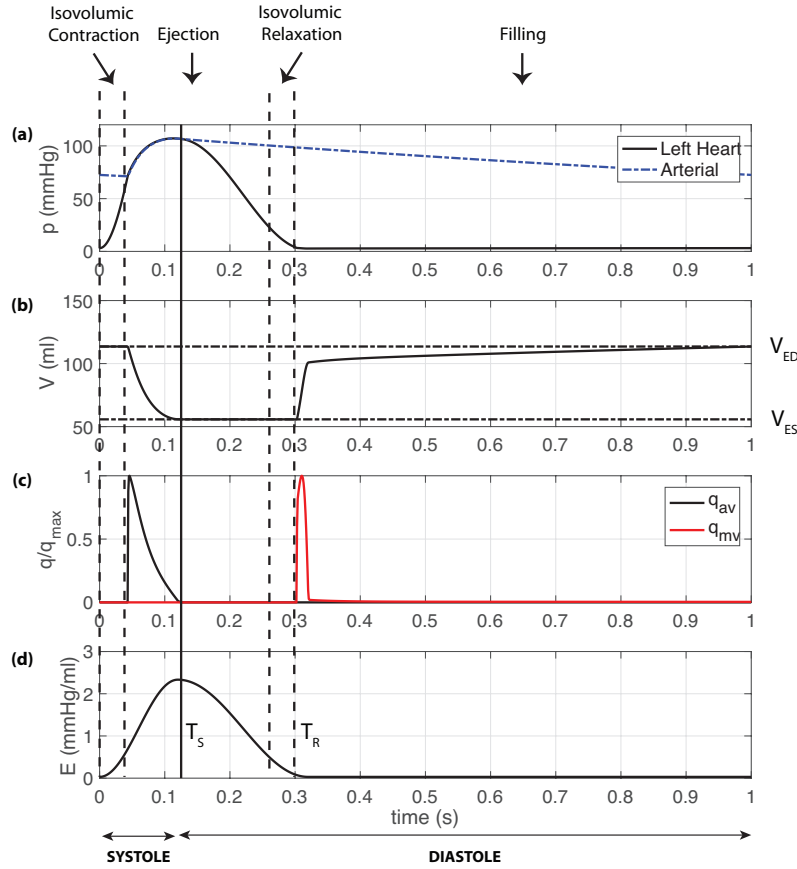
Figure 7.2 *Pressure, volume, flow, and elastance changes during the systolic and diastolic phases of the cardiac cycle.* (a) Left ventricular (black) and arterial (blue dashed) pressures. (b) Left ventricular volume. The horizontal dashed lines represent end-diastolic (V_{ED}) and end-systolic (V_{ES}) volumes. (c) Relative flows q_{av} and q_{mv}. (d) Time-varying elastance during a cardiac cycle. The maximum elastance is found at $\tilde{t} = T_S$ and the minimal elastance at $\tilde{t} = T_R$, while the length of the cardiac cycle is assumed to be $T = 1s$. Adapted from [Smith & Kampine, 1990].

T. This is evident in the pressure and relative aortic flow throughout the cardiac cycle shown in Figure 7.2. If the pressure in the heart is greater than the venous pressure, then $q_{mv} = 0$. The relative flow through the mitral valve is shown by the red line in Figure 7.2c.

These relations are represented by the piecewise functions

$$q_{av} = \begin{cases} \dfrac{p_h - p_a}{R_{av}}, & \text{when } p_h > p_a \\ 0, & \text{otherwise} \end{cases} \quad \text{and} \quad q_{mv} = \begin{cases} \dfrac{p_v - p_h}{R_{av}}, & \text{when } p_h < p_v \\ 0, & \text{otherwise.} \end{cases}$$

Differentiating 7.3, yields

$$\frac{dV_i}{dt} = C_i \frac{dp_i}{dt} \quad \Longrightarrow \quad \frac{dp_i}{dt} = \frac{1}{C_i} \frac{dV_i}{dt}.$$

Thus, the pressure in each compartment is given by the solution to

$$\begin{aligned} \frac{dp_v}{dt} &= \frac{q_v - q_{mv}}{C_v}, & \frac{dp_a}{dt} &= \frac{q_{av} - q_a}{C_a}, \\ \frac{dp_{vo}}{dt} &= \frac{q_o - q_v}{C_{vo}}, & \frac{dp_{ao}}{dt} &= \frac{q_a - q_o}{C_{ao}} \end{aligned} \tag{7.7}$$

and the pressure in the heart is given by (7.4).

7.2.2 Non-Pulsatile Cardiovascular Model

The inclusion of an elastance function, representing the pumping of the heart, makes the model described above pulsatile. The left heart compartment can be eliminated by integrating the current model over the cardiac cycle, creating a non-pulsatile cardiovascular model, without introducing additional model parameters. To date, this has not been done in previous cardiovascular studies.

The volume in the ventricular compartment is given by solving

$$\frac{dV_h}{dt} = q_{mv} - q_{av},$$

where during filling (from T_R to T) the mitral valve is open and the aortic valve is closed. Thus,

$$\frac{dV_h}{dt} = q_{mv} = \begin{cases} \dfrac{p_v - p_h}{R_{mv}}, & \text{when } p_v > p_h \\ 0, & \text{otherwise.} \end{cases}$$

106

To eliminate the left ventricle compartment, during filling we let the average flow through the heart, Q, be defined as

$$Q = \overline{q}_{mv} = \frac{1}{T}\int_0^T \frac{dV_h}{dt}\,dt \approx \frac{1}{T}\int_{T_R}^T \frac{dV_h}{dt}\,dt,$$

where $\overline{q}_{mv}$ represents the average flow through the mitral valve. From Figure 7.2c, it is clear that the mitral valve is closed for $0 < \tilde{t} < T_R$ ($q_{mv} = 0$). Thus, the latter integral holds and integration gives

$$
\begin{aligned}
Q &\approx \frac{1}{T}\int_{T_R}^T \frac{dV_h}{dt}\,dt \\
&= \frac{1}{T}\Big[V_h(T) - V_h(T_R)\Big] \\
&= \frac{1}{T}\Big[V_{ED} - V_{ES}\Big],
\end{aligned}
$$

where V_{ED} and V_{ES} are the end-diastolic and end-systolic volumes, respectively. During ejection, the aortic valve is open while the mitral valve is closed so

$$\frac{dV_h}{dt} = -q_{av} = \begin{cases} -\dfrac{p_h - p_a}{R_{mv}}, & \text{when } p_h > p_a \\ 0, & \text{otherwise.} \end{cases}$$

Again, let the average flow through the heart be defined as Q, giving

$$Q = \overline{q}_{av} = -\frac{1}{T}\int_0^T \frac{dV_h}{dt}\,dt.$$

Note that during ejection, the volume in the left ventricle is decreasing, indicated by the minus in front of the integral. As shown in Figure 7.2, the heart ejects blood from the end of the isovolumic contraction to the beginning of the isovolumic relaxation. Since the volume is not changing during the isovolumic contraction, nor from the end of systole ($t = T_S$) to the beginning of filling ($t = T_R$),

we can estimate the average flow during ejection as the change in flow from $t = 0$ to $t = T_S$ as

$$
\begin{aligned}
Q &\approx -\frac{1}{T} \int_0^{T_S} \frac{dV_h}{dt} dt \\
&= -\frac{1}{T} \Big[V_h(T_S) - V_h(0) \Big] \\
&= \frac{1}{T} \Big[V_{ED} - V_{ES} \Big].
\end{aligned}
$$

Keeping in mind that $H = 1/T$ and defining the stroke volume as

$$
V_{\text{str}} = V_{ED} - V_{ES}, \tag{7.8}
$$

then the cardiac output can be defined as

$$
Q \approx H V_{\text{str}}.
$$

Note that the heart rate can be given as an input to the model or given by a control function (discussed in Section 7.3.2). The final step of the model development is to solve for V_{ED} and V_{ES} in terms of the model parameters. This is achieved via integration.

Solving for V_{ED} During Filling

During filling, the flow entering the left ventricle is given by

$$
q_{mv} = \frac{p_v - p_h}{R_{mv}},
$$

so that

$$
\dot{V}_h = q_{mv} - \cancel{q_{av}} = \frac{p_v - p_h}{R_{mv}}. \tag{7.9}
$$

Inserting (7.4) in (7.9) gives

$$
\dot{V}_h = \frac{1}{R_{mv}} (p_v - E_h(V_h - V_{un})) \Longleftrightarrow
$$

$$
\dot{V}_h + \frac{E_h}{R_{mv}} V_h = \frac{p_v + E_h V_{un}}{R_{mv}}.
$$

We can assume that the venous pressure p_v is constant since it does not oscillate much during filling; that is, $p_v = \overline{p}_v$. Additionally, we can assume that $E_h(t) = E_m$, so that integration yields

$$\mu(t) = \int \frac{E_m}{R_{mv}}\,\mathrm{d}t = \frac{E_m}{R_{mv}}t \quad \text{(Integrating Factor)}$$

$$
\begin{aligned}
\Longrightarrow e^{E_m t/R_{mv}}\,V_{lh} &= \int e^{E_m t/R_{mv}}\Big(\frac{\overline{p}_v + E_m V_{un}}{R_{mv}}\Big)\mathrm{d}t \\
&= e^{E_m t/R_{mv}}\Big(\frac{\overline{p}_v + E_m V_{un}}{\cancel{R_{mv}}}\Big)\Big(\frac{\cancel{R_{mv}}}{E_h}\Big) + C \\
&= e^{E_m t/R_{mv}}\Big(\frac{\overline{p}_v}{E_m} + V_{un}\Big) + C. \\
\Longrightarrow V_h &= \frac{\overline{p}_v}{E_m} + V_{un} + C e^{-E_m t/R_{mv}}.
\end{aligned}
\tag{7.10}
$$

Assuming $V_h(0) = V_{ES}$ (volume at the beginning of filling, i.e. minimum volume), (7.10) becomes

$$
\begin{aligned}
V_{ES} &= \frac{\overline{p}_v}{E_m} + V_{un} + C e^{-E_m \cdot 0/R_{mv}} \\
\Longrightarrow C &= V_{ES} - \frac{\overline{p}_v}{E_m} - V_{un} \\
\Longrightarrow V_h &= V_{ES}e^{-E_m t/R_{mv}} + \Big(\frac{\overline{p}_v}{E_m} + V_{un}\Big)\Big(1 - e^{-E_m t/R_{mv}}\Big).
\end{aligned}
$$

Evaluating this at end-diastolic volume $V = V_{ED}$ gives

$$V_{ED} = V_{ES}e^{-E_m T_D/R_{mv}} + \Big(\frac{\overline{p}_v}{E_m} + V_{un}\Big)\Big(1 - e^{-E_m T_D/R_{mv}}\Big), \tag{7.11}$$

where $T_D = T - T_R$ and T_R is the time to fill, as shown in Figure 7.2.

Solving for V_{ES} During Ejection

During ejection, the flow entering the left ventricle is given by

$$q_{av} = \frac{p_h - p_a}{R_{av}},$$

so that

$$\dot{V}_h = \cancel{q_{mv}} - q_{av} = -\frac{p_h - p_a}{R_{av}}. \tag{7.12}$$

Inserting (7.4) in (7.12) gives

$$\dot{V}_h = -\frac{1}{R_{av}}(E_h(V_h - V_{un}) - p_a) \Longleftrightarrow$$

$$\dot{V}_h + \frac{E_h}{R_{av}} V_h = \frac{E_h V_{un} + p_a}{R_{av}}.$$

Assuming the arterial pressure p_a is constant ($p_a = \overline{p}_a$) and $E_h(t) = E_M$, integrating yields

$$
\begin{aligned}
e^{E_M t / R_{av}} V_{lh} &= \int e^{E_M t / R_{av}} \left(\frac{E_M V_{un} + \overline{p}_a}{R_{av}} \right) \mathrm{d}t \\
&= e^{E_M t / R_{av}} \left(V_{un} + \frac{\overline{p}_a}{E_M} \right) + C \\
\Longrightarrow V_h &= \frac{\overline{p}_a}{E_M} + V_{un} + C e^{-E_M t / R_{av}}.
\end{aligned}
\tag{7.13}
$$

Note that the assumption that p_a is constant is a weaker assumption than the one on the venous side. However, it is necessary in order to evaluate the integral. Arterial pressure might be able to be approximated with a sinusodail function of the systolic and diastolic pressures.

Assuming $V_h(0) = V_{ED}$, (7.13) becomes

$$
\begin{aligned}
V_{ED} &= \frac{\overline{p}_a}{E_M} + V_{un} + C \\
\Longrightarrow C &= V_{ED} - \frac{\overline{p}_a}{E_M} - V_{un} \\
\Longrightarrow V_h &= e^{-E_M t / R_{av}} V_{ED} + \left(\frac{\overline{p}_a}{E_M} + V_{un} \right) \left(1 - e^{-E_M t / R_{av}} \right).
\end{aligned}
$$

Evaluating this equation at end-systolic volume $V = V_{ES}$ gives

$$V_{ES} = e^{-E_M T_R/R_{av}} V_{ED} + \Big(\frac{\overline{p}_a}{E_M} + V_{un}\Big)\Big(1 - e^{-E_M T_M/R_{av}}\Big) \tag{7.14}$$

where T_R is the time at end-systole.

Stroke Volume

Recall from (7.15) that

$$V_{str} = V_{ED} - V_{ES}.$$

Letting

$$k_1 = e^{-E_M T_R/R_{av}} \quad \text{and} \quad k_2 = e^{-E_m T_D/R_{mv}},$$

then from (7.11 and (7.14), we have

$$
\begin{aligned}
V_{ED} &= V_{ES} k_2 + \Big(\frac{\overline{p}_v}{E_m} + V_{un}\Big)\Big(1 - k_2\Big) \\
V_{ES} &= V_{ED} k_1 + \Big(\frac{\overline{p}_a}{E_M} + V_{un}\Big)\Big(1 - k_1\Big).
\end{aligned}
$$

Multiplying the second equation by k_2 and substituting in the first equation gives

$$
\begin{aligned}
V_{ES} k_2 &= V_{ED} k_1 k_2 + \Big(\frac{\overline{p}_a}{E_M} + V_{un}\Big)\Big(1 - k_1\Big) k_2 \\
\implies V_{ED} &= V_{ED} k_1 k_2 + \Big(\frac{\overline{p}_a}{E_M} + V_{un}\Big)\Big(1 - k_1\Big) k_2 + \Big(\frac{\overline{p}_v}{E_m} + V_{un}\Big)\Big(1 - k_2\Big) \\
\implies V_{ED}(1 - k_1 k_2) &= \Big(\frac{\overline{p}_a}{E_M} + V_{un}\Big)\Big(1 - k_1\Big) k_2 + \Big(\frac{\overline{p}_v}{E_m} + V_{un}\Big)\Big(1 - k_2\Big) \\
\implies V_{ED} &= \Big(\frac{\overline{p}_a}{E_M} + V_{un}\Big)\frac{(1 - k_1)k_2}{(1 - k_1 k_2)} + \Big(\frac{\overline{p}_v}{E_m} + V_{un}\Big)\frac{(1 - k_2)}{(1 - k_1 k_2)}.
\end{aligned}
$$

Similarly for V_{ES},

$$V_{ED}\,k_1 \;=\; V_{ES}\,k_1 k_2 + \Big(\frac{\overline{p}_v}{E_m} + V_{un}\Big)\big(1-k_2\big)k_1$$

$$\Longrightarrow V_{ES} \;=\; V_{ES}\,k_1 k_2 + \Big(\frac{\overline{p}_v}{E_m} + V_{un}\Big)\big(1-k_2\big)k_1 + \Big(\frac{\overline{p}_a}{E_M} + V_{un}\Big)\big(1-k_1\big)$$

$$\Longrightarrow V_{ES}(1-k_1 k_2) \;=\; \Big(\frac{\overline{p}_v}{E_m} + V_{un}\Big)\big(1-k_2\big)k_1 + \Big(\frac{\overline{p}_a}{E_M} + V_{un}\Big)\big(1-k_1\big)$$

$$\Longrightarrow V_{ES} \;=\; \Big(\frac{\overline{p}_v}{E_m} + V_{un}\Big)\frac{(1-k_2)k_1}{(1-k_1 k_2)} + \Big(\frac{\overline{p}_a}{E_M} + V_{un}\Big)\frac{(1-k_1)}{(1-k_1 k_2)}.$$

This gives

$$
\begin{aligned}
V_{\text{str}} \;&=\; V_{ED} - V_{ES}\\
&=\; \Big(\frac{\overline{p}_a}{E_M} + V_{un}\Big)\frac{(1-k_1)k_2}{(1-k_1 k_2)} + \Big(\frac{\overline{p}_v}{E_m} + V_{un}\Big)\frac{(1-k_2)}{(1-k_1 k_2)}\\
&\quad -\Big(\frac{\overline{p}_v}{E_m} + V_{un}\Big)\frac{(1-k_2)k_1}{(1-k_1 k_2)} - \Big(\frac{\overline{p}_a}{E_M} + V_{un}\Big)\frac{(1-k_1)}{(1-k_1 k_2)}\\
&=\; \Big(\frac{\overline{p}_a}{E_M} + V_{un}\Big)\Big[\frac{-1+k_1+k_2-k_1 k_2}{1-k_1 k_2}\Big] - \Big(\frac{\overline{p}_v}{E_m} + V_{un}\Big)\Big[\frac{-1+k_1+k_2-k_1 k_2}{1-k_1 k_2}\Big]\\
&=\; \Big(\frac{-1+k_1+k_2-k_1 k_2}{1-k_1 k_2}\Big)\Big(\frac{\overline{p}_a}{E_M} + \cancel{V_{un}} - \frac{\overline{p}_v}{E_m} - \cancel{V_{un}}\Big)\\
&=\; \Big(\frac{-1+k_1+k_2-k_1 k_2}{1-k_1 k_2}\Big)\Big(\frac{\overline{p}_a}{E_M} - \frac{\overline{p}_v}{E_m}\Big).
\end{aligned}
$$

Note that since the exponentials k_1 and k_2 are close to 0 (since the resistances R_{av} and R_{mv} are small), the stroke volume can be approximated by

$$V_{\text{str}} = -\Big(\frac{\overline{p}_a}{E_M} - \frac{\overline{p}_v}{E_m}\Big). \tag{7.15}$$

Simulations shown in Figure 7.3 comparing the averaged pulsatile pressure (cyan) and the non-pulsatile pressure (red dashed) show that the two pressures agree.
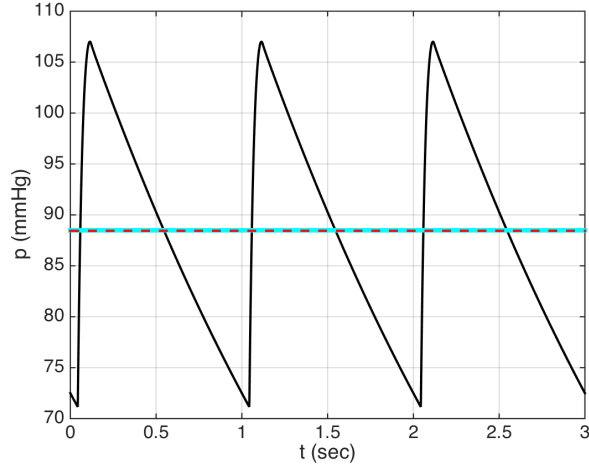
Figure 7.3 *Predictions of arterial pressure p_a, using the pulsatile and non-pulsatile.* Pulsatile pressure is shown by black line, while non-pulsatile pressure is shown by the cyan line.

7.2.3 Non-pulsatile Model

Using (7.15), the non-pulsatile dynamics described in Figure 7.1b can be expressed as

$$
\begin{aligned}
\frac{dV_v}{dt} &= q_v - Q, & \frac{dV_a}{dt} &= Q - q_a, \\
\frac{dV_{vo}}{dt} &= q_o - q_v, & \frac{dV_{ao}}{dt} &= q_a - q_o,
\end{aligned}
\tag{7.16}
$$

where the flows q are defined in (7.5) and

$$
Q = H V_{\text{str}}.
$$

7.3 Coupled Model

In response to inflammation, pro-inflammatory mediators, in particular IL-1β, TNF-α, and IL-6, communicate with the brain via neural firing. This initiates the brain-mediated components of

113

host defense, such as fever [Hansen et al., 2001; Netea et al., 2000]. This change in the temperature set point decreases the vagal firing, leading to an increase in heart rate (HR). The increased production of nitric oxide (NO) by the inflammatory mediators results in a decrease in resistance and contractility and an increase in compliance, due to its function as a vasodilator, causing blood pressure (BP) to decrease [Chowdhary et al., 2000]. This decrease in sympathetic activity sustains the increase in heart rate, initially induced by the increase in temperature. Experimental data shows that the onset of inflammation also causes a decrease in the pain perception threshold (PPT), causing an increase in sympathetic activity [Schobel et al., 1996]. This forces resistance to increase, in turn increasing BP. The interactions between the cardiovascular system and the inflammatory response, in particular the effect of the inflammatory response on HR and BP, are illustrated in Figure 7.4.

7.3.1   Temperature

Fever is one of the most frequent physiological adaptions as a result of infection. It is initiated to stagnate the growth of bacteria, as most bacteria are unable to proliferate at temperatures above 39° C [Netea et al., 2000]. When a pathogen/bacteria enters the body, monocytes and leukocytes stimulate the release of endogenous pyrogens (EP). These EPs, recently identified as pro-inflammatory mediators such as IL-1β, TNF-α, and IL-6, reach the central nervous system (CNS), where they induce the production of prostaglandins. Through this process, they are able to increase the temperature set point and cause a fever. IL-10 acts as an endogenous antipyretic, reducing the fever [Conti et al., 2004; Pajkrt et al., 1997a].

The effect of the EPs, TNF-α and IL-6, and the anti-pyretic IL-10 on temperature is modeled by

$$\frac{d\,\text{Temp}}{d\,t} = \frac{-\text{Temp} + F(\text{TNF, IL6, IL10})}{\tau_1}, \tag{7.17}$$

where

$$
\begin{aligned}
F(\text{TNF, IL6, IL10}) \;=\; & k_T(T_M - T_m)\Big(k_{T\text{TNF}}H_T^U(\text{TNF} - q_{\text{TNF}}) + k_{T6}H_T^U(\text{IL6} - q_{\text{IL6}}) \\
& -k_{T10}(1 - H_T^D(\text{IL10} - q_{\text{IL10}}))\Big) + T_m,
\end{aligned}
$$

and τ_1, $k_{T\text{TNF}}$, k_{T6}, k_{T10}, and k_T are rate constants. T_m is the baseline temperature and T_M is the

114
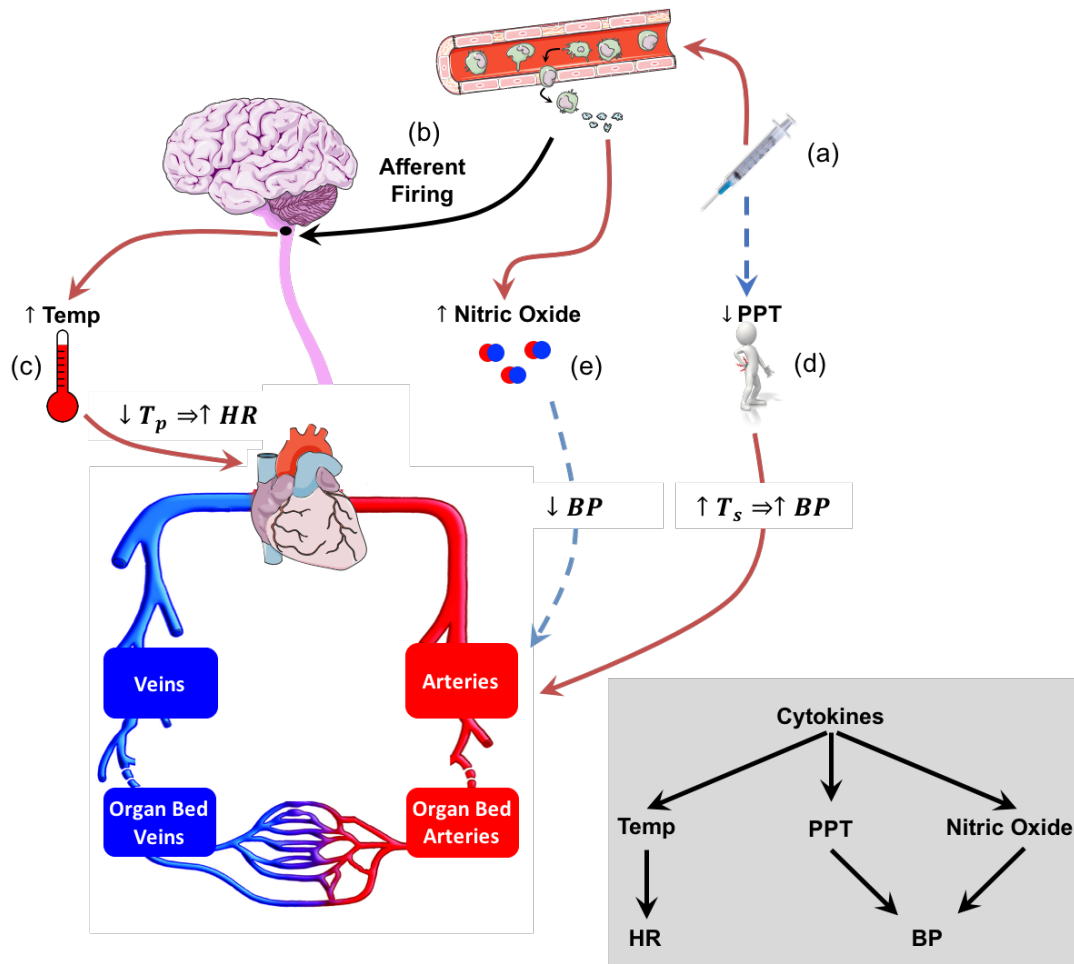
Figure 7.4 *Effect of inflammation on cardiovascular dynamics.* (a) Endotoxin causes release of inflammatory mediators and reduction of pain perception threshold (PPT). (b) Afferent firing in the brain, as a result of IL-1β, TNF-α, and IL-6 increases temperature. (c) In response to the fever, a decrease in vagal activity (T_p) causes an increase in HR. (d) PPT reduction increases sympathetic activity (T_s), which increases blood pressure. (e) Between 2-4 hours after the administration of endotoxin, nitric oxide is released, decreasing BP.

maximum temperature. Note that the Hill functions are functions of each mediator minus its basal level (the amount of mediator in the absence of the endotoxin). This form is used to ensure that temperature stays constant before the administration of endotoxin.

7.3.2 Heart Rate

In addition to causing a fever, the activity in the CNS also decreases the vagal firing, causing an increase in heart rate. Clinical findings show a dose-dependent increase of around $2°$ C in response to LPS injection [Andreasen et al., 2008]. The control of HR, stimulated by changes in temperature, is modeled by

$$\frac{dH}{dt} = \frac{-H + G(\text{Temp})}{\tau_2}, \tag{7.18}$$

where

$$G(\text{Temp}) = k_H(H_M - H_m)H_H^U(\text{Temp} - T_m) + H_m. \tag{7.19}$$

H_m and H_M represent the minimum and maximum heart rate, respectively. The rate constants are given by τ_2 and k_H.

7.3.3 Pain Perception Threshold

Past studies [Benson et al., 2012; Janum et al., 2016; Wegner et al., 2014] show a dose-dependent relationship between pain perception and inflammation. In particular, Janum et al. [2016] found that endotoxin administration in healthy individuals led to a reduction in PPT and an increase in pain perception to heat stimuli. The relationship between the endotoxin and the PPT is modeled by

$$\frac{d\text{PT}}{dt} = -k_{\text{PT}P}P\ \text{PT} + k_{\text{PT}}(\text{PT}_M - \text{PT}), \tag{7.20}$$

where $k_{\text{PT}P}$ and k_{PT} are rate constants and PT_M is the baseline PPT, prior to the injection of the endotoxin, when $P = 0$. Upon injection, P decreases from the initial value of 2 ng/kg of body weight to zero, causing the PPT to also decrease. Once $P = 0$, the PPT will return to its baseline level.

7.3.4 Nitric Oxide

The vasodilator, nitric oxide, is produced in the endothelium by endothelial, neural, and inducible nitric oxide synthase (NOS). Neuronal and endothelial NOS (nNOS and eNOS, respectively) produce a low, constant amount of NO. Inducible NOS (iNOS) synthesizes NO several hours after endotoxin administration [Chowdhary et al., 2000; Vincent et al., 2000]. Its production is primarily regulated by TNF-α and IL-10. iNOS is expressed and activated in a variety of cells, such as the vascular endothelial cells, smooth muscle cells, and activated monocytes. Monocytes activated by endotoxin have iNOS messenger ribonucleic acid (mRNA) present after 2 hours and iNOS protein after 4 hours [Kirkeboen & Strand, 1999].

Accounting for this, the change in the concentration of NO is modeled by

$$\frac{dN}{dt} = k_{NM} M_A \left(\frac{\text{TNF}(t-\kappa)^{h_{N\text{TNF}}}}{\text{TNF}(t-\kappa)^{h_{N\text{TNF}}} + \eta_{N\text{TNF}}^{h_{N\text{TNF}}}} \right) \left(\frac{\eta_{N10}^{h_{N10}}}{\text{IL}10(t-\kappa)^{h_{N10}} + \eta_{N10}^{h_{N10}}} \right) - k_N N, \qquad (7.21)$$

where M_A are the activated monocytes of the inflammatory model and κ represents the delay in the synthesis of NO after the production of TNF-α and IL-10. The rate constants are given by k_{NM} and k_N and the half-maximum value and exponent are given by $\eta_{N\text{TNF}}$ and $h_{N\text{TNF}}$, respectively.

7.3.5 Resistance

The main pressure change in the systemic circulation occurs in the arterioles, where the resistance against blood flow is high due to the small diameter of the arterioles (30-50 μm). This resistance can be varied considerably by vasoconstriction and vasodilation because the walls of these vessels are equipped with a large amount of smooth muscle cells. These can increase wall tension and thus, reduce the diameter [Batzel et al., 2007]. Therefore, we focus on changing the resistance in the organ bed. The combined effects of a change in the PPT and NO in response to inflammation on the resistance in the organ bed are modeled by

$$\frac{dR}{dt} = k_{\text{RPT}} \left(\frac{\Gamma^2}{\Gamma^2 + \eta_{\text{RPT}}^2} \right) - k_{RN} N - k_R (\text{R} - R_o), \qquad (7.22)$$

117

where $\Gamma = \frac{d\mathrm{PT}}{dt}$ (7.20) and the k terms are rate constants. η_{RPT} is the half-maximum value and R_o is the baseline resistance in the organ bed (i.e. the resistance in the absence of pain or nitric oxide). Prior to the injection of the endotoxin, $\Gamma = 0$ and $N = 0$, ensuring that the resistance remains at its initial level. Upon injection, the PPT begins to decrease, causing Γ^2 to increase and thereby increase the resistance. This causes the initial increase in blood pressure. Two to four hours later, Γ^2 approaches zero and NO begins to increase, causing the resistance to decrease and consequently decrease the blood pressure. Once NO has decreased to its baseline level, R returns to R_o.

7.4   Parameterization

Cardiovascular Model

The parameters of the non-pulsatile cardiovascular model are adapted from the model by Williams et al. [2013] and are shown in Table 7.2. The compliance is computed by rearranging (7.3) to obtain

$$C_i = \frac{V_{\mathrm{str},i}}{p_i},$$

where $V_{\mathrm{str},i} = V_i - V_{un}$ is the stressed volume in compartment i. Values for the stressed volume of each compartment can be found in Table 7.1.

Temperature

For (7.17), T_m is obtained from the experimental data. As experimental data is from young, healthy individuals, it can be assumed that the maximum temperature will not exceed 39.5° C (this is characterized as hyperthermia, which can be life-threatening). Thus, T_M is set at 39.5° C. The rate constants are chosen to modulate the amount of stimulation or dampening from the inflammatory mediators. Since the primary production results from TNF-α and IL-6, k_TTNF and k_{T6} are significantly higher than k_{T10}.

Heart Rate

For (7.19), H_m is the mean heart rate prior to the injection of the endotoxin and can be extracted from the data. Gellish et al. [2007] analyzed the longitudinal relationship between age and maximal

heart rate and found that H_M is related to age by

$$H_M = 207 - 0.7(\text{Age}).$$

Thus, H_M was initialized based on the participant's age. The rate constant k_H controls the rate of increase in HR from the temperature and was chosen to produce dynamics that best aligned with the data. τ_2 controls the overall magnitude of the response and is chosen accordingly.

Pain Perception Threshold

For (7.20), PT_M is the baseline PPT in the absence of the endotoxin. The rate constants $k_{\text{PT}P}$ and k_{PT} are chosen such that the magnitude of decrease in the PPT agrees with the data.

Nitric Oxide

Note that the form of (7.21) is very similar to the equations of the inflammatory model. Thus, the half-maximum values η_{NTNF} are initially set equal to η_{6TNF}. However, due NO's short half life (1 to 40 seconds) and the extremely small quantities that are produced (picomolars) [Hakim et al., 1996], it is difficult to measure quantitatively with a high degree of accuracy. Therefore, the rate constants and half-maximum values are scaled to guarantee a relative concentration of NO in the presence of the endotoxin. The delay κ is chosen to ensure that an increase in N is observed two to four hours after the endotoxin is injected [Kirkeboen & Strand, 1999].

Resistance

The baseline level of the resistance R_o is computed by rearranging (7.2) to obtain

$$R_i = \frac{p_{\text{in}} - p_{\text{out}}}{q_i}.$$

The rate constants of (8.11) are estimated to achieve the appropriate change in the resistance and consequently, the blood pressure.

The half-maximum values of each Hill functions in the control equations are parameterized in a manner similar to the inflammatory model (see Chapter 5). The nominal parameter values of

Table 7.1 *Patient-specific inputs to the coupled cardiovascular-inflammatory model.* Mean values for pressure and heart rate (p_a and H_m) are taken from experimental data over the first two hours of the experiment (i.e. prior to endotoxin administration).

Input	Equation	Unit	Input	Equation	Unit
BSA	$\sqrt{HW/3600}$	m^2	V_{tot}	$(3.229\text{BSA}-1.229)*1000$	mL
V_{un}	10	mL	$V_{\text{tot,sys}}$	$0.85\,V_{\text{tot}}$	mL
$V_{\text{tot,art}}$	$0.20\,V_{\text{tot,sys}}$	mL	$V_{\text{tot,ven}}$	$0.80\,V_{\text{tot,sys}}$	mL
$V_{\text{tot,a}}$	$0.18\,V_{\text{tot,art}}$	mL	$V_{\text{tot,ao}}$	$0.15\,V_{\text{tot,art}}$	mL
$V_{\text{tot,v}}$	$0.85\,V_{\text{tot,ven}}$	mL	$V_{\text{tot,vo}}$	$0.15\,V_{\text{tot,ven}}$	mL
$V_{\text{str,a}}$	$0.18\,V_{\text{tot,a}}$	mL	$V_{\text{str,ao}}$	$0.18\,V_{\text{tot,ao}}$	mL
$V_{\text{str,v}}$	$0.05\,V_{\text{tot,v}}$	mL	$V_{\text{str,vo}}$	$0.05\,V_{\text{tot,vo}}$	mL
V_{ED}	$142-V_{\text{un}}$	mL	V_{ES}	$47-V_{\text{un}}$	mL
q_{tot}	V_{tot}	mL/min	q_{a}	q_{tot}	mL/min
q_{o}	q_{tot}	mL/min	q_{v}	q_{tot}	mL/min
p_{a}	$\frac{1}{N}\sum_{i=1}^{N}p_{a,\text{data}(i)}$	mmHg	p_{ao}	$0.98\,p_{\text{a}}$	mmHg
p_{v}	3.5	mmHg	p_{vo}	3.75	mmHg
H_m	$\frac{1}{N}\sum_{i=1}^{N}H_{\text{data}(i)}$	bpm	T_m	$\text{Temp}_{\text{data}}(1)$	°C
PT_M	$\text{PT}_{\text{data}}(1)$	-	κ	0.4	hr

the coupled model are given in Table 7.2, with the patient-specific inputs to the model given in Table 7.1.

Table 7.2 *Coupled cardiovascular-inflammatory model nominal parameter values and units.*

No.	Parameter	Value	Unit	No.	Parameter	Value	Unit
1	R_a	$(p_a - p_{ao})/q_a$	mmHg min/mL	20	k_{RN}	0.025	mmHg $\cdot$ min/mL $\cdot$ hr
2	R_o	$(p_{ao} - p_{vo})/q_o$	mmHg min/mL	21	k_R	1	$(\mathrm{hr})^{-1}$
3	R_v	$(p_{vo} - p_v)/q_v$	mmHg min/mL	22	η_{TTNF}	185	pg/mL
4	C_a	$V_{str,a}/p_a$	mL/mmHg	23	η_{T6}	560	pg/mL
5	C_{ao}	$V_{str,ao}/p_{ao}$	mL/mmHg	24	η_{T10}	34.7720	pg/mL
6	C_{vo}	$V_{str,vo}/p_{vo}$	mL/mmHg	25	η_{HT}	38	$^\circ$C
7	C_v	$V_{str,v}/p_v$	mL/mmHg	26	η_{NTNF}	100	pg/mL
8	E_m	p_v/V_{ED}	mmHg/mL	27	η_{N10}	4.3465	pg/mL
9	E_M	p_a/V_{ES}	mmHg/mL	28	η_{RPT}	150	$(\mathrm{hr})^{-1}$
10	k_T	0.5	-	29	h_{TTNF}	0.75	-
11	k_{TTNF}	1.5	-	30	h_{T6}	0.75	-
12	k_{T6}	1.5	-	31	h_{T10}	1	-
13	k_{T10}	0.0625	-	32	h_{HT}	2	-
14	k_H	0.25	-	33	h_{NTNF}	3.16	-
15	k_{PTP}	0.115	$(\mathrm{hr} \cdot \mathrm{ng/kg})^{-1}$	34	h_{N10}	0.3	-
16	k_{PT}	0.005	$(\mathrm{hr})^{-1}$	35	T_M	39.5	$^\circ$C
17	k_{NM}	0.0018	$(\mathrm{hr} \cdot \mathrm{noc})^{-1}$	36	H_M	220 - 0.7*Age	bpm
18	k_N	0.8293	$(\mathrm{hr})^{-1}$	37	τ_1	1	$(\mathrm{hr})^{-1}$
19	k_{RPT}	0.1333	mmHg $\cdot$ min/mL $\cdot$ hr	38	τ_2	0.25	$(\mathrm{hr})^{-1}$

The abbreviation noc is the number of cells present.

121

CHAPTER

8

COUPLED MODEL RESULTS & ANALYSIS

The sensitivity analysis, identifiability analysis, and optimization techniques presented in Chapter 4 have been applied to the coupled cardiovascular-inflammatory model. As shown in Figure 8.1 temperature is predicted as a function of the inflammatory mediators and heart rate is predicted from temperature. The pain perception threshold is modeled as function the pathogen. Finally, pain perception and nitric oxide, modeled as a function of the inflammatory mediators, combine to affect blood pressure. Thus, the coupled model can be divided into submodels, which we analyze separately.

The analysis for the mediator-temperature submodel, temperature-heart rate submodel and pathogen-pain submodel are presented in Sections 8.2, 8.3, and 8.4, respectively. The coupled model analysis is presented in Sections 8.5 and 8.6. In addition to optimizing the parameters of the coupled model, we analyze changes in heart rate variability (HRV) and relate these changes to the optimized parameters of the model. The results of the model are presented in Section 8.7, with the analysis of HRV given in Section 8.7.2. The results are discussed in Section 8.8.
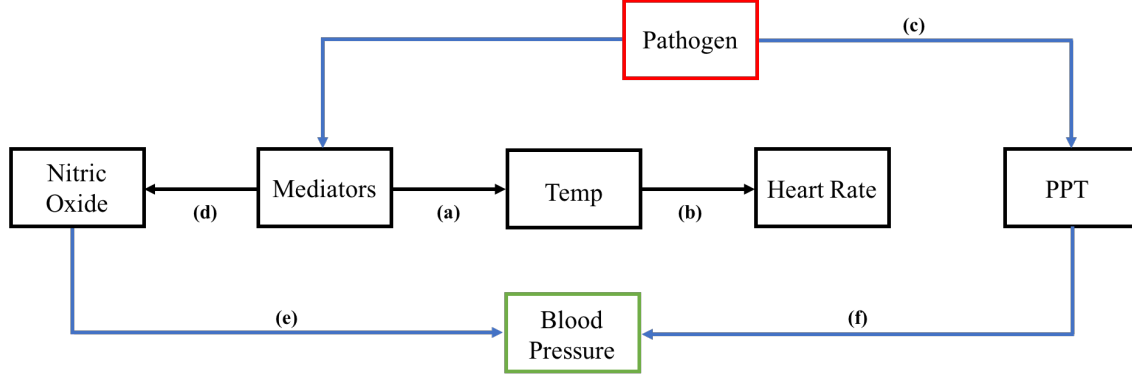
Figure 8.1 *Coupled cardiovascular inflammatory model.* Mediators are produced in response to the pathogen. (a) Increase in mediator production causes the temperature to increase. (b) The temperature increase causes heart rate to increase. (c) The pathogen reduces the pain perception threshold, which (f) in turn impacts blood pressure. (d) Mediators produce nitric oxide, which lead to (e) vasodilation (delayed).

8.1 Least Squares Formulation

Recall from Chapter 3 that each participant had their temperature, heart rate, pain perception threshold, and blood pressure recorded periodically throughout the experiment. Thus for each submodel, we aim to find a parameter set $\hat{\theta}$ that minimizes the least squares error between the computed and measured values. That is,

$$\hat{\theta} = \arg\min_{\theta} J(\theta), \qquad \text{where} \qquad J(\theta) = R^T R, \tag{8.1}$$

where

$$R = \frac{1}{\sqrt{N}} \frac{Y - y}{Y}, \tag{8.2}$$

where Y is the data, y is the model output, and N is the number of data points. The mediator-temperature and pathogen-pain submodels are optimized against temperature and pain perception threshold data. The temperature-heart rate submodel is optimized against the smoothed mean heart rate data. Finally, the coupled model is optimized against the cuff blood pressure, as well as the mean blood pressure data, measured with a finapres. Prior to optimization, sen-

sitivity and identifiability analysis are used to identify those parameters that are sensitive and uncorrelated.

8.2 Mediator-Temperature Submodel

Recall from Chapter 7, that temperature can be modeled by

$$\frac{d\,\text{Temp}}{d\,t} = \frac{-\text{Temp} + F(\text{TNF, IL6, IL10})}{\tau_1}, \tag{8.3}$$

where

$$
\begin{aligned}
F(\text{TNF, IL6, IL10}) \;=\;\; & k_T(T_M - T_m)\Big(k_{T\text{TNF}}H_T^U(\text{TNF} - q_{\text{TNF}}) + k_{T6}H_T^U(\text{IL6} - q_{\text{IL6}}) \\
& - k_{T10}(1 - H_T^D(\text{IL10} - q_{\text{IL10}}))\Big) + T_m.
\end{aligned}
\tag{8.4}
$$

To find a parameter set satisfying (8.1) for the mediator-temperature submodel, sensitivity and identifiability analysis are used.

Sensitivity Analysis

Recall from Chapter 4 that sensitivities can be computed on either a local or global level. The proceeding analysis is local. The sensitivity matrix defined by $\chi = \frac{\partial y}{\partial \theta}$ is used to determine the sensitivity of the model to changes in the parameters. To remain consistent with the inflammatory model, we define

$$
\chi = \frac{\partial R}{\partial \theta} =
\begin{bmatrix}
\frac{\partial y_1(t_1)}{\partial \theta_1} & \cdots & \frac{\partial y_1(t_1)}{\partial \theta_q} \\
\vdots & \ddots & \vdots \\
\frac{\partial y_1(t_N)}{\partial \theta_1} & \cdots & \frac{\partial y_1(t_N)}{\partial \theta_q} \\
\frac{\partial y_2(t_1)}{\partial \theta_1} & \cdots & \frac{\partial y_2(t_1)}{\partial \theta_q} \\
\vdots & \ddots & \vdots \\
\frac{\partial y_m(t_N)}{\partial \theta_1} & \cdots & \frac{\partial y_m(t_N)}{\partial \theta_q}
\end{bmatrix},
\tag{8.5}
$$

where R is defined in (8.2). Since the inflammatory model is optimized for each data set prior to the coupling, the sensitivity analysis will focus on the parameters of the model used in the temperature

equation. That is, $\theta = (\tau_1, T_M, T_m, k_T, k_{T\text{TNF}}, k_{T6}, k_{T10}, \eta_{T\text{TNF}}, \eta_{T6}, \eta_{T10}, h_{T\text{TNF}}, h_{T6}, h_{T10})$.

To ensure that the parameter values remain positive during the optimization, we use $\tilde{\theta} = \log\theta$ so that χ, like the inflammatory model, is a relative sensitivity matrix given by

$$\chi = \frac{\partial R}{\partial \tilde{\theta}} = \frac{\partial R}{\partial \log\theta} = \frac{\partial R}{\partial \theta}\theta. \tag{8.6}$$

The ranked sensitivities for this submodel are shown in Figure 8.2. The sensitivities are ranked by taking the two norm of the sensitivity matrix. Using a cutoff of $\phi = 10\sqrt{\varphi}$, where $\varphi = 10^{-8}$ is the integration tolerance, the parameters are divided into 10 sensitive and 3 insensitive parameters.

Identifiability Analysis & Subset Selection

Similar to the inflammatory model, structural identifiability cannot be determine from this sub-model, due to the complexity. In fact, structural identifiability will not be determined for any of the proceeding submodels. However, insight can be obtained by analyzing their equations. In the same fashion as the inflammatory model, the half-maximum values and exponents of the Hill functions are fixed at their nominal values due to the difficulty in estimating them (see Chapter 5 for further details). In (8.4), it is clear that k_T and $k_{T\text{TNF}}$ can be combined into one parameter k_1. In the same fashion, k_T and k_{T6} can be combined into k_2. Thus, all three parameters cannot be estimated together. To account for this, k_T is fixed at its nominal value.

By the nature of the experiment, it can be assumed that the temperature will not rise above $39.5°C$ and the baseline temperature can be extracted from the data. Thus, T_m and T_M are also fixed at their nominal values.

Practical Identifiability

The structural correlation method (SCM) [Olufsen & Ottesen, 2013], described in Chapter 4, is used to determine if remaining the 3 sensitive parameters are correlated. Analysis of covariance of these parameters showed that (k_{T6}, τ_1) can be uniquely determined, using a cutoff of $\zeta = 0.90$.

Figure 8.2 *Relative parameter sensitivities ranked from most to least sensitive for the mediator-temperature submodel.* Black line shows cutoff between sensitive and insensitive parameters. Cutoff ϕ was chosen to be $10\sqrt{\varphi}$, where $\varphi = 10^{-8}$ is the integration tolerance. Red squares and parameters listed in red denote sensitive parameters that are considered for optimization. Black circles denote parameters that are optimized.

8.3 Temperature-Heart Rate Submodel

From Chapter 7, we have

$$\frac{dH}{dt} = \frac{-H + G(\text{Temp})}{\tau_2}, \tag{8.7}$$

where

$$G(\text{Temp}) = k_H(H_M - H_m)H_H^U(\text{Temp} - T_m) + H_m. \tag{8.8}$$

Sensitivity and identifiability analysis of the parameters $\theta = (\tau_2, H_M, H_m, k_H, \eta_{HT}, h_{HT})$ is used to find a subset that can be estimated, given available data.

126

Figure 8.3 *Relative parameter sensitivities ranked from most to least sensitive for the temperature-heart rate submodel.* Black line shows cutoff between sensitive and insensitive parameters. Cutoff ϕ was chosen to be $10\sqrt{\varphi}$, where $\varphi = 10^{-8}$ is the integration tolerance. For this submodel, only two parameters (shown by red squares and black circles) are considered for optimization and practical identifiability proves them to be uncorrelated.

Sensitivity and Identifiability Analysis & Subset Selection

Results of the sensitivity analysis (depicted in Figure 8.3), using the same cutoff $\phi = 10\sqrt{\varphi}$, shows that all 6 parameters are sensitive. However, the half-maximum values and exponents cannot be uniquely identified. Additionally, the minimum and maximum heart rate values can be determined from the data. Thus, only τ_2 and k_H remain. Practical identifiability shows that these parameters are uncorrelated when $\zeta = 0.90$ and can therefore be uniquely optimized.

8.4   Pathogen-Pain Submodel

The pain perception threshold (PPT) is predicted from the pathogen as

$$\frac{d\,\text{PT}}{d\,t} = -k_{\text{PT}P}\,P\;\text{PT} + k_{\text{PT}}(\text{PT}_M - \text{PT}). \tag{8.9}$$

Figure 8.4 *Relative parameter sensitivities ranked from most to least sensitive for the pathogen-pain submodel.* Black line shows cutoff between sensitive and insensitive parameters. Cutoff ϕ was chosen to be $10\sqrt{\varphi}$, where $\varphi = 10^{-8}$ is the integration tolerance. For this submodel, only two parameters (shown by red squares and black circles) are considered for optimization and practical identifiability proves them to be uncorrelated.

For this model, we are concerned with the parameters $\theta = (\text{PT}_M, k_{\text{PT}P}, k_{\text{PT}})$.

Sensitivity and Identifiability Analysis & Subset Selection

Sensitivity analysis shows that all 3 parameters are sensitive (see Figure 8.4). However, since the initial threshold PT_M is given by the data, it will be fixed at its nominal values. Thus, correlation analysis is applied to the parameters $k_{\text{PT}P}$ and k_{PT}. Results showed that they are uncorrelated.

8.5   Steady-State Coupled Cardiovascular Inflammatory Submodel

In the absence of an endotoxin or any other control factors, heart rate and blood pressure are expected to remain constant. In order to ensure that the model begins at steady-state, the initial values for the volumes are computed by setting the change in volume in compartment i, $\frac{dV_i}{dt} = 0$ for

each compartment and then solving for V_i in terms of the parameter values for all compartments. This is done using `Maple2018`. Note that volume is conserved since $\sum_i \frac{dV_i}{dt} = 0$, so that one state variable can be eliminated.

Due to the patient-specific inputs to the model (see Table 7.1 of Chapter 7), the initial conditions are unique between subjects. To ensure that the model represents the data well during steady-state (i.e. from $t = -2$ to $t = 0$), the parameters are optimized. To accomplish this, we have the submodel

$$\frac{dV_v}{dt} = q_v - Q, \qquad \frac{dV_a}{dt} = Q - q_a,$$
$$\frac{dV_{vo}}{dt} = q_o - q_v, \qquad \frac{dV_{ao}}{dt} = q_a - q_o, \tag{8.10}$$

where $q = \frac{p_{in} - p_{out}}{R_a}$ and the flow through the heart is modeled by

$$Q = H_m V_{\text{str}},$$

since the heart rate is constant from $t = -2$ to $t = 0$. Thus, we have $\theta = (R_a, R_v, R_o, C_a, C_{ao}, C_v, C_{vo}, E_m, E_M)$.

Sensitivity and Identifiability Analysis & Subset Selection

Sensitivity analysis reveals that all 9 parameters are sensitive, using the same cutoff $\phi = 10\sqrt{\varphi}$. Keeping in mind that we cannot optimize more than one resistance and more than one capacitor due to the resistors being in series and the capacitors being in parallel, we perform subset selection using the SCM. Figure 8.5 shows that two parameters, C_a and R_o, can be estimated.

8.6 Dynamic Coupled Cardiovascular Inflammatory Submodel

The effects of nitric oxide (NO) and pain perception on blood pressure after the endotoxin administration (from $t = 0$ to $t = 6$) are modeled by changing the resistance in the organ bed as

$$\frac{dR}{dt} = k_{RPT}\left(\frac{\Gamma^2}{\Gamma^2 + \eta_{RPT}^2}\right) - k_{RN}N - k_R(R - R_0), \tag{8.11}$$
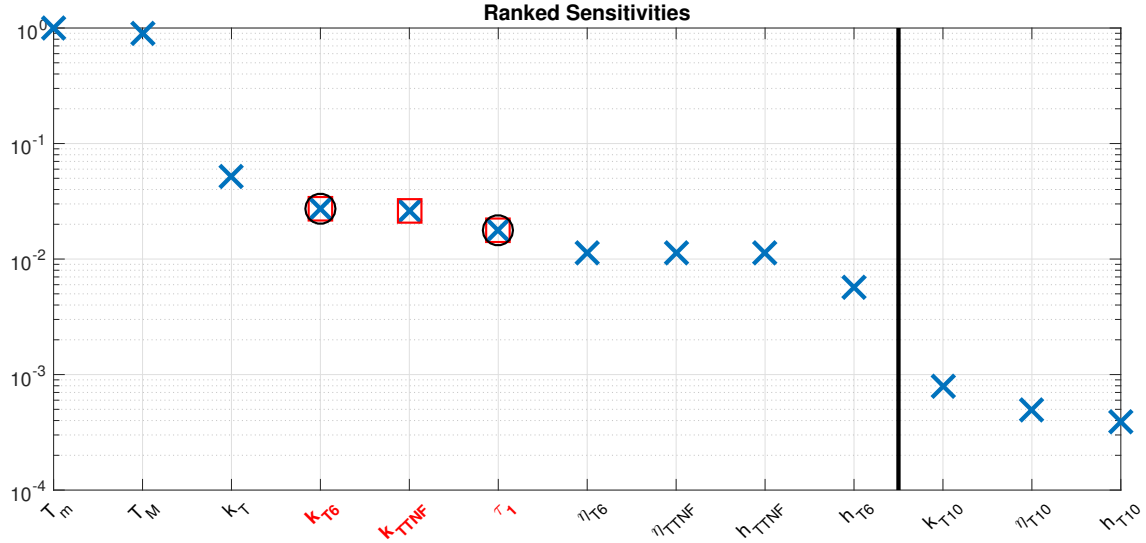
Ranked Sensitivities
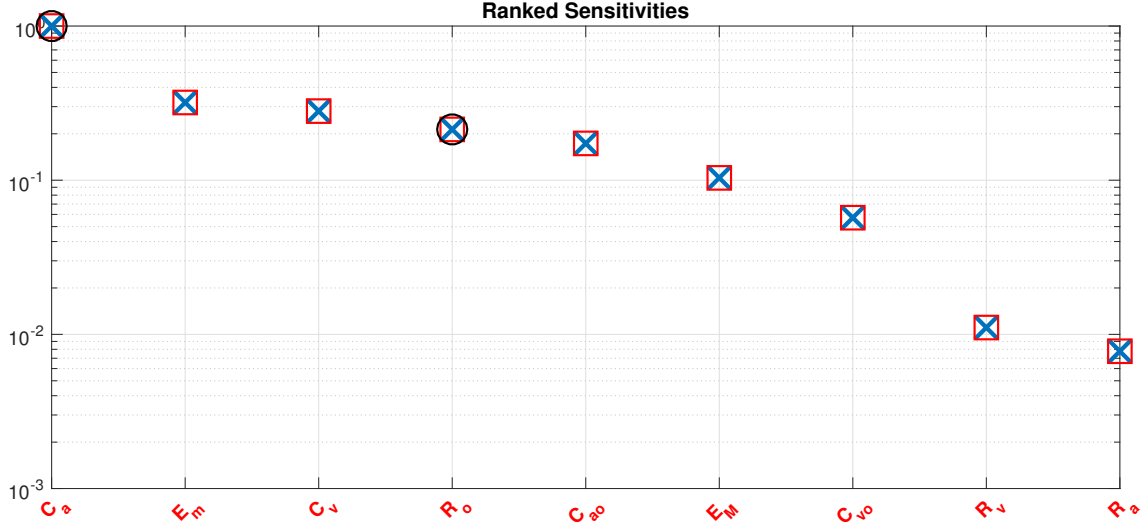
Figure 8.5 *Relative parameter sensitivities ranked from most to least sensitive for the steady-state coupled model.* Black line shows cutoff between sensitive and insensitive parameters. Cutoff ϕ was chosen to be $10\sqrt{\varphi}$, where $\varphi = 10^{-8}$ is the integration tolerance. Red squares and parameters listed in red denote sensitive parameters that are considered for optimization. Black circles denote parameters that are optimized.

where $\Gamma = \frac{d\text{PT}}{dt}$ (8.9) and NO is modeled by

$$\frac{dN}{dt} = k_{NM} M_A \left(\frac{\text{TNF}(t-\kappa)^{h_{N\text{TNF}}}}{\text{TNF}(t-\kappa)^{h_{N\text{TNF}}} + \eta_{N\text{TNF}}^{h_{N\text{TNF}}}} \right) \left(\frac{\eta_{N10}^{h_{N10}}}{\text{IL}10(t-\kappa)^{h_{N10}} + \eta_{N10}^{h_{N10}}} \right) - k_N N. \tag{8.12}$$

It should be noted that due to the short half-life of NO, we did not have NO data available and therefore are using a relative amount of NO produced by the inflammatory mediators to predict the resistance. For this reason, the parameters of the NO equation will be fixed at their nominal levels and the analysis will be done on the remaining parameters $\theta = (k_{RPT}, k_{RN}, k_R, \eta_{RPT}, h_{RPT})$.

Sensitivity and Identifiability Analysis & Subset Selection

As shown in Figure 8.6, sensitivity analysis reveals that all 5 parameters are sensitive. Following the methods of the inflammatory model, the half-maximum values and exponents are fixed at their

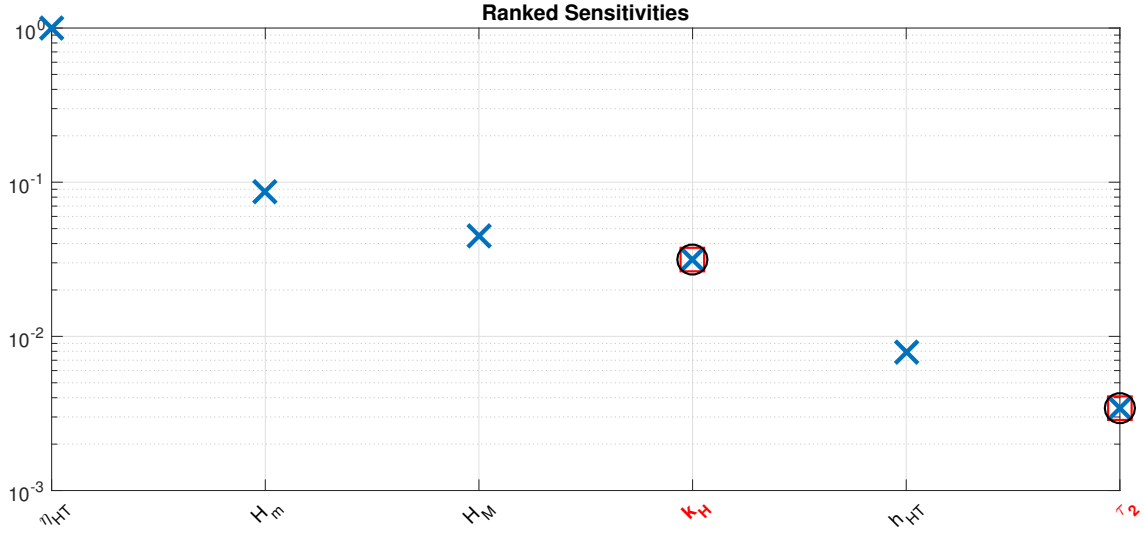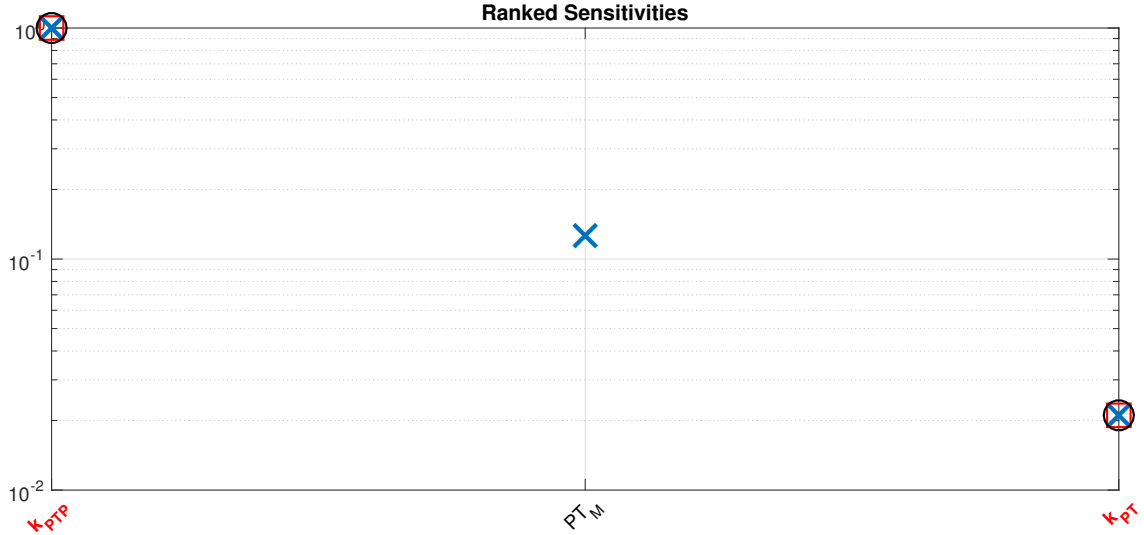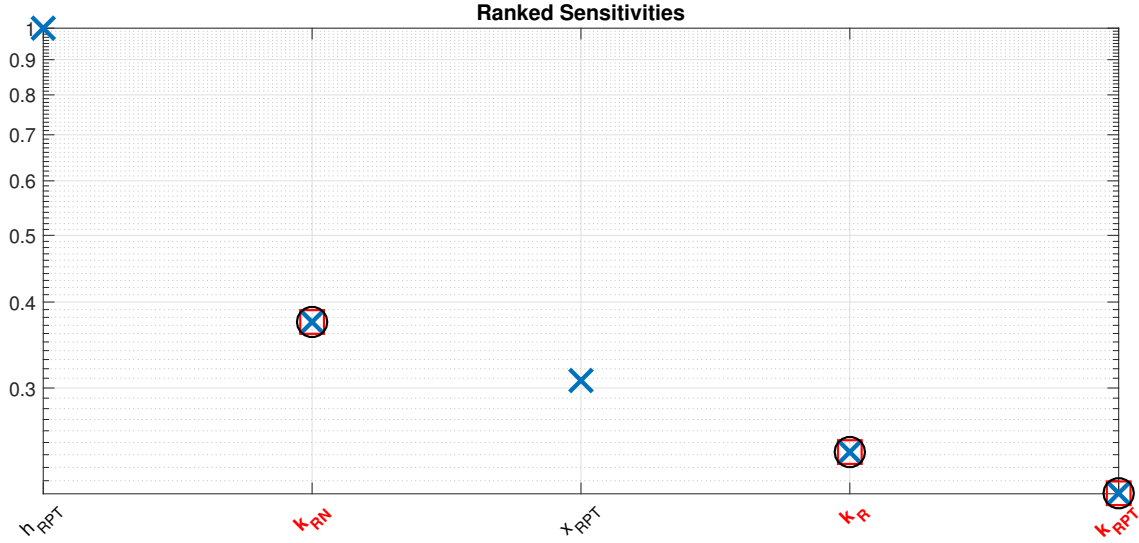**Figure 8.6** *Relative parameter sensitivities ranked from most to least sensitive for the dynamic coupled model.* Black line shows cutoff between sensitive and insensitive parameters. Cutoff ϕ was chosen to be $10\sqrt{\varphi}$, where $\varphi = 10^{-8}$ is the integration tolerance. Red squares and parameters listed in red denote sensitive parameters that are considered for optimization. Black circles denote parameters that are optimized.

nominal values, and we test for correlations among the remaining 3 parameters. Subset selection shows that no correlations exist between the remaining parameters so they will all be optimized.

8.7   Results

For each submodel, the parameters were optimized against the Day A data for each of the data sets using a combination of the Nelder-Mead and Levenberg-Marquardt algorithms. Temperature data was available for all 20 data sets, however the heart rate and blood pressure data was either noisy or unavailable. We focused our analysis on the 18 available data sets. To remain consistent with the inflammatory model and unless otherwise stated, the upper and lower bounds for Levenberg-Marquardt are set to be approximately one-quarter of and four times the nominal parameter values, respectively. All submodels, excluding the steady-state coupled submodel, were optimized

from $t = 0$ to $t = 6$. That is, after the endotoxin was given at $t = 0$.

8.7.1 Parameter Optimization

The optimal parameters for the submodels are given in Table 8.1. The R^2 statistic was used to quantify the accuracy of the mediator-temperature submodel. Due to the scarcity of available data points for the pain perception threshold (3 available data points), the R^2 value could not be used as a useful statistic for the model. The large variation in the mean blood pressure and heart rate data were not captured by this model and therefore, the linear regression model used for the R^2 is not useful for these submodels either. For the mediator-temperature submodel, $R^2 \geq 0.87$. The upper and lower bounds of the Levenerg-Marquardt algorithm had to be expanded to range between 1E-04 and 3 for τ_2 in order to ensure that the optimizer did not force the parameters to the bounds and that physiologically feasible results were obtained. The bounds for the steady-state and dynamic coupled models were also extended to one-sixteenth and sixteen times the nominal value. For seven data sets, optimizing the dynamic model resulted in poorer fits than using the nominal dynamic parameters. This was due to the scarcity of data during the times when the majority of the dynamics are observed (i.e. the peaks). In those cases, the nominal set was used instead. To remain consistent with the results of the inflammatory model, the optimal results shown in Table 8.1 are for the same individual as the results shown in Table 6.1 of Chapter 6.

8.7.1.1 Normal versus Abnormal Responses

As discussed in Chapter 3, the participants were divided into abnormal and normal responders. To further understand differences between the two response types, we compared the changes in blood pressure and heart rate between a normal and an abnormal responder, shown in Figure 8.7. The top two panels of Figure 8.7 and Figure 8.8(a) show that the model is able to capture both the normal and abnormal responses well.

The differences in the blood pressure responses between the normal and abnormal responders are reflected in the optimal parameter values. The rate responsible for the increase in resistance as a result of a decrease in PPT k_{RPT} was significantly larger in the abnormal responder (normal: 0.893, abnormal: 8). Additionally k_{RN}, the rate at which the resistance decreases in response to nitric oxide, was larger in the abnormal responder (normal: 0.430, abnormal: 0.750). Similar results

Table 8.1 *Nominal and optimal parameter values for a particular subject.* Parameters were optimized using a combination of the Nelder-Mead and Levenberg-Marquardt algorithms for the mediator-temperature, temperature-heart rate, pathogen-PPT, steady-state (SS) coupled, and dynamic coupled submodels. The mean plus/minus the standard deviation for each parameter is also included.

Submodel	Parameter	Nominal θ	Optimal $\hat{\theta}$	Mean $\pm$ Std
Med-Temp	τ_1	1	2.243	1.794 ± 0.814
	k_{T6}	1.5	4.426	3.242 ± 1.689
Temp-HR	τ_2	0.25	0.003	0.439 ± 0.559
	k_H	0.25	0.353	0.312 ± 0.086
Path-PPT	k_{PTP}	0.115	0.080	0.142 ± 0.075
	k_{PT}	0.005	0.011	0.086 ± 0.165
SS Coupled	R_o	1.065	1.034	0.915 ± 0.152
	C_a	1.369	1.452	1.524 ± 0.327
Dynamic Coupled	k_{RPT}	8	0.893	5.784 ± 3.120
	k_{RN}	0.750	0.430	0.948 ± 0.635
	k_R	1	0.642	1.303 ± 0.692

were found in the heart rate response, shown in Figure 8.8. The rate constant τ_2 was smaller in the normal responder (normal: 0.413, abnormal: 0.900). The resistance and compliance parameters were of the same magnitude between response types (R_o normal: 1.034, R_o abnormal: 0.969 and C_a normal 1.452 and C_a abnormal: 1.533).

8.7.1.2 Model Validation

To validate the coupled model, the model was ran using the optimal parameters for Day A against the data for Day B. Since the initial conditions for the temperature, pain perception threshold, blood pressure, and heart rate are derived from the data, these values were changed for the Day B data. A comparison of the results for a particular subject for Day A versus Day B is shown in Figure 8.9. Though the initial value for the heart rate was lower than the mean heart rate data, the predictions of heart rate and subsequently blood pressure fit well to the data.

133

8.7.2 Heart Rate Variability Analysis

Heart rate variability is a measure of how much the heart rate varies from beat to beat. Variations in time differences between successive heart beats can be analyzed using time or frequency domain analysis [Huston & Tracey, 2011]. Using time domain analysis, statistical measurements of the RR-intervals provides information about the inter-beat variability. Parameters including the standard deviation of the average beat-to-beat intervals (SDANN) and the percentage of interval differences of successive inter-beat intervals greater than 50ms (pNN50) provide quantitative information about the variability from beat to beat. Frequency domain analysis uses spectral methods, in particular power spectral density analysis (PSD), to understand the RR-interval variation. PSD explains how power is distributed as a function of frequency. The high frequency (HF) variability and low frequency/high frequency ratio (LF/HF) is believed to provide a measure of vagal and sympathetic activity.

To analyze HRV, we follow the approach proposed by Jan et al. [2010], who used HRV to study the influence of gender to an in vivo endotoxin challenge in healthy humans. Following their approach, we examine predictions of 1) SDANN, 2) pNN50, 3) HF variability, and 4) the LF/HF ratio by analyzing the average beat-to-beat intervals hourly, over three 5-minute periods computed using built-in HRV toolbox in Labchart ®[ADInstruments Inc. Colorado Springs, USA]. To understand how the differences between normal and abnormal responses correlated with changes in HRV, we compared HRV predictions for the subjects shown in Figures 8.7 and 8.8. HRV predictions (Figure 8.10) showed that the SDANN, the pNN50 and the HF components were significantly larger in subjects with abnormal responses, reflecting a higher vagal firing rate and greater variability between heart beats. Similar results were found in the other two subjects with similar abnormal responses.

8.8 Discussion

In this chapter, we presented the results of the coupled model of the inflammatory response and the associated cardiovascular dynamics in response to endotoxin. The intra- and inter-individual variations in the cardiovascular response to intravenous endotoxin, shown in Figures 8.7-8.10, demonstrate the importance of coupling the inflammatory response with the cardiovascular

dynamics.

The differences in the blood pressure responses are primarily as a result of nitric oxide and changes in the pain perception threshold. To account for the large increase in blood pressure in the abnormal response, k_{RPT} must be significantly larger since the change in PPT are the same between the responders. The amount of NO produced by the inflammatory mediators is lower in the abnormal response, which implies a slower increase in blood pressure. This results in a larger value for k_{RN} in the abnormal responder. As shown in (8.8), heart rate is primarily regulated by temperature. While the temperatures appear to increase at the same rates, heart rate increases faster in the normal responder in Figure 8.8. This is responsible for the smaller τ_2 and by the form of the equation (8.8), a smaller τ_2 causes a faster increase in heart rate.

In agreement with the findings by Marsland et al. [2007], HRV analysis suggested that greater basal vagal activity, given by the HF parameter, correlated with an attenuated release of TNF-α. This high basal vagal activity was also associated with an increase in the production of the anti-inflammatory mediator IL-10. In general, the abnormal responders were found to have a higher level of vagal activity, accompanied by greater variability in heart rate from beat to beat. Additionally, the noted differences discussed above produced similar results in the other abnormal responses, regardless of classification (i.e. high levels of both TNF-α and IL-10 or an increased level of IL-6 and IL-8.

In the absence of a fever, increase vagal activity causes a decrease in heart rate. An increase in body temperature in response to the endotoxin is said to be associated with adrenergic stimulation [Evans et al., 2015] igniting a flight-or-fight mode. The results shown in Figures 8.8 give way to the possibility that temperature overrides the increased vagal response and allows heart rate to increase. The smaller increase in heart rate in the abnormal responder can be explained by the higher basal level of vagal activity and the smaller increase in temperature. This contrasts the normal responder who exhibited lower baseline vagal activity and a larger increase in temperature, which explains the large increase in heart rate.

It should be noted that the cardiovascular responses presented here and not the only pathways regulating this response. The increase in heart rate in response to the fever can cause vasoconstriction of the skin in an effort to retain heat. This vasoconstriction will cause blood pressure to increase. Additionally, the injection of the endotoxin increases the sensitivity to pain, resulting in sympathetic stimulation which affects heart rate. For the coupled model presented here, we have

focused on the main components of the response but plan to incorporate these other factors into the model. We will also use DRAM to confirm the results of the subset selection in future work.

The discussion above makes it clear that HRV parameters and temperature can provide important information about the inflammatory and cardiovascular response. As information about the inflammatory response, as well as levels of the pain perception threshold, provide insight into the blood pressure response, each of these factors can be combined to allow for real-time and non-invasive analysis of the inflammatory and cardiovascular response. Our model revealed a distinct relationship between the magnitude of the inflammatory response and vagal response, as well as temperature. Though the participants in the experiment were all young, healthy individuals, we were able to identify particular markers for abnormal responses, correlating with changes in HRV. Therefore, improved future modeling of HRV, temperature, and the perception of pain may eventually allow physicians to perform simple real-time monitoring and enable them to intervene prior to sepsis propagation.
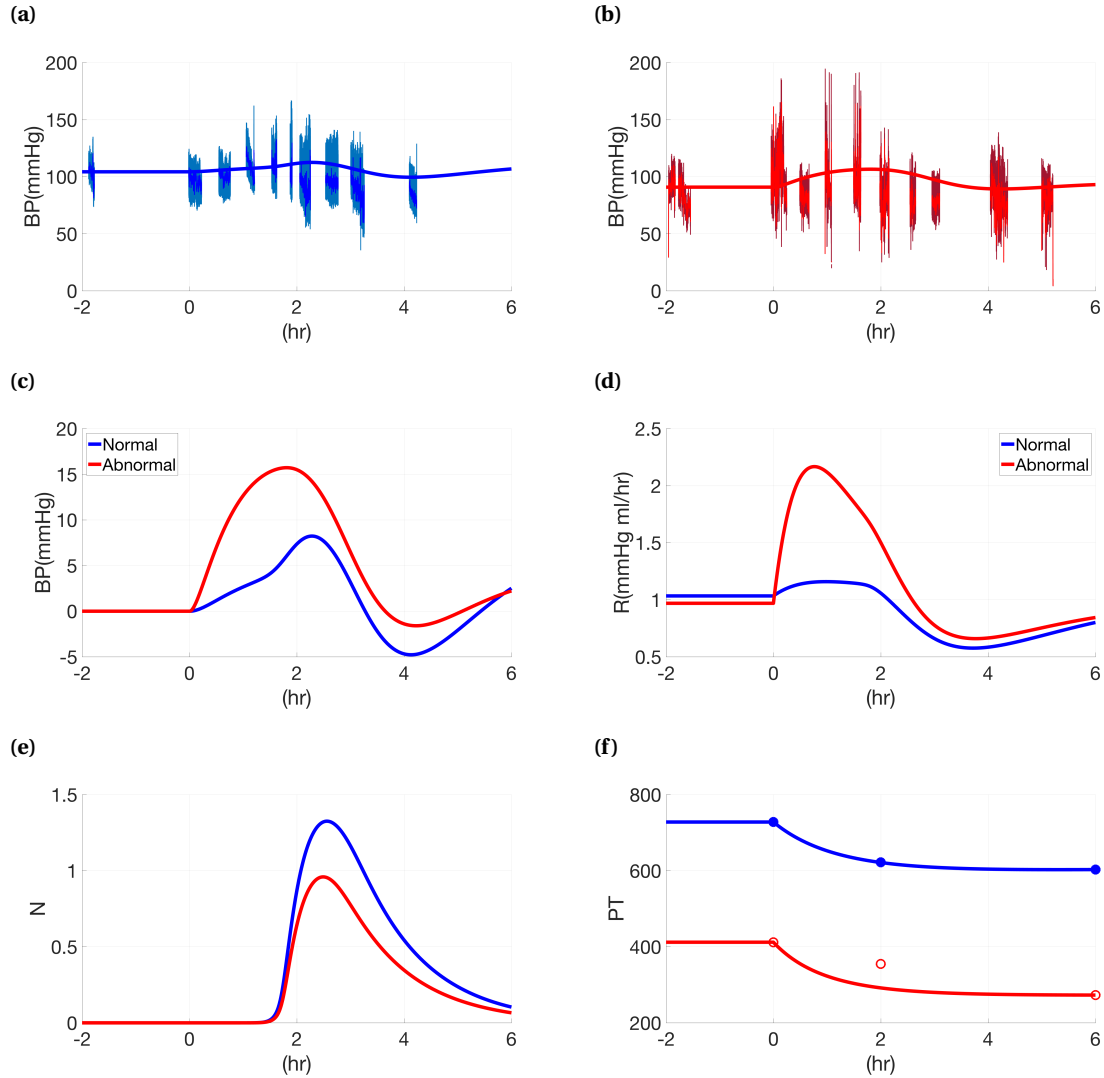
Figure 8.7 *Comparison of normal and abnormal responders to endotoxin challenge.* (a-b) Model fits to mean blood pressure data for normal (left) and abnormal (right) responder. (c) Relative changes in mean arterial blood pressure. (d) Changes in organ bed resistance. (e) Changes in nitric oxide. (f) Model fits to pain perception tolerance data. Normal responses and abnormal responses are shown in blue and red, respectively. Participants were given 2 ng/kg body weight of endotoxin at $t = 0$ h. Blood pressure signal was recorded from $t = -2$ to $t = 6$ h.

(a)

(b)
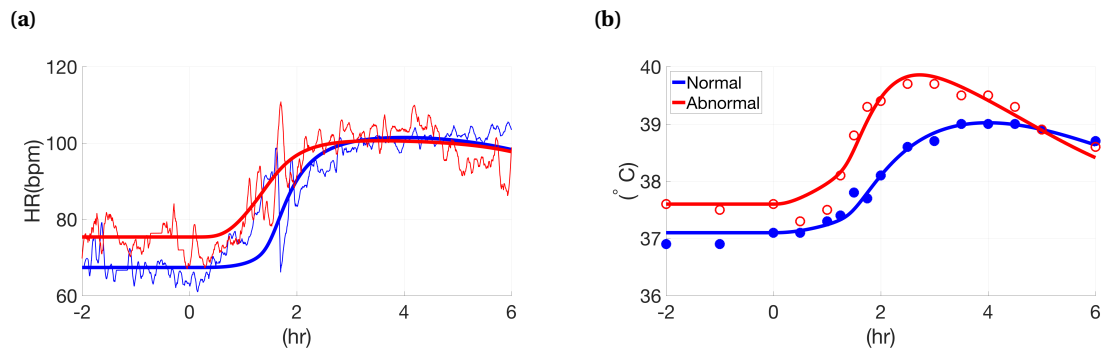
Figure 8.8 *Comparison of heart rate and temperature responses in normal and abnormal responders.*
(a) Model fits to mean heart rate data. (b) Model fits to temperature. Normal responses and abnormal
responses are shown in blue and red, respectively. Participants were given 2 ng/kg body weight of endo-
toxin at $t = 0$ h. Body temperature and ECG signals were recorded from $t = -2$ to $t = 6$ h.

138
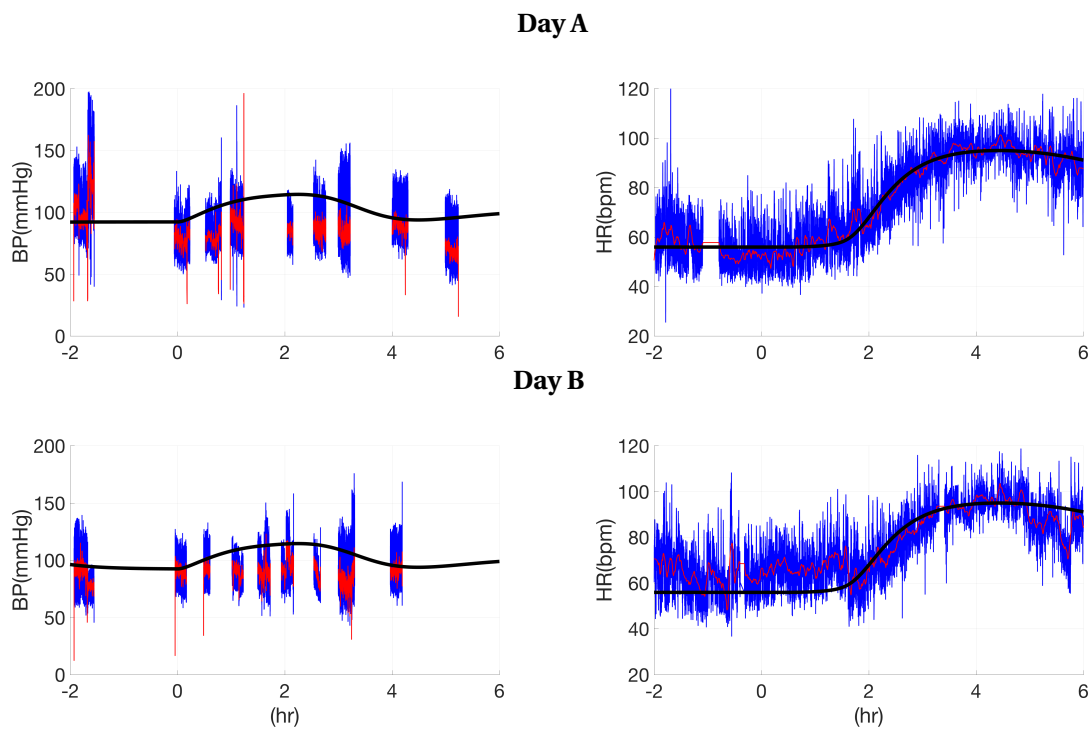
Day A

Day B

Figure 8.9 *Day A versus Day B Model Predictions.* Blood pressure and heart rate model predictions for one individual plotted against data for Day A (top panels) and Day B (bottom panels). The model was initially optimized against Day A data. Participants were given 2 ng/kg body weight of endotoxin at $t = 0$ h. Blood pressure and ECG signals were recorded from $t = -2$ to $t = 6$ h.

139
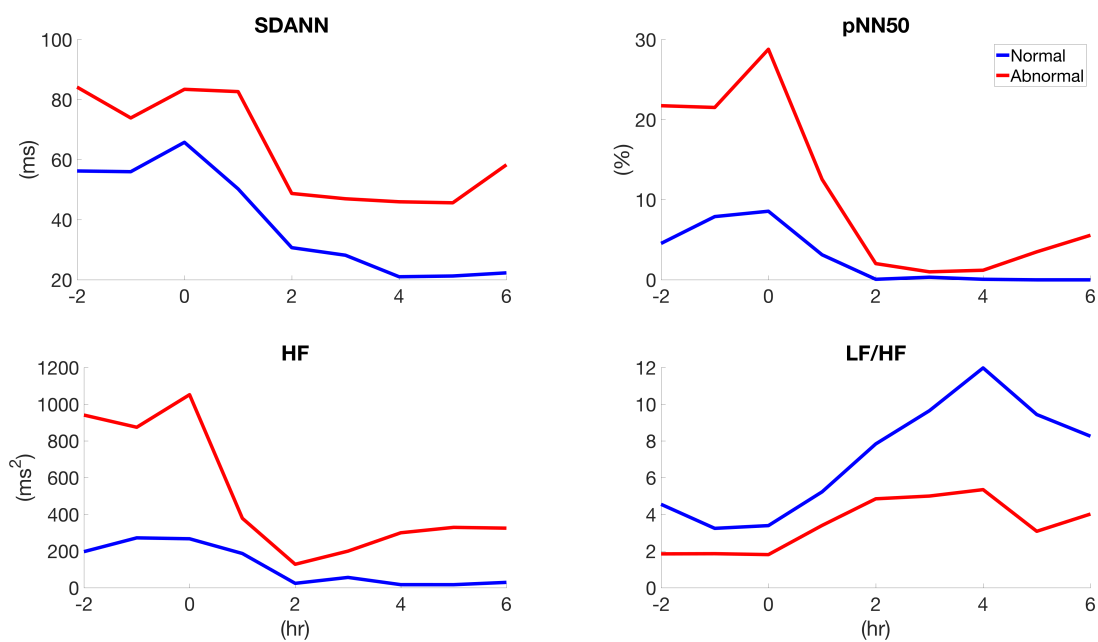
Figure 8.10 *Frequency domain measures of HRV for normal and abnormal responders.* SDANN, pNN50, HF, and the LF/HF Ratio. Participants were given 2 ng/kg body weight of endotoxin at $t = 0$ h and HRV parameters were obtained by analyzing the average beat-to-beat intervals hourly, over three 5-minute periods.
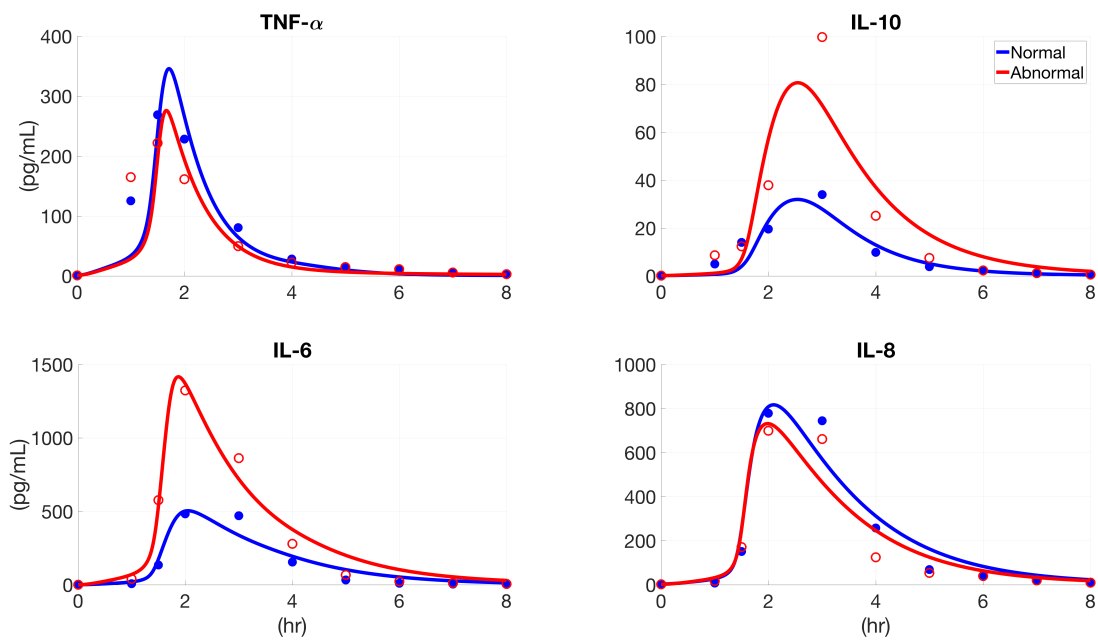
Figure 8.11 *Inflammatory Model Predictions.* A normal model fit (blue line) against data (blue circles) and an abnormal model fit (red line) against data (red unfilled circles) are shown. Participants were given 2 ng/kg body weight of endotoxin at $t = 0$ h, and inflammatory mediator levels were measured at $t = 2, 0, 1, 1.5, 2$ h and hourly for the next 4 hours. Pseudodata was added at $t = 7$ and 8 h to ensure that mediators had appropriate time to decay.

CHAPTER

$$9$$

CONCLUDING REMARKS

In this study, a mathematical model of the acute inflammatory response to an endotoxin challenge has been developed. The model is based on the biological interactions between the primary components of the immune system, including the resting and activated monocytes, pro-inflammatory mediators TNF-α, IL-6, and IL-8, and the anti-inflammatory mediator IL-10. The model analyzed in this thesis was developed to balance the complexity between simple models [Kumar et al., 2004; Reynolds et al., 2006] and more rigorous models [Chow et al., 2005; Clermont et al., 2004a]. Specific attention was paid to develop a model that allows for a complete physiological understanding of each pathway and parameter value. The model was rendered patient-specific through the use of sensitivity analysis, identifiability analysis, and parameter optimization. Model predictions fit well against the experimental data. Analysis of parameters differences allowed us to distinguish between normal and abnormal responders.

The inflammatory response was coupled with a non-pulsatile cardiovascular model allowing us to study changes in heart rate and blood pressure in response to an endotoxin. The non-pulsatile

model is the first model created by integrating the more complex pulsatile model, using the same parameters as the pulsatile model. We have used this coupled model to study our hypothesize that temperature, nitric oxide, and pain are the effectors that connect the immune and cardiovascular responses. This hypothesis may explain the observed differences between mice and humans. Like the inflammatory model, the coupled cardiovascular-inflammatory model has been made patient-specific through the use of sensitivity analysis, identifiability analysis, and parameter estimation. This is the first model of this type, as the coupling of the two responses has primarily been focused on the effect of the cardiovascular system on the inflammatory response. Estimated parameters were subsequently related to changes in heart rate variability, allowing for us to investigate how changes in HRV are associated with changes in inflammatory mediators.

The key difference between our mathematical model and previously published models of the inflammatory response is the analysis and modeling of *in vivo* human data, as opposed to mice or swine data. Key differences in their responses, as presented in [Seok et al., 2013] raise question as to the validity in modeling the human inflammatory response based on animal data. Furthermore, while previous models predict a mean acute inflammatory response, our model parameters have been optimized on an individual basis, making for a subject-specific model. The identified and modeled associations between inflammatory responses and changes in HRV suggest that HRV data may be further analyzed and used as a non-invasive real-time monitoring marker of early sepsis onset.

One of the limitations of the current model was the sparseness of the available data points. The majority of the changes in the dynamics of the system occur between 1 and 3 hours after endotoxin administration. Thus, having more data points available during those times, perhaps every 15 minutes, may have provided more accurate results. For example, we expect TNF-α to peak 1.5 to 2 hours after the subject is given the endotoxin. However, due to the time points at which the data was collected, we cannot predict exactly when the cytokine level peaks. Additionally, having data for the numbers of circulating resting and activated monocytes may have provided insight as to why a particular subject has a specific response to the endotoxin versus another since the monocytes are responsible for the measured mediator cascade. Similar issues were found with the pain perception data, which were only measured at three time points throughout the experiment. Noise within the blood pressure response made it difficult to accurately predict the response in several individuals.

9.1 Future Work

Although we chose to study TNF-, IL-6, IL-8, and IL-10, there are many other important inflamma-tory mediators and factors involved in the inflammatory process. For example, as discussed in Chapter 2, IL-1β is considered one of the most important pro-inflammatory mediators released from monocytes upon endotoxin-induced activation and in addition to being a vasodilator, nitric oxide promotes inflammation and tissue injury [Chow et al., 2005; Tracey, 2002]. In fact, the ex-perimentalist did attempt to measure IL-1β. However, improper handling of the blood samples produced undetectable data. Additionally, the endotoxin-signaling pathway has been shown to involve lipopolysaccharide-binding protein (LBP), and the co-activators myeloid differentiation-2 (MD-2), and CD14, as well as TLR4. Each signaling pathway has a specific reaction time that may be dependent on the dose of endotoxin, the availability of co-activators as well as the specific mediator being activated. For instance, Blomkalns et al. [2011] found that the release of IL-8 by freshly isolated human peripheral blood mononuclear cells given a low dose of endotoxin was dependent on both membrane-associated CD14 and TLR4. In addition, it has been found that recognition by a specific receptor cluster is associated with the strain of bacteria [Hirschfeld et al., 2001]. To increase the accuracy of our model, we need to identify the specific pathways activated and the time necessary for production of the specific mediator, and then incorporate these factors into our model for future optimization.

In an effort to study the inflammatory response to higher doses, we attempted to raise to initial condition for P and analyze the model predictions. Unfortunately, we did not achieve a significant change in the dynamics, as seen in [Chow et al., 2005]. We would like to gather more insight into this area and make the necessary changes to the model to predict the expected response. In addition, we would like to develop a corresponding model appropriate for mice, with the necessary pathways, that we can use to further test our hypothesize that temperature and nitric oxide are the driving force behind the cardiovascular response to endotoxin.

Finally, findings suggest that in addition to affecting heart rate, an increase in temperature also affects blood pressure via vasoconstriction and vasodilation, which the body does in an effort to retain and expel heat. Additionally, the decreased pain perception may cause an increase in heart rate. Incorporating these interactions into the current coupled model may help explain the variations in responses between the normal and abnormal responders, as well as variations in the

HRV responses.

BIBLIOGRAPHY

Andreasen, A. S. et al. (2008). "Human endotoxemia as a model of systemic inflammation". *Curr Med Chem* **15**.17, pp. 1697–705.

Banks, H. T. et al. (2009). "An Inverse Problem Statistical Methodology Summary". *Mathematical and Statistical Estimation Approaches in Epidemiology*.

Banks, H. & Tran, H. (2009). *Mathematical and Experimental Modeling of Physical and Biological Processes*. Boca Raton, FL: CRC Press.

Batzel, J. et al. (2007). *Cardiovascular and Respiratory Systems*. Society for Industrial and Applied Mathematics.

Bearup, D. J. et al. (2013). "The input-output relationship approach to structural identifiability analysis". *Comput Methods Programs Biomed* **109**, pp. 171–181.

Benson, S. et al. (2012). "Acute experimental endotoxemia induces visceral hypersensitivity and altered pain evaluation in healthy humans". *Pain* **153**, pp. 794–9.

Bjorcl, A. (1996). *Numerical Methods for Least Squares Problems*. SIAM.

Blomkalns, A. L. et al. (2011). "Low level bacterial endotoxin activates two distinct signaling pathways in human peripheral blood mononuclear cells". *J Inflamm (Lond)* **8**.

Borovikova, L. V. et al. (2000). "Vagus nerve stimulation attenuates the systemic inflammatory response to endotoxin". *Nature* **405**, pp. 458–62.

Brinth, L. S. et al. (2015). "Orthostatic intolerance and postural tachycardia syndrome as suspected adverse effects of vaccination against human papilloma virus". *The Journal of Rheumatology* **33**.22, pp. 2602–5.

Buchwald, D. et al. (1997). "Markers of inflammation and immune activation in chronic fatigue and chronic fatigue syndrome". *The Journal of Rheumatology* **24**.2, pp. 372–376.

Cacuci, D. (2003). *Sensitivity & Uncertainty Analysis*. Chapman and Hall.

Chambers, J. M. (1983). *Graphical Methods for Data Analysis*. Belmont, California: Wadsworth International Group.

Chow, C. C. et al. (2005). "The acute inflammatory response in diverse shock states". *Shock* **24**, pp. 74–84.

Chowdhary, S. et al. (2000). "Nitric oxide and cardiac autonomic control in humans". *Hypertension* **36**, pp. 264–269.

Clermont, G. et al. (2004a). "In silico design of clinical trials: a method coming of age". *Crit Care Med* **32**, pp. 2061–70.

Clermont, G. et al. (2004b). "Mathematical and Statistical Modeling of Acute Inflammation". *Classification, Clustering, and Data Mining Applications*. Springer Berlin Heidelberg.

Conti, B. et al. (2004). "Cytokines and fever". *Front Biosci* **9**, pp. 1433–49.

Copeland, S. et al. (2005). "Acute inflammatory response to endotoxin in mice and humans". *Clin Diagn Lab Immunol* **12**, pp. 60–7.

Cowie, D. A. et al. (2004). "Orthostatic hypotension occurs frequently in the first hour after anesthesia". *Anesth Analg* **98**, pp. 40–5.

Day, J. et al. (2006). "A reduced mathematical model of the acute inflammatory response II. Capturing scenarios of repeated endotoxin administration". *J Theor Biol* **242**, pp. 237–56.

Deventer, S. J. van et al. (1990). "Experimental endotoxemia in humans: analysis of cytokine release and coagulation, fibrinolytic, and complement pathways". *Blood*.

Dick, J. et al. (2013). "High-dimensional integration: the quasi-Monte Carlo way". *Acta Numerica* **22**, pp. 133–288.

Edelstein-Keshet, L. (2005). *Mathematical Models in Biology*. Society for Industrial and Applied Mathematics.

Ellwein, L. M. (2008). "Cardiovascular and respiratory modeling". PhD thesis. Raleigh, NC: North Carolina State University.

Evans, S. S. et al. (2015). "Fever and the thermal regulation of immunity: the immune system feels the heat". *Nat Rev Immunol* **15**, pp. 3335–49.

Fried, E. et al. (2011). "Postoperative sepsis". *Curr Opin Crit Care* **17**, pp. 396–401.

Gellish, R. L. et al. (2007). "Longitudinal modeling of the relationship between age and maximal heart rate". *Med Sci Sports Exerc* **39**, pp. 822–9.

Gen, M. & Cheng, R. (2000). *Genetic Algorithms and Engineering Optimization.* A Wiley-Interscience publication. Wiley.

Griewank, A. (1989). "On automatic differentiation". *Mathematical Programming: recent developments and applications 6*, pp. 83–107.

Grubb, B. P. (2008). "Postural Tachycardia Syndrome". *Circulation* **117**.21, pp. 2814–2817.

Guerra, M. L. et al. (2015). "Early mobilization of patients who have had a hip or knee joint replacement reduces length of stay in hospital: a systematic review". *Clin Rehabil* **29**.9, pp. 844–54.

Guyton, A. C. & Hall, J. E. (2011). *Guyton and Hall textbook of medical physiology.* Philadelphia, PA: Saunders Elsevier.

Haario, H. et al. (2006). "DRAM: Efficient adaptive MCMC". *Statistics and Computing* **16**.4, pp. 339–354.

Hakim, T. S. et al. (1996). "Half-life of nitric oxide in aqueous solutions with and without haemoglobin". *Physiol Meas* **17**.4, pp. 267–77.

Hansen, M. K. et al. (2001). "The contribution of the vagus nerve in interleukin-1beta-induced fever is dependent on dose". *Am J Physiol Regul Integr Comp Physiol* **280**.4, R929–34.

Harada, A. et al. (1994). "Essential involvement of interleukin-8 (IL-8) in acute inflammation". *J Leukoc Biol* **56**.5, pp. 559–64.

Heiss, F. & Winschel, V. (2008). "Likelihood approximation by numerical integration on sparse grids". *Journal of Econometrics* **144**.1, pp. 62 –80.

Heldt, T. et al. (2002). "Computational modeling of cardiovascular response to orthostatic stress". *J Appl Physiol (1985)* **92**.3, pp. 1239–54.

Hirschfeld, M. et al. (2001). "Signaling by toll-like receptor 2 and 4 agonists results in differential gene expression in murine macrophages". *Infect Immun* **69**.3, pp. 1477–82.

Huston, J. M. & Tracey, K. J. (2011). "The Pulse of Inflammation: Heart Rate Variability, the Cholinergic Anti-Inflammatory Pathway, and Implications for Therapy". *J Intern Med* **269**.1, pp. 45–53.

Institute, T. H. (2016). *Heart Anatomy*. URL: `http://www.texasheart.org/HIC/Anatomy/anatomy2.cfm`.

Jan, B. U. et al. (2010). "Relationship of Basal Heart Rate Variability to in Vivo Cytokine Responses Following Endotoxin". *Shock* **33**.4, pp. 363–8.

Janeway, C. et al. (2001). *Immunobiology: The Immune System in Health and Disease*. Taylor & Francis, Inc.

Jans, O. et al. (2012). "Orthostatic intolerance during early mobilization after fast-track hip arthroplasty". *Br J Anaesth* **108**.3, pp. 436–43.

Janum, S. et al. (2016). "Pain perception in healthy volunteers: effect of repeated exposure to experimental systemic inflammation". *Innate Immun* **22**.7, pp. 546–556.

Kappel, F. & Peer, R. O. (1993). "A mathematical model for fundamental regulation processes in the cardiovascular system". *J Math Biol* **31**.6, pp. 611–31.

Kelley, C. (1999). *Iterative Methods for Optimization*. Philadelphia, PA: SIAM.

Kiparissides, A. et al. (2009). "Global Sensitivity Analysis Challenges in Biological Systems Modeling". *Industrial & Engineering Chemistry Research* **48**, pp. 7168–7180.

Kirkeboen, K. A. & Strand, O. A. (1999). "The role of nitric oxide in sepsis–an overview". *Acta Anaesthesiol Scand* **43**, pp. 275–88.

Kumar, R. et al. (2004). "The dynamics of acute inflammation". *J Theor Biol* **230**, pp. 145–55.

Madsen, K. et al. (2004). *Methods for Nonlinear Least Squares Problems*. Denmark.

Maradit Kremers, H. et al. (2015). "Prevalence of Total Hip and Knee Replacement in the United States". *J Bone Joint Surg Am* **97**, pp. 1386–97.

Marquardt, D. (1963). "An Algorithm for Least-Squares Estimation of Nonlinear Parameters". *SIAM* **11**, pp. 431–441.

Marsland, A. L. et al. (2007). "Stimulated production of proinflammatory cytokines covaries inversely with heart rate variability". *Psychosom Med* **69**, pp. 709–16.

Martich, G. D. et al. (1991). "Detection of interleukin 8 and tumor necrosis factor in normal humans after intravenous endotoxin: the effect of antiinflammatory agents". *J Exp Med* **173**, pp. 1021–4.

Mathews, J. H. & Fink, K. D. (1998). *Numerical Methods Using MATLAB*. Simon & Schuster.

Merck (2017). *Overview of the Autonomic Nervous System*. URL: `http://www.merckmanuals.com/home/brain`.

Miao, H. et al. (2011). "On identifiability of nonlinear ODE models and applications in Viral Dynamics". *SIAM Rev Soc Ind Appl Math* **53**, pp. 3–39.

Mukkamala, R. (2000). "A forward model-based analysis of cardiovascular system identification methods". PhD thesis. Cambridge, MA: Massachusetts Institute of Technology.

Mukkamala, R. & Cohen, R. J. (2001). "A forward model-based validation of cardiovascular system identification". *Am J Physiol Heart Circ Physiol* **281**, H2714–30.

Netea, M. et al. (2000). "Circulating cytokines as mediators of fever". *Clinical Infectious Diseases* **31**.Supplement 5, S178–S184.

Nieman, G. et al. (2012). "A two-compartment mathematical model of endotoxin-induced inflammatory and physiologic alterations in swine". *Crit Care Med* **40**, pp. 1052–63.

Olufsen, M. S. & Ottesen, J. T. (2013). "A practical approach to parameter estimation applied to model predicting heart rate regulation". *J Math Biol* **67**, pp. 39–68.

Olufsen, M. S. et al. (2005). "Blood pressure and blood flow variation during postural change from sitting to standing: model development and validation". *J Appl Physiol* **99**, pp. 1523–37.

Orfanidis, S. J. (1995). *Introduction to Signal Processing*. Upper Saddle River, NJ, USA: Prentice-Hall, Inc.

Pajkrt, D et al. (1997a). "Attenuation of proinflammatory response by recombinant human IL-10 in human endotoxemia: effect of timing of recombinant human IL-10 administration." *The Journal of Immunology* **158**.8, pp. 3971–3977.

Pajkrt, D. et al. (1997b). "Modulation of cytokine release and neutrophil function by granulocyte colony-stimulating factor during endotoxemia in humans". *Blood* **90**, pp. 1415–24.

Pearse, E. O. et al. (2007). "Early mobilisation after conventional knee replacement may reduce the risk of postoperative venous thromboembolism". *Bone & Joint Journal* **89-B**.3, pp. 316–322.

Persson, P.-O. & Strang, G. (2003). "Smoothing by Savitzky-Golay and Legendre Filters". *Mathematical Systems Theory in Biology, Communications, Computation, and Finance*. Ed. by Rosenthal, J. & Gilliam, D. S. New York, NY: Springer New York, pp. 301–315.

Poll, T. van der et al. (1997). "Antiinflammatory cytokine responses during clinical sepsis and experimental endotoxemia: sequential measurements of plasma soluble interleukin (IL)-1 receptor type II, IL-10, and IL-13". *J Infect Dis* **175**, pp. 118–22.

Pope, S. R. et al. (2009). "Estimation and identification of parameters in a lumped cerebrovascular model". *Math Biosci Eng* **6**, pp. 93–115.

Resource, W. C. (2015). *Anatomy of Skin & Physiology of Healing*. URL: http://woundcareresource.com/basic.html.

Reynolds, A. et al. (2006). "A reduced mathematical model of the acute inflammatory response: I. Derivation of model and analysis of anti-inflammation". *J Theor Biol* **242**, pp. 220–36.

Rossol, M. et al. (2011). "LPS-induced cytokine production in human monocytes and macrophages". *Crit Rev Immunol* **31**, pp. 379–446.

Schobel, H. P. et al. (1996). "Hemodynamic and sympathetic nerve responses to painful stimuli in normotensive and borderline hypertensive subjects". *Pain* **66**, pp. 117–24.

Schulte, W. et al. (2013). "Cytokines in Sepsis: Potent Immunoregulators and Potential Therapeutic Targets: An Updated View". *Mediators of Inflammation* **2013**, p. 16.

Seber, G. A. F. & Wild, C. J. (2003). *Nonlinear Regression*. Hoboken, NJ: John Wiley & Sons, Inc.

Seok, J. et al. (2013). "Genomic responses in mouse models poorly mimic human inflammatory diseases". *Proc Natl Acad Sci U S A* **110**, pp. 3507–12.

Smith, J. & Kampine, J. (1990). *Circulatory physiology - the essentials*. The Williams & Wilkins Company.

Smith, R. (2014). *Uncertainty Quantification: Theory, Implementation, and Applications*. SIAM.

— (2016). "Uncertainty Quantification for Biological Models".

Starkie, R. et al. (2003). "Exercise and IL-6 infusion inhibit endotoxin-induced TNF-alpha production in humans". *FASEB J* **17**, pp. 884–6.

Sun, L. & Ye, R. D. (2012). "Role of G protein-coupled receptors in inflammation". *Acta Pharmacol Sin* **33**, pp. 342–50.

Torio, C. & Moore, B. (2013). *National Inpatient Hospital Costs: The Most Expensive Conditions by Payer, 2013: Statistical Brief #204*. URL: https://www.ncbi.nlm.nih.gov/books/NBK368492/.

Tracey, K. J. (2002). "The inflammatory reflex". *Nature* **420**, pp. 853–9.

— (2007). "Physiology and immunology of the cholinergic antiinflammatory pathway". *J Clin Invest* **117**, pp. 289–96.

Ursino, M. (1998). "Interaction between carotid baroregulation and the pulsating heart: a mathematical model". *Am J Physiol*.

Valdez-Jasso, D. et al. (2008). "Viscoelastic mapping of the arterial ovine system using a Kelvin model". *IEE Trans Biomed Eng*.

Vincent, J. L. et al. (2000). "Effects of nitric oxide in septic shock". *Am J Respir Crit Care Med*.

Wegner, A. et al. (2014). "Inflammation-induced hyperalgesia: effects of timing, dosage, and negative affect on somatic pain sensitivity in human experimental endotoxemia". *Brain Behav Immun*.

Williams, N. et al. (2013). "Patient-specific modeling of head-up tilt". *Math Med Biol*.

Zhang, J. M. & An, J. (2007). "Cytokines, Inflammation and Pain". *Int Anesthesiol Clin*.

APPENDIX

A

MATLAB SOURCE CODES

As mentioned in Chapter 4, the sensitivity analysis, identifiability analysis, and optimization methods were implemented using `MATLAB`. This Appendix introduces the code used to obtain the results in Chapters 4, 6 , and 8. The full code can be found on the Cardiovascular Dynamics Group website. The optimization and uncertainty quantification code has been adapted from code developed by Dr. C. Tim Kelley [1999] and the Research Training Group tutorial by Dr. Ralph C. Smith [2014], respectively. Bayesian uncertainty quantification is done using the MCMC `MATLAB` toolbox developed by Dr. Heikki Haario [2006].

---

mSIRS Model

Solves the differential equations ((4.2) of Chapter 4) predicting states within the mSIRS model. This code returns plots of model predictions for S, I, and R.

Executable `DriverBasic.m`

Calls   `load_global.m`   sets parameters and initial conditions.
       `modelBasic.m`   right hand side of ODEs.

Output   Model states S, I, and R as a function of time.

Sensitivity Analysis

Computes the sensitivity matrix χ defined in (4.8) of Chapter 4. From this, ranked sensitivities are computed as described in Section 4.3. Returns plot of ranked and time-varying sensitivities, as well as the sensitivity ranking.

Executable `DriverBasic_sens.m`

Calls	`load_global.m`	sets parameters and initial conditions.
	`senseq.m`	Solves ODEs by calling `modelBasic.m`; computes sensitivities using forward/central difference.

Output `sens.mat` (MAT-file containing sensitivity matrix χ and ranked sensitivities).

Identifiability Analysis

Identifies pairwise parameter correlations using the structured correlation method (explained in Section 4.4.2 of Chapter 4).

Executable `covariance.m`

Input `sens.mat`, ζ (identifiability cutoff).

Output `INDMAP` (indices of uncorrelated parameters after running iteratively).

Optimization

Optimizes the parameters of `INDMAP` using either the Nelder-Mead or Levenberg-Marquardt algorithms.

Nelder-Mead

The Nelder-Mead simplex algorithm, described in Section 4.5.1, is implemented using the built-in MATLAB function `fminsearch.m`.

Executable `DriverBasic_NM.m`

Input data, `INDMAP`

155

Calls	load_global.m	sets parameters and initial conditions.
	fminsearch.m	optimizes parameters of INDMAP using the Nelder-Mead algorithm; built-in MATLAB optimizer.
	→ Calls model_fmin.m	returns the model solution, residual $R = y_{\text{model}} - y_{\text{data}}$, and cost $J(\theta) = R^T R$.
	⟶ Calls model_wrap.m	wraps parameters of INDMAP into ALLPARS (all remaining parameters).
	⟶⟶ Calls model_sol.m	returns the model solution by calling modelBasic.m.

Output parsopt (optimal parameters of INDMAP).

Levenberg-Marquardt

The Levenberg-Marquardt algorithm, which uses a combination of the gradient-descent and Gauss-Newton methods, as described in Section 4.5.2 of Chapter 4, can be implemented using the optimization code developed by Dr. Tim Kelley [Kelley, 1999] or via the built-in MATLAB function nlinfit.m.

Executable DriverBasic_LM_TK.m

Input data, INDMAP

Calls	load_global.m	sets parameters, initial conditions, and upper and lower bounds for optimizer.
	newlsq_v2.m	optimizes parameters of INDMAP using the Levenberg-Marquardt algorithm; adapted from Dr. Tim Kelley's optimization code.
	→ Calls opt_wrap.m	returns the residual $R = y_{\text{model}} - y_{\text{data}}$, the cost $J(\theta) = R^T R$, and the sensitivity matrix χ.
	⟶ Calls model_res.m	returns the model solution, R, and $J(\theta)$.
	⟶⟶ Calls model_wrap.m	wraps parameters of INDMAP into ALLPARS (all remaining parameters) and returns the model solution.
	⟶⟶⟶ Calls model_sol.m	returns the model solution by calling modelBasic.m.

Output   `parsopt` (optimal parameters of `INDMAP`).

An advantage of the optimization code developed by Dr. C. Tim Kelley is that upper and lower bounds are placed on the parameter values to ensure that they converge to feasible values. The Levenberg-Marquardt algorithm in `MATLAB` does not have this option.

Executable `DriverBasic_LM_nlinfit.m`

Input   data, `INDMAP`

Calls   `load_global.m`   sets parameters and initial conditions.
              `nlinfit.m`   optimizes parameters using `MATLAB`'s built-in
                                            Levenberg-Marquardt algorithm.
              → Calls `model_wrap_nl.m`   wraps parameters of `INDMAP` into `ALLPARS` (all
                                            remaining parameters) and returns the model
                                            solution.
              ⟶ Calls `model_sol.m`   returns the model solution by calling
                                            `modelBasic.m`.

Output   `parsopt` (optimal parameters of `INDMAP`), the residual $R = y_{model} - y_{data}$, cost
              $J(\theta) = R^T R$, and mean squared error $s^2 = J(\theta)/(N-p)$, where N is the number of data
              points and p is the number of parameters being optimized, and covariance matrix
              defined by $(\chi^T \chi)^{-1} s^2$.

Uncertainty Quantification

Computes the confidence, prediction, and credible intervals for the mSIRS model. Also computes the parameter confidence intervals. Parameter confidence intervals and confidence intervals are computed using frequentist methods [Smith, 2014]. Credible intervals are computed using Bayesian methods [Haario et al., 2006]. Prediction intervals are computed using either frequentist or Bayesian methods.

Frequentist Intervals

Frequentist intervals code is adapted from the Research Training Group tutorial by Dr. Ralph C. Smith [2014].

Executable `DriverBasic_intervals.m`

Input	data, `parsopt`, `INDMAP`, χ, s^2	
Calls	`modelBasic.m`	right hand side of ODEs.
	`nlparci.m`	built-in MATLAB function used to compute parameter confidence intervals.
	→ Calls `model_wrap_nl.m`	wraps parameters of `INDMAP` into `ALLPARS` (all remaining parameters) and returns the model solution.
	⟶ Calls `model_sol.m`	returns the model solution by calling `modelBasic.m`.
Output	Parameter confidence intervals, plots of model solution with frequentist prediction and confidence intervals.	

Bayesian Intervals

Bayesian methods are adapted from the MCMC MATLAB toolbox by Dr. Hiekki Haario 2006.

Executable `DriverBasic_DRAM.m`

Input data, `parsopt`, `INDMAP`, s^2

Calls	`mcmcrun.m`	returns parameter chains used to obtain posterior distributions using MCMC algorithm.
	→ Calls `model_res.m`	returns the model solution, the residual $R = y_{\mathrm{model}} - y_{\mathrm{data}}$, and the cost $J(\theta) = R^T R$.
	⟶ Calls `model_wrap.m`	wraps parameters of `INDMAP` into `ALLPARS` (all remaining parameters) and returns the model solution.
	⟶ Calls `model_sol.m`	returns the model solution by calling `modelBasic.m`.
	`mcmcplot.m`	plots parameter chains, probability densities, and parameter pairs.
	`mcmcpred.m`	computes credible and prediction intervals using Bayesian MCMC algorithm.
Output	Plots of model solution, credible and prediction intervals.	